Summer 2017

Study of multi-axial failure properties of planar biological soft tissues

Timothy Kwang-Joon Chung
University of Iowa

STUDY OF MULTI-AXIAL FAILURE PROPERTIES OF PLANAR BIOLOGICAL SOFT TISSUES

by

Timothy Kwang-Joon Chung

A thesis submitted in partial fulfillment
of the requirements for the Doctor of Philosophy
degree in Biomedical Engineering in the
Graduate College of
The University of Iowa

August 2017

Thesis Supervisor: Professor Suresh M.L. Raghavan

Graduate College
The University of Iowa
Iowa City, Iowa

CERTIFICATE OF APPROVAL

PH.D. THESIS

This is to certify that the Ph.D. thesis of

Timothy Kwang-Joon Chung

has been approved by the Examining Committee for
the thesis requirement for the Doctor of Philosophy degree
in Biomedical Engineering at the August 2017 graduation.

Thesis Committee: _____
M.L. Suresh Raghavan, Thesis Supervisor

_____
Joseph M. Reinhardt

_____
Nicole M. Grosland

_____
Edward Sander

_____
Shaoping Xiao

Thank you, to Good old days

He has told you, O man, what is good;
And what the LORD require of you
But to do justice, to love kindness,
and to walk humbly with your God?

-Micah 6:8

ACKNOWLEDGEMENTS

If I were to revisit my past in this present moment, I may not have believed in what the future had in store for me. Some people call it serendipity (probabilistic framework), but I call it Divine provision (deterministic). I do not know what I deserved to have a family like mine, or where I would be without them. I want to thank my parents for their great patience with a very rebellious and low-motivated son (recovery complete). They are still the smartest people I know, and that will remain so from their wisdom they've gained throughout the years. Thank you, mom and dad. I want to also thank my brother Jonny for being there for supporting me throughout the years spiritually and physically (thanks for throwing the refrigerator at me). My grandpa has been the family patriarch throughout the years and a source of admiration. He has been an example of someone who is steadfast in his faith and what it means to be Christ-like.

I also want to take time to thank my aunt and uncle, June and Charles Yang for being pioneers in a new land. They learned the culture, worked hard and supported our immediate family throughout the years, we wouldn't have made it without you. I also want to thank my second aunt and uncle and my cousins Stacy, Lynn and Jennifer Baek. You've been good throughout the years to me and many blessings to all your families (sorry, you guys have too many kids to acknowledge here, just know that uncle Timmy cares…). One thing you trained me to do was to put down the toilet seat after use…'CHUNG! Put down that seat!!'. I know my now wife (Eunice) appreciates it.

I want to thank Pastor Lee for teaching me scripture in my formative years and when I was still blind. I want to thank Pastor Tony for discipleship for when I could see, but was yet struggling in many different facets of my life.

I would like to take time to thank my academic advisor M.L. Suresh Raghavan. It has been a slippery slope at times and it has been smooth sailing at other times. I appreciate the immense grace you showed me when I was needing a research home during graduate school. Maybe you should gamble more often. At the bottom of my heart, I have always been thankful for being given an opportunity to research under you. Thank you for the much-needed criticism and guidance throughout my graduate school days (I may have become delusional without it). Hopefully you don't read this. I also want to thank the BioMOST lab. Being surrounded by cleverer people than me has been a humbling experience. I always appreciate learning, listening and discussing various topics with my lab mates. I would like to thank Dr. Chaid Schwarz, Dr. Ben Berkowitz and Dr. Anna Schumacher for their friendship and conversations. I want to thank my undergraduate helper (and friend), Brett Austin for aiding me with various experiments and for having a willingness to do more than required of him (you will be an excellent physician in the near future). I also want to thank Srivats Sarathy (future Ph.D.) for the random deep conversations late at night in the lab. I seriously appreciate the help with the uniaxial extension experiments and for getting the bacterial cellulose samples. I wanted to troll you a bit in my acknowledgements, but decided the general public probably wouldn't understand.

I want to also mention my in laws (Jung and Kyeong Kim) for being supportive and understanding when I didn't have a job or know when I was going to graduate…takes a lot of faith, thank you. I should mention my bro in law, Minwoo, thanks for being cool with me from the get go. The nagging is so that you will be better than I was during the same timepoint in life…

Last but not least, I would like to thank my wife, Eunice Chung (yes, you've been Chungified) for her constant support throughout the ups and downs of graduate school life. Leading up to my dissertation defense and marriage, you did all you could do to plan for our wedding and make sure everything was in order. I appreciate the time and energy you invested to make my life a little more stress-free during this time. We've been through quite a bit and thank you for choosing me to spend the rest of your life with. You are an amazing person that challenges me to be a better person and shows me where to be humble (cough cough). I hardly doubt that there will be a dull moment with our life together, and may our love continue to grow deeper with each other and our future children.

Oh, I almost forgot. I want to thank those furry raccoons that literally run across the street into the sewer when I'm driving home late at night scaring me half to death. I want to also thank the family of swallows who decided to build a nest right above the front door of the house. It gives the game 'dodgeball' a whole new meaning, please don't use my head as target practice.

There are too many people to thank in my life. If I were to mention all of them, I would have written more here than in my dissertation.

ABSTRACT

Rupture of abdominal aortic aneurysm (AAA) is a catastrophic event that leads to high mortality and morbidity in patients. The primary causes associated with aneurysm rupture remain poorly understood despite rigorous investigations. Reports have shown that AAA that went on to rupture or present ruptured had higher peak wall tension (stress resultant) than those that did not go on to rupture or present ruptured. Studies investigating the material strength of ruptured AAA and unruptured AAA revealed that the uniaxial failure strength in ruptured AAA is no different on average than unruptured AAA. However, it is poorly understood whether uniaxial failure properties are reliable as they are not indicative of the manner in which failure occurs in biological soft tissues.

Multi-axial failure properties using a bubble inflation test (BIT) have been implemented by various groups but have not been directly compared against uniaxial failure properties. The current study seeks to develop a BIT apparatus, to compare multi-axial and uniaxial failure properties of fibrous anisotropic biological soft tissues (bovine aorta) and non-fibrous isotropic molded silicon, and to perform a survey of computational indices at the rupture sites of four ruptured AAA. Two versions of the BIT apparatus were developed: a manual that was developed allows for a large amount of failure properties to be extracted that can identify localized weaknesses. It was found that circumferentially oriented multi-axial failure was correlated with longitudinally oriented uniaxial failure properties, however, for oblique oriented multi-axial failure the correlation decreased. Utilizing the insights gained from the multi-axial experiments it was determined that the failure properties used in the computational study with the data from

Raghavan et al. were appropriate for use in retrospective assessment of the rupture site in four ruptured AAA computational models.

Although the study was inconclusive in finding causation, the rupture line of each aneurysm had indices ranging between the third quartile and peak values for tension to failure tension ratio, nodal displacement magnitude, strain energy per unit volume and strain energy per unit surface area. This study provides a framework for interrogating failure properties at a higher density of measurement and a heterogeneous computational model that has the potential to predict AAA rupture in the future.

PUBLIC ABSTRACT

The cardiovascular system is a vast network of interconnected tubes, there is a tube located behind the stomach known as the abdominal aorta that is a major conduit of oxygenated blood flow to the lower region of the human body. A disease known as aneurysm arises in this region and the abdominal aorta undergoes irreversible ballooning and if left untreated can go on to rupture. Abdominal aortic aneurysm (AAA) rupture is a leading cause of death in westernized cultures and it remains poorly understood on why this occurs. Studies have considered the material strength of aneurysms and the amount of wall stress that the aneurysm wall is subject to in computer simulations with little consensus on what exactly is the root cause of rupture. This current study that is proposed investigates the material properties in all directions (multiaxial) using a bubble inflation test (the previous method to test failure in a single direction, uniaxial) and compare the two using biological soft tissues and manmade molded silicone. It was found that the multiaxial failure properties were correlated to the uniaxial failure properties and this information was utilized in a separate computer simulation of four ruptured AAA. There were no metrics that could predict the rupture site location, but in general stress and strain metrics used showed that the rupture site had elevated values between the 75th and 99th percentile. Further studies using the methods developed in this study may allow researchers to accurate predict rupture site location and provide clinicians with rupture risk assessments using computer simulations.

TABLE OF CONTENTS

TABLE OF TABLES

TABLE OF EQUATIONS

TABLE OF DERIVATIONS

TABLE OF FIGURES

CHAPTER 1 - BACKGROUND AND SIGNIFICANCE

1.1 - ABDOMINAL AORTIC ANEURYSM RUPTURE

The cardiovascular system is composed of a vast network of arteries that carry oxygenated blood to the rest of the body. The aorta is a major conduit of oxygenated blood to the head vessels along with the lower trunk. Specifically, the abdominal aorta is superior to the iliac arteries (that lead into the left and right legs) and is inferior to the renal arteries (that lead into the left and right kidneys). A healthy adult will have an average aortic diameter of 2 to 2.5 centimeters (cm).

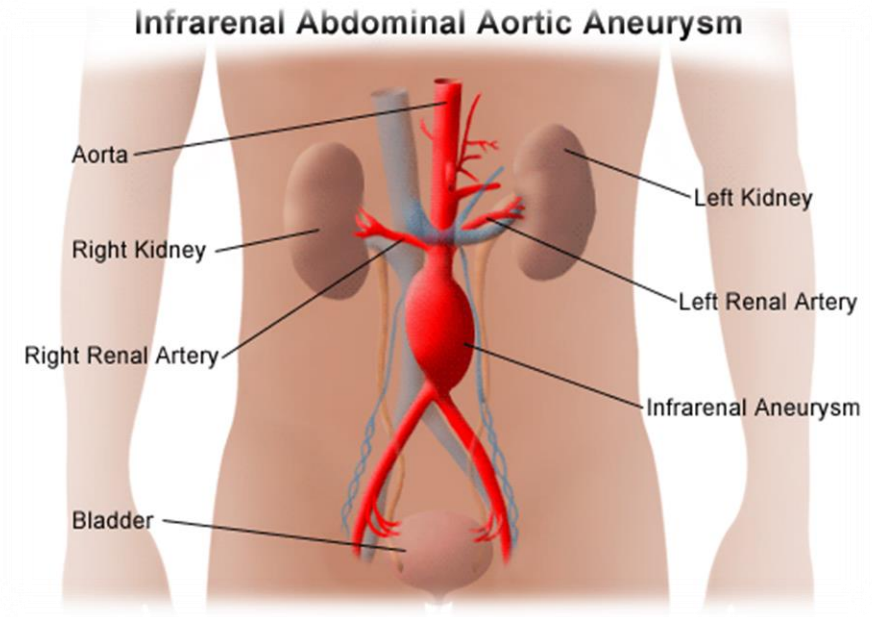

Figure 1: Abdominal aortic aneurysm physiologic location (inferior to renal arteries).

For unknown reasons, the abdominal aorta undergoes internal injury that leads to subsequent remodeling of the artery wall. Continued dilation occurs in the aorta under physiologic pressure and elevated pressure due to hypertension

over millions of cardiac cycles throughout the life of a patient. Diseased aneurysms can reach up to diameters of 7 cm and usually exhibit asymmetric growth that cannot be easily predicted, and if left untreated may lead to rupture. AAA rupture is a catastrophic biomechanical event that occurs in small (less than 5 cm in diameter) and large sized aneurysms (greater than 5 cm in diameter) that penetrates through the aneurysm wall (Figure 2). Aneurysms are most prevalent in western societies among the elderly population. It still remains the 13th leading cause of cardiovascular related deaths in the United States. Although there are other complications that arise with having a dilated abdominal aorta, the major risk and concern is aneurysm rupture. Upon rupture, the artery wall is breached with blood and causes severe internal bleeding and subsequent pressurization of the abdominal cavity. Ruptured aneurysms will most likely result in death if there is no immediate intervention as the mortality rates are high due to complications from internal bleeding[1].

Figure 2: AAA rupture through the thickness

Clinicians face difficulties in discovering AAA due to the lack of screening for AAA and understanding when to operate on a patient with an aneurysm. Often, an AAA is discovered while screening for another disease by way of CT

scan or ultrasound screening. Cardiovascular surgeons repair AAA surgically when aneurysms have a maximum transverse diameter of 5.5 cm.

In 1977 Darling et al. performed a large AAA study to investigate whether size was a major factor in aneurysm rupture[2]. It was reported that 12.8% of aneurysms with a diameter less than or equal to 5 cm ruptured (34 ruptured out of a 265 total aneurysms), while 40% of aneurysms with a diameter greater than 5 cm ruptured (78 ruptured aneurysms out of 194 total aneurysms) and a rupture occurrence of 24.9% of all aneurysms ruptured (Table 1). This has been a preface for much speculation in the course of AAA rupture research as it cannot be simply stated that larger diameter aneurysms will rupture while smaller diameter aneurysms will not rupture.

Table 1: Summary of Darling et al AAA autopsy study.

Size (cm)	Ruptured	Unruptured	Total	%Ruptured
≤ 5.0	34	231	265	12.8
> 5.0	78	116	194	40.0
No Size	6	8	14	43.0
Total	118	355	473	24.9

Due to the high morbidity associated with AAA rupture, there has been much interest in the medical and biomedical engineering communities in understanding the mechanics of rupture. Studies investigating material properties (failure stress, tension and strain) of the diseased aneurysm wall, material components of the artery wall, and computational methods have aided in the process of understanding the mechanics of AAA rupture.

1.2 - ARTERY WALL COMPOSITION AND FIBER ORGANIZATION

The entire cardiovascular system is a living conduit that can undergo repair and remodeling from the constituents that make up the arterial wall. Albeit, the layers of the arterial wall are a manmade construct, it is important to understand how these layers relate to their mechanical strength. Figure 3 shows the various layers of the artery wall: The intima (innermost layer) is lined with endothelial cells surrounded by elastic, the tunica media contain smooth muscle cells, the tunica externa contains loose fibrous connective tissue and the serosa is the outermost layer that contains epithelial cells. It is important to note that the greatest heterogeneity in the artery wall occurs across the thickness of the wall itself.

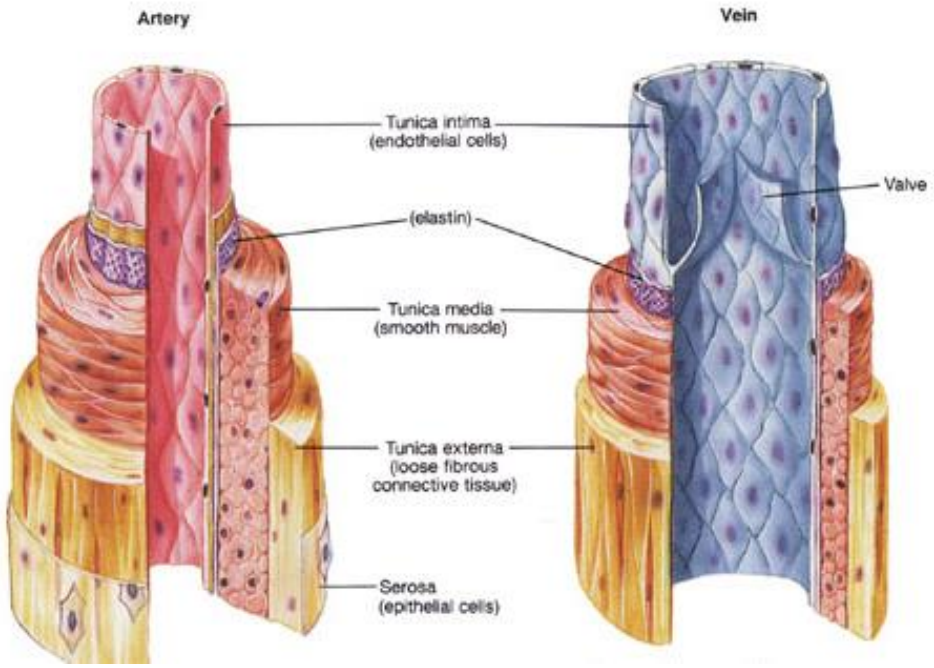

Figure 3: The layers of the arterial wall are shown beginning with the inner layer of endothelial cells (intima layer), smooth muscle (media), connective tissue (externa) and outermost layer known as the serosa.

He et al, 1994 investigated the composition of a AAA wall to understand whether the constituents that make up the wall had altered during the course of the diseased state[3]. It was reported that elastic and smooth muscle content decreased while collagen and ground substance content increased (i.e. the AAA wall increased in stiffness). The artery wall is composed of countless molecules that are organized into fibers that make up the wall tissue. The major fiber components that help retain the shape of the artery are elastin and collagen. The biochemical aspects of these fibers will not be discussed, but rather their mechanical contributions to the wall.

Elastin bands in the wall tissue are elastic components of the tissue. Elasticity is the ability for a deformed shape under a load to retain its original configuration when the load is withdrawn. As the wall tissue continues to deform, the elastin fibers become taut and collagen fibers are recruited. Collagen fibers withstand a much higher load than the elastin fibers, but they are unable to retain the original undeformed state.

The components of the wall are fused together but are given assigned layers as convention. The inner layer where blood flows is known as the intima layer, the media is the middle layer composed of smooth muscle cells, elastin and collagen, and the adventitia is the outermost layer that is composed of collagen and elastin (Figure 3). For all practical purposes, the mechanical contribution of these 'layers' have been relatively undefined in normal aortic tissue. However, Teng et al., 2015 reported mechanical properties on the various layers of diseased AAA tissue wall to reveal that all layers (adventitia,

media, thrombus) behaved nonlinearly in both the longitudinal and circumferential directions[4]. It was further noted that the failure properties were similar in both the longitudinal and circumferential when compared to each other.

The effect of heterogeneity was elucidated by Humphrey et al. when the concept of residual stresses of an artery (across the thickness) was first reported. Humphrey et al. found that the residual stresses across the artery wall thickness helped homogenize the circumferential stress[5]. Uniaxial extension tests have been performed on artery wall tissue that characterizes the indiscriminate contributions of the entire wall and the maximum load the artery wall can accept across longitudinally or circumferentially. These characterizations only describe the bulk stresses the entire wall can withstand and not what the wall can accept through its heterogeneous wall thickness (where actual rupture occurs). The nonlinearity of aneurysm wall tissue under load has been extensively reported on by Raghavan et al. and others[6–12] and many material models have been formulated from experimental data.

Figure 4 represents a sample uniaxial extension test, where the 'toe region' represents the wavy elastin fibers becoming taut, while the higher stress/strain region represent the recruitment of collagen fibers. Equation 1a – 1b refers to how stress is calculated incorporating the changes in the mid cross-sectional area as the tissue continues to stretch with the assumption of the material being isotropic with no volumetric changes as the material is being stretched.

The peak stress of the artery sample represents the stress across the entire thickness of the wall. Equation 1a encompasses the maximum stress with the actual cross-sectional area (stress along the thickness), and Equation 1b refers to the maximum tension with the thickness lumped together[8]. Failure stress normalizes the thickness contributions and reports the cross-sectional area change with an assumption of material isotropy.

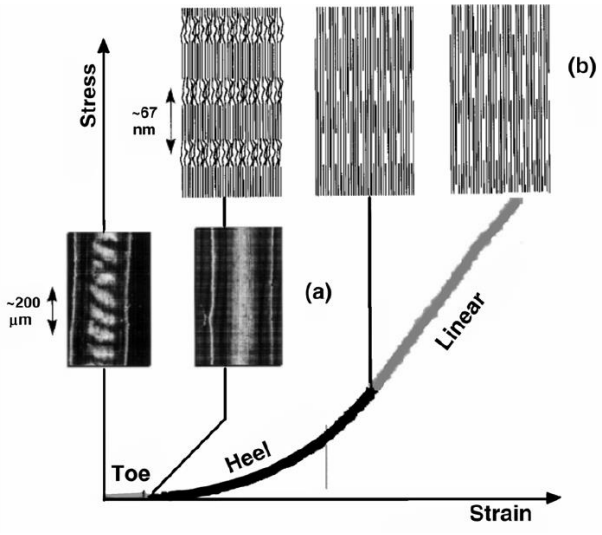

Figure 4: Elastin recruitment (toe region), combined stretching in the heel region, and the linear region of mostly collagen fibers (stiffness).

Equation 1(a) Stress in uniaxial extension (b) Tension in uniaxial extension tests.

$$Equation\ 1a:\ \ S_f = \frac{F_f}{w_o t_o}\left(1 + \varepsilon_f\right)$$

$$Equation\ 1b: T_f = \frac{F_f}{w_o}\left(\sqrt{1 + \ \varepsilon_f}\right)$$

$$S_f = Failure\ Stress;\ T_f = Failure\ Tension;\ \epsilon_f = Failure\ Strain;$$

$$w_o = Original\ width; t_o = \ Original\ Thickness$$

Failure tension eliminates the uncontrollable characteristics of thickness and describes the propensity of the wall to fail along its entire thickness. The contribution of thickness is ignored when using tension and may help clarify the

'maximum' load the arterial wall may withstand. Therefore, tension will be considered as the index of interest for comparisons of ruptured and unruptured aneurysms with stress being presented as a formality to what has been traditionally reported in literature.

1.3 - TESTING METHODS FOR BIOLOGICAL SOFT TISSUES

Studies have developed material models that are representative of how materials behave when subject to various external loading scenarios. Uniaxial, biaxial, planar radial extension tests (PRET) and bubble inflation tests (BIT) have been utilized to understand how materials behave during extension[4,7,12–19]. Uniaxial extensions tests allow for specimens to fail and provide information on the maximum allowable stress in a single direction (Figure 5). Limitations of the uniaxial extension test include: uniaxial extension tests are loaded in a single direction irrespective of fiber orientation, uniaxial extension tests are not representative of how vascular tissues interact with external loads found in the body, specimen size is limited to the biological tissue sample during experimentation, and the cutting involved in procuring samples.

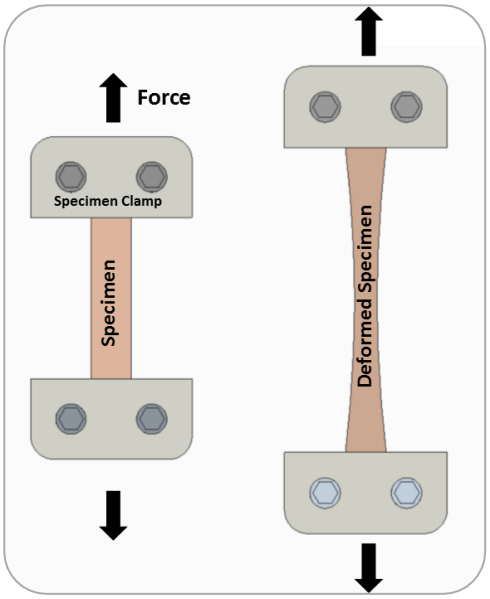

Figure 5: Uniaxial Extension test, example of a specimen under uniaxial extension

A large number of specimens diminish the reproducibility through premature specimen failure at the clamps. It is unknown if uniaxial failure

properties are representative of multiaxial failure properties that are subject during AAA rupture. In the past, uniaxial extension tests have been conducted in longitudinal and circumferentially oriented specimens[4,6,8,10,20–22], Reeps et al 2013 preferred circumferentially oriented AAA specimens for uniaxial testing as they exhibited higher failure properties than longitudinal strips[22]. Raghavan et al 2011 reported that circumferential failure properties were similar to those of the longitudinally oriented AAA specimens[6].

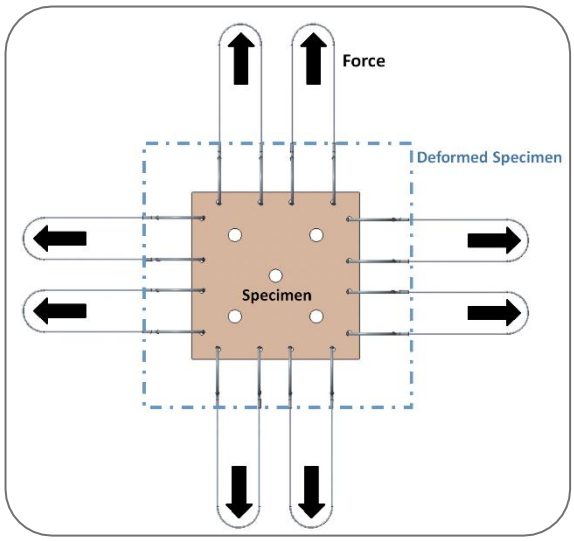

Figure 6: Biaxial extension test. Dotted line signifies deformed during equi-biaxial loading and white circles are markers for strain measurement.

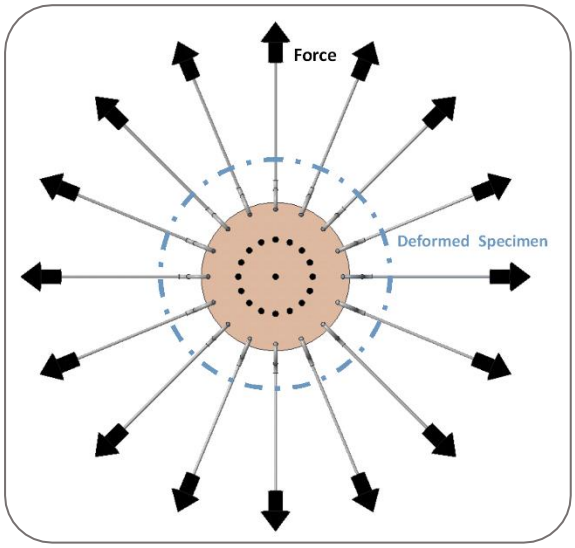

Figure 7: PRET- Dotted line signifies deformed shape during equi-radial loading and dotted circles are markers for strain measurement.

Biaxial extension tests allow for the specimen to undergo loading in two independent orientations to understand how biological soft tissues behave anisotropically (Figure 6). The limitations of this extension test are that the material is not allowed to fail, *a priori* knowledge of fiber orientation is needed to prevent the specimen from shearing, and hooking the specimen can create practical challenges. Researchers in the past have assumed fiber orientation for

biaxial extension tests[23,24]. Attempts have been made to determine fiber orientation using light scattering techniques for thin biological tissues[25,26] or determining the fiber orientation by loading the specimen in different orientations[27]. The inability to retrieve failure properties in biological soft tissues prevent the general understanding of how failure is affected by their biaxial elastic properties or whether a relationship between their respective biaxial properties and biaxial failure exist.

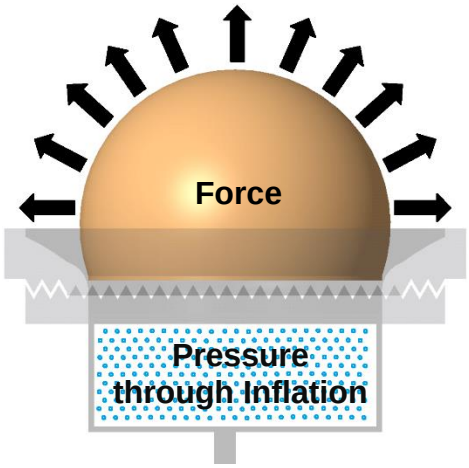

Figure 8: Bubble Inflation test. Multi-axial extension through inflation.

The planar radial extension test (PRET) loads a circular specimen radially in sixteen different directions[13] (Figure 7). PRET reveals the fiber orientation by placing force sensors radially and recording the force data during an equal displacement extension test. The PRET has limitations that include: elastic properties are available and not failure properties due to the nature of clamping,

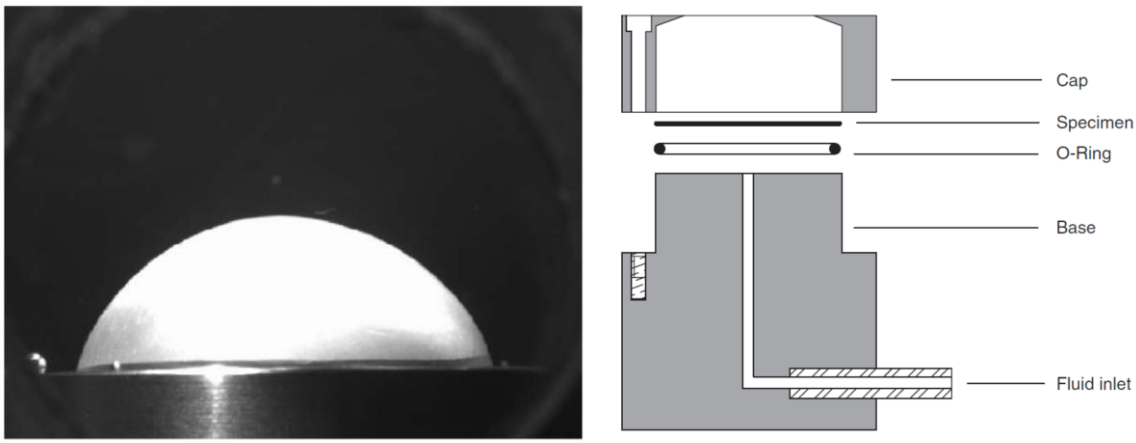

Figure 9: Slifka et al, bubble inflation tester with latex, bovine vascular material and PTFE.

loading specimens with hooks is challenging and starting at a zero load for all sixteen load cells with zero strain is cumbersome.

The bubble inflation test (BIT) involves rupturing a specimen multi-axially through inflation (Figure 8). Other groups have named this experiment type biaxial failure testing or biaxial tension testing. For clarity and consistency, the bubble inflation test will be referred to as a multi-axial failure test. The BIT has been used for non-biological tissues including polymers[28], latex[29], rubbers[30] and dough[31] to understand material properties. In the case of rubbers, researchers wanted to understand how large deformation materials interacted with external pressure loads. Additional synthetic materials were investigated using the inflation test because the materials tested were to be used under inflation in practice. Subsequent bubble inflation tests were implemented using biological tissues that included liver[32], bovine tissue[29], abdominal aortic aneurysm tissue[14] and thoracic aortic tissue[14,32–35]. Mohan et al developed a bubble inflation test that was named 'biaxial tension tester' and performed experiments with cadaveric thoracic aorta specimens[35]. The study attempted to bridge the gap in understanding between multiaxial failure and uniaxial failure properties, but due to constraints in the experimental apparatus not enough samples were tested to make this comparison. Other groups using the bubble inflation testing method have not made direct comparisons to uniaxial extension tests but have only speculated that uniaxial failure properties may not be correlated to multiaxial failure[32,33]. Drexler et al and Slifka et al performed bubble inflation tests with latex, bovine vascular material and polytetrafluorethylene (PTFE) and AAA

tissue[29,36] using capsule type BIT seen in Figure 9. Applications investigated how biological soft tissues and manmade vascular graft materials behaved during inflation. Milankovic et al developed a BIT apparatus for AAA specific research and reported displacement (height of bubble dome) and pressure during experimentation in a physiological thermal bath[14]. Pressure loading of biological soft tissues are advantageous in understanding how these fibrous, anisotropic materials behave in the cardiovascular system. Various research groups have investigated stress fields, material anisotropy, deformations and peak stresses of samples under pressure loading conditions. Davis et al implemented a two camera system that back calculated stress fields from strain fields during experimentation (Figure 10) [33,37]. However, simpler BIT systems have been implemented that only record peak stress and maximum deformation through optical measurements[14,29,34,35,38]. The BIT has

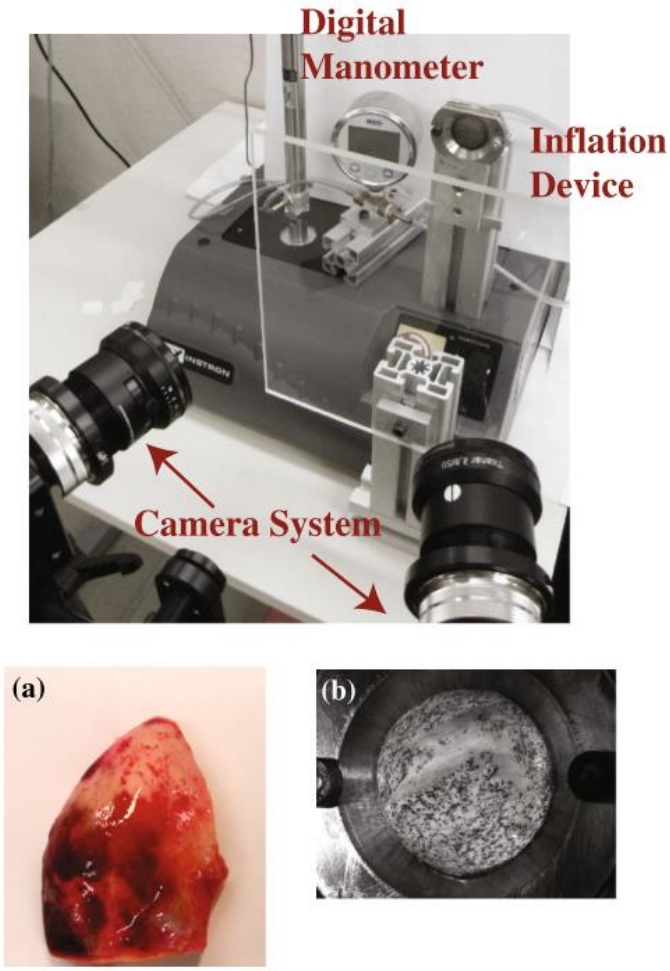

Figure 10: Two-camera apparatus with uniaxial plunger for strain/stress field calculations using BIT.

limitations in determining the maximum allowable specimen size (dependent on extracted biological sample), the implementation of a complex two-camera tracking system and the inverse calculation of the stress field. There is no consensus when it comes to the important indices that can be extracted from multiaxial bubble inflation tests. The aforementioned implementation of BIT has either looked at material heterogeneity (stress-strain fields) that requires a higher complexity or pressure-displacement data that in comparison is much easier to record. It is not yet clear on which information is most valuable to extract and whether multiaxial failure properties significantly differ from the current standard of using uniaxial failure properties.

Table 2: Survey of multiaxial testing methods and their obtainable data.

	Elastic Properties	Failure Properties	*a priori* fiber orientation	Easy to grip specimens?	Optical strain field measurements?
Uniaxial	Y	Y	N	Y	N
Biaxial	Y	N	Y	N	Y
PRET	Y	N	N	N	Y
BIT	Y	Y	N	Y	Y

Table 2 surveys the multi-axial extension tests strengths and weaknesses. The only experimental methods that can retrieve failure properties of soft tissues are with BIT and uniaxial extension testing. The comparison of oriented uniaxial failure properties (circumferential and longitudinal) with multiaxial failure properties remains to be of great interest and the implementation of this is found in Chapter 4. The proposed studies will exclusively look at failure properties of uniaxial extension tests and multiaxial extensions tests using the BIT.

1.4 – COMPUTATIONAL FINITE ELEMENT MODELING IN AAA

Finite element analysis has been a modeling tool to investigate the AAA rupture phenomenon. Computational studies coupled with material models from experimental uniaxial extension or biaxial extension testing have been used to understand the pressure induced wall stresses of aneurysms under ideal systolic pressure (120 mmHg) or patient specific blood pressure[9,23,39–49]. The majority of computational models that are reported in literature feature a constant wall thickness, homogeneous material properties (isotropic model) for the entire AAA model. Traditionally in literature, the peak wall stress (maximum principal stress) of a given aneurysm geometry has been reported as a metric to determine whether an aneurysm has a propensity to rupture.

Attempts have been made to incorporate thicknesses in models to determine stress more accurately, but the limitations to the current resolution of computed tomography imaging does not provide reliable thickness values[50]. Conclusions have been made that increased AAA thickness may be indicative of non-load bearing material whereas thinner areas may be indicative of weak spots that result in higher peak wall stress[50]. An example of non-load bearing material contribution is intraluminal thrombus (ILT) and this has been modeled as well in AAA computational studies[24,51–53]. Gasser et al[44] reported that there was a strong correlation between high stress and aneurysm rupture in a meta-analysis of retrospective computational studies. It has also been reported that

symptomatic AAA rupture have been correlated to pressure induced wall stress[40–42] but a causative relationship has not been found.

In attempts to find a causative relationship relating pressure induced stress, Vande Geest et al.[48,49] developed a stochastic equation to estimate failure strength in AAA and developed a metric known as the rupture potential index (pressure induced stress to failure strength ratio). It is thought that when the pressure induced stress exceeds the local failure strength, rupture occurs. However, if the stochastic equation estimating failure strength cannot accurately capture localized weaknesses, AAA rupture site cannot be predicted. Albeit, many computational studies have been performed, only correlation between peak wall stress and the propensity for an aneurysm to rupture have been made. Richer data sets that interrogate failure properties in various regions of an AAA along with wall thicknesses measurements are needed to fill in the gaps of the overall approach taken in computational studies. Understanding material heterogeneity and the effects of wall thickness would enhance the methods used to predict rupture site in AAA computational mechanics.

1.5 - POST-MORTEM ANEURYSM RESEARCH

Thubrikar et al. completed a study on the mechanical properties of aneurysms in different regions of the aneurysm[7]. The research group excised five whole aneurysms with diameters greater than 5 cm. It was found that the posterior regions were thicker than the anterior regions and that the wall stiffness increased from the posterior to anterior to lateral regions of the aneurysm. A total of 46 longitudinal and circumferential strips were tested with a total of 47

thickness measurements. The purpose of the study was not to test a hypothesis but rather report qualitatively and quantitatively the characteristics of diseased aneurysms.

Raghavan et al. completed a study that was similar in nature to Thubrikar's work with a greater density of measurement[6]. They retrieved measured data from post-mortem patients with diseased aneurysmal tissue. A total of thirteen aneurysms were excised that included four ruptured aneurysms and nine unruptured aneurysms (Figure 11). All aneurysms were examined and tested with the same protocol within 48 hours of autopsy[6]. Wall thicknesses were measured with a digital caliper in the anterior, posterior, right and left regions of the aneurysm with about 40 measurements per aneurysm. Uniaxial extension tests were performed on about 6 specimens per aneurysm with consistent

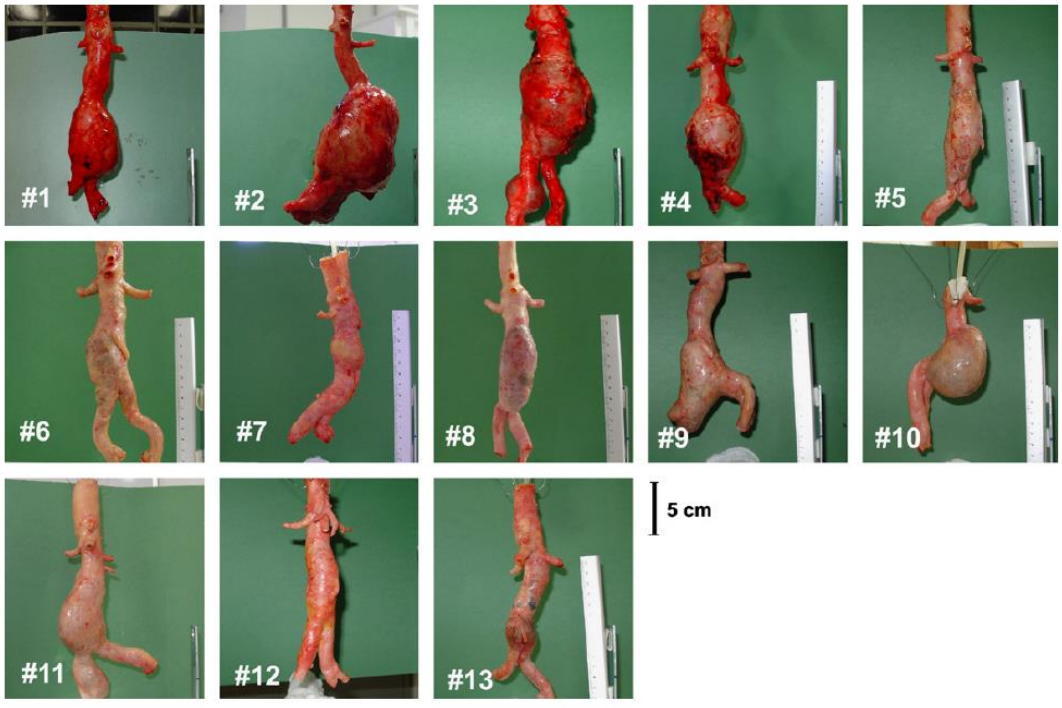

Figure 11: Four ruptured (aneurysms 1-4) and nine unruptured AAA (aneurysms 5-13) as reported in Raghavan et al 2011.

geometry (aside from thickness) per aneurysm and force displacement data was collected for analysis. Specimens were taken in the longitudinally oriented direction with a few specimens taken in the circumferentially oriented direction. Histology was performed on a strip adjacent to the uniaxial extension test specimens as well. In addition to the measured data collected, 36 digital photographs revolving around the aneurysm were taken in front of a green background for each aneurysm of interest.

Table 3: Aneurysm ID with age, aneurysm status, aneurysm diameter, number of material strips and thickness sites collected in Raghavan et al. 2011.

ID	Age	Rupture Status	Diameter (cm)	Strips	Thickness Sites
1	66	Ruptured	5.06	5	33
2	75	Ruptured	7.93	6	36
3	70	Ruptured	6.83	5	46
4	69	Ruptured	5.48	5	26
5	74	Unruptured	4.06	6	28
6	79	Unruptured	3.84	8	26
7	84	Unruptured	3.2	4	43
8	46	Unruptured	3.35	4	20
9	69	Unruptured	4.31	10	28
10	80	Unruptured	6.58	2	20
11	84	Unruptured	4.46	11	37
12	79	Unruptured	3.31	6	28
13	90	Unruptured	3.57	5	48

Failure properties (strength, tension), wall thicknesses, zero-pressure geometry, and histological data are information that cannot be retrieved without excising the entire aneurysm. In the past, Martufi et al. used the radius of curvature to predict the aneurysm wall thickness and Vande Geest et al. proposed a stochastic model that predicted failure strength of the aneurysm in

order to calculate the Rupture Potential Index (RPI) of an aneurysm (Equation 7)[48,49,54]. The study completed acquired a large density of direct wall thickness measurements as well as failure properties of ruptured and unruptured aneurysms[6,8]. Table 3 (adapted from Raghavan et al 2011) corresponds to all the aneurysms seen in Figure 9 and gives basic background information of each aneurysm.

Raghavan et al. tested the hypothesis of whether or not ruptured aneurysms were weaker than unruptured aneurysms[6]. It was found that ruptured aneurysms were not weaker (on average) than unruptured aneurysms for the given study population. Figure 12 represents the aneurysm diameter and failure tension. Regardless of ruptured or unruptured status and diameter, the failure properties of the aneurysms were found to be statistically insignificant as the ruptured aneurysms were found to be within the range of the minimum failure

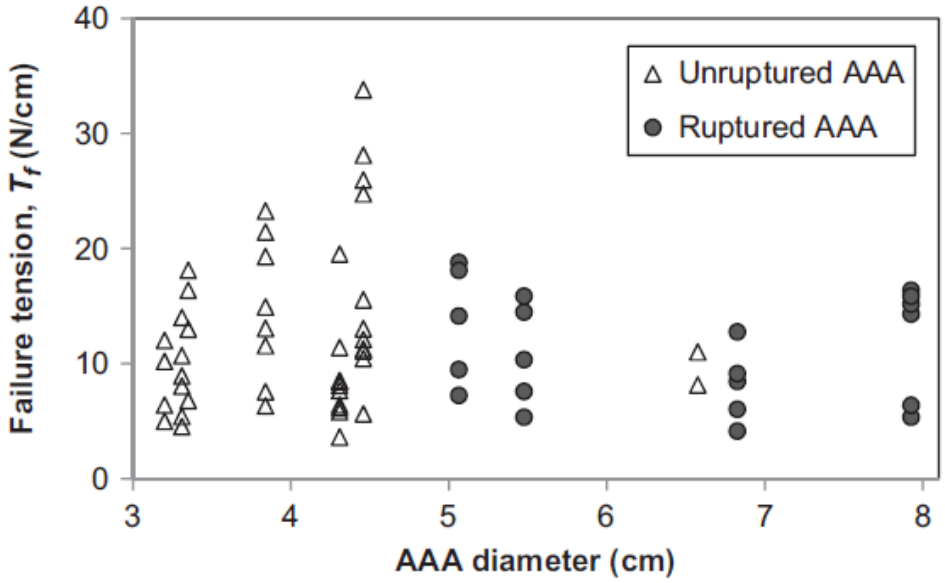

Figure 12: Failure tension in ruptured and unruptured AAA (Raghavan et al 2011).

tension of the unruptured aneurysms.

1.6 – VARIABLE WALL THICKNESS HETEROGENEOUS FINITE ELEMENT MODEL OF RUPTURED AND UNRUPTURED ABDOMINAL AORTIC ANEURYSMS

A variable wall thickness heterogeneous material finite element model of four ruptured and nine unruptured abdominal aortic aneurysm was generated with the measured data from Raghavan et al 2011[6]. In the previous study, failure metrics (stress and tension) were compared between ruptured and unruptured AAA and found that on average there was no statistical difference between ruptured and unruptured failure properties. A computational study that included the measured data (wall thickness, failure stress, failure tension and elastic properties) was developed to compare the pressure induced wall tension and

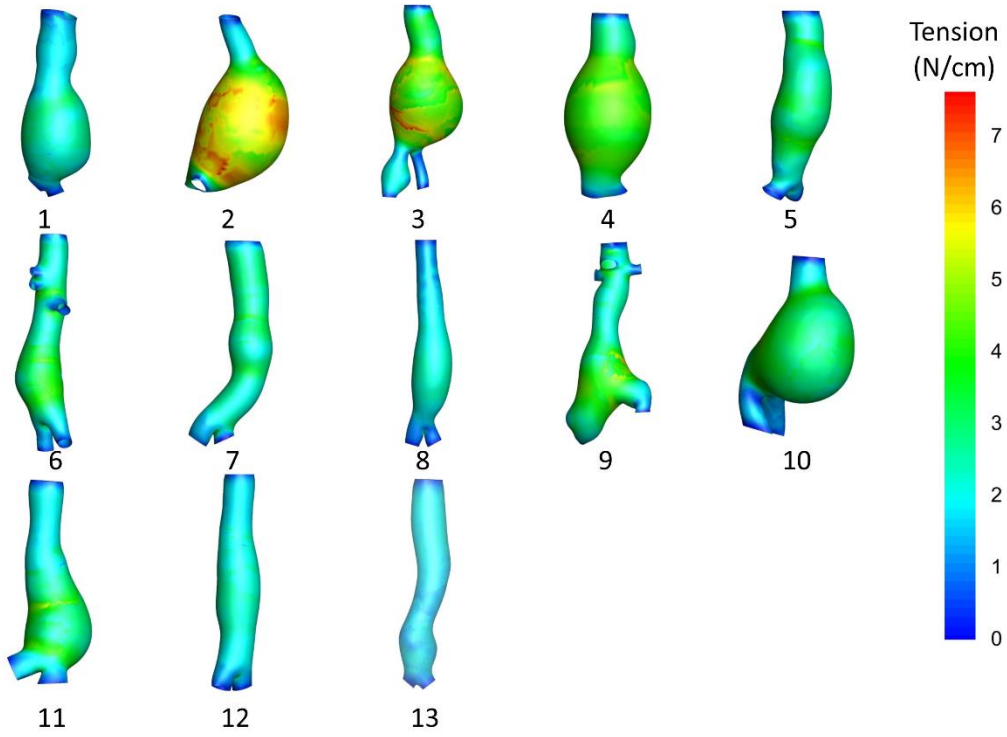

Figure 13:Pressure induced wall tension results for four ruptured AAA (aneurysms 1-4) and nine unruptured AAA (aneurysms 5-13)

stress between these two groups. Figure 13 represents the pressure induced wall tension in four ruptured and nine unruptured AAA.

The data was taken from four ruptured and nine unruptured infrarenal aortic aneurysm that were harvested from cadaver's post-mortem at the University of Sao Paulo School of Medicine. The AAA were pressurized to 5 mmHg with a shape conforming compliant balloon and placed on hooks. 36 photographs were taken in 10^{o} increments on a plain green background (Figure 14) and taken around the cranio-caudal axis of the aneurysm to capture two-dimensional shape information. Wall thicknesses were measured around 35 sites per aneurysm and an average of six uniaxial extension tests were

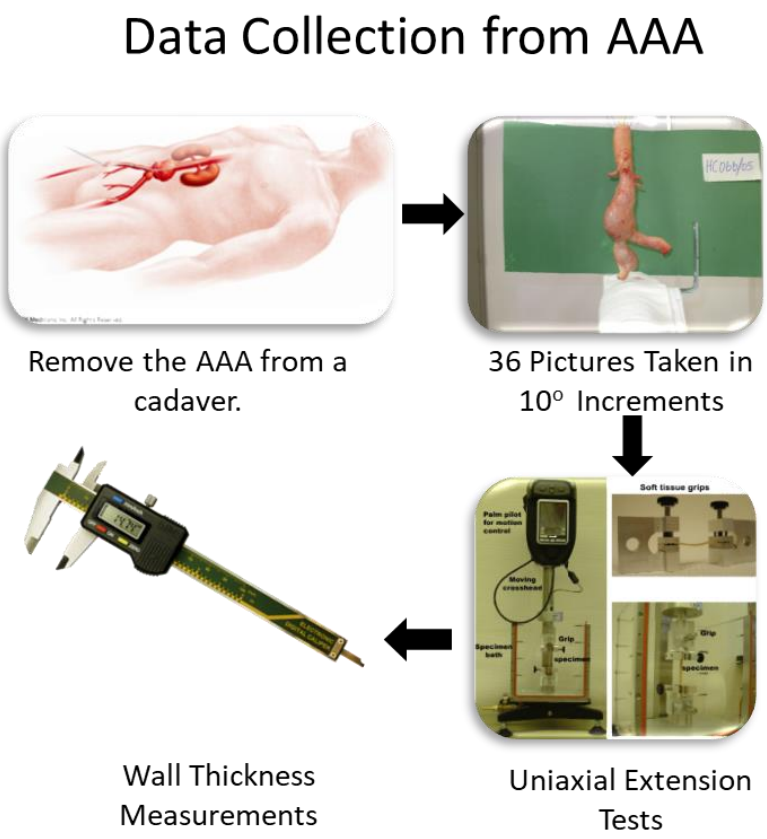

Figure 14: Process to remove AAA and retrieve shape information, material data and wall thicknesses

performed per aneurysm. For elastic properties, α and β, the parameters of the finite elastic isotropic incompressible two-parameter model reported by Raghavan and Vorp, 2000 were estimated using the Levenberg – Marquardt[55,56] damped least-squared method for each stress-strain curve. The minimum alpha value allowed was 3 N/sq.cm to ensure convergence of the heterogeneous material computational model. The surface geometry of the AAA were reconstructed using shape from silhouette techniques performed in 3DSOM (CDSL Limited, Long, England) from a voxel carving technique proposed by Hong et al.[57] . The reconstruction method included wrapping the surface geometry with a texture based on the RGB data from the photographs. A map of where thicknesses and material properties were measured were marked by a vascular surgeon and used as reference to export data points that relayed the measured information. For the uniaxial specimens that were marked on the aneurysm, the center point was chosen as the location of the elastic and failure properties. Additional surface preserving Laplacian smoothing was performed in Meshlab (Visual computing Laboratory, Pisa, Italy). With the surface geometry reconstructed and the measured points accounted for, an interpolation of these measured points on a scattered mesh were needed. The measured data included failure stress, failure tension, wall thicknesses, the α and β elastic parameters. A geodesic distance nearest neighbor nonlinear weighted scattered data interpolation algorithm was developed to interpolate the aforementioned scalar values from the set of known locations to the set of unknown locations on

the surface mesh (Figure 15). The overall schema of the interpolation algorithm was to inversely weight the four closest known locations to an unknown location.

First, the geodesic distances from each of the measurement sites to all

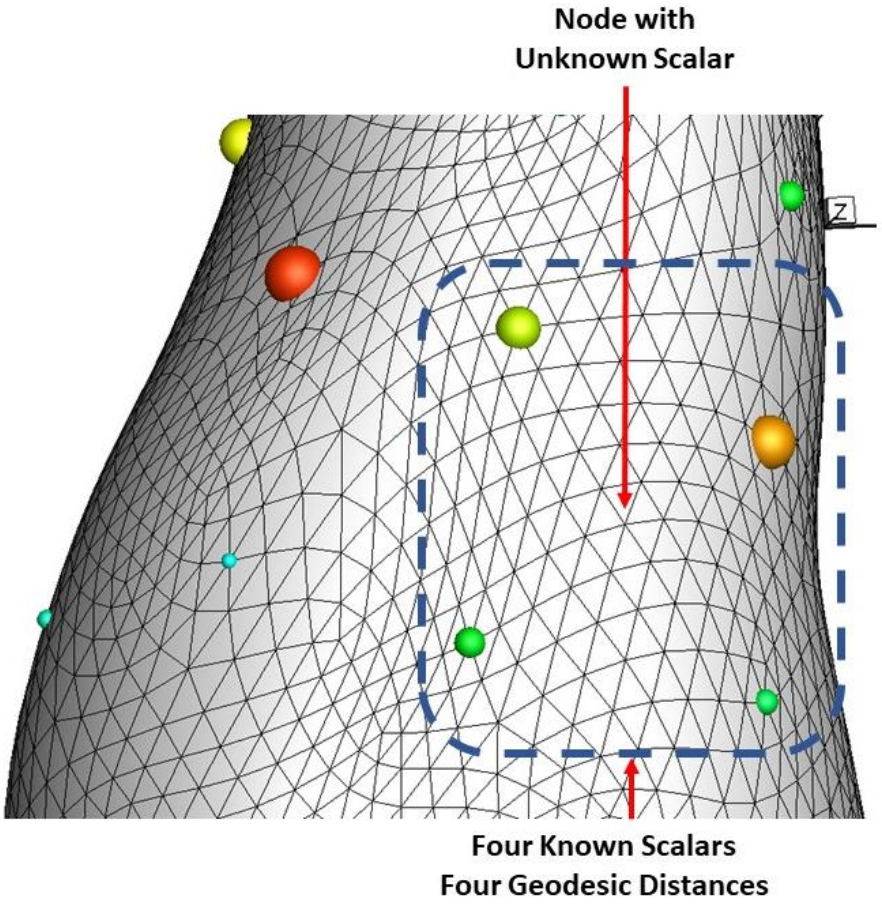

Figure 15: Region of known scalars that are closest to the unknown scalar at node i.

nodes in the surface mesh were computed. For a node i, for which the interpolated thickness t_i needs to be determined. Its nearest m neighbors with measured thicknesses $t_{i,1}$, $t_{i,2}$,… and $t_{i,m}$ are at geodesic distances $d_{i,1}$, $d_{i,2}$,….and $d_{i,m}$ from node i (nearest to farthest). From this, the normalized geodesic distances is written as (Equation 2),

Equation 2: Formula to normalize geodesic distances

$$g_{i,j} = \frac{d_{i,j}}{\sum_{k=1}^{m} d_{i,k}}$$

The interpolated thickness of *i*th node is defined as Equation 3.

Equation 3: Interpolated thickness from weighted terms and known thickness values.

$$t_i = \sum_{j=1}^{m} w_{i,j}\, t_{i,j}$$

where, $t_{i,j}$: $1 \le j \le m$ are the thicknesses of the *m* nearest neighboring nodes with measured values (*j*=1 represents the nearest neighbor to node *i*; *j*=2, the next nearest; and so on), and

Equation 4: Nonlinear weights for interpolation.

$$w_{i,j} = \begin{cases} (1 - g_{i,j}) & j = 1 \\ (1 - g_{i,j}) \prod_{k=1}^{j-1} g_{i,k} & 1 < j < m \\ \prod_{k=1}^{j-1} g_{i,k} & j = m \end{cases}$$

It can be shown that the sum of weights in Equation 4, $\sum_{j=1}^{m} w_{i,j} = 1$

Equation 4 ensures that the nearest neighbor is weighted the most followed by the next nearest neighbor and so on with a nonlinear drop in weights. In this

study, *m* = 4 (that is, the interpolation was performed using four nearest neighbors). Therefore, Equation 4 would reduce to Equation 5,

Equation 5: Four weights in interpolation method.

$$w_{i,1} = 1 - g_{i,1}$$

$$w_{i,2} = (1 - g_{i,2})g_{i,1}$$

$$w_{i,3} = (1 - g_{i,3})(g_{i,2})(g_{i,1})$$

$$w_{i,4} = (g_{i,3})(g_{i,2})(g_{i,1})$$

Figure 16 represents the original thicknesses and how they were interpolated on the surface of the AAA geometry. Interpolation was performed

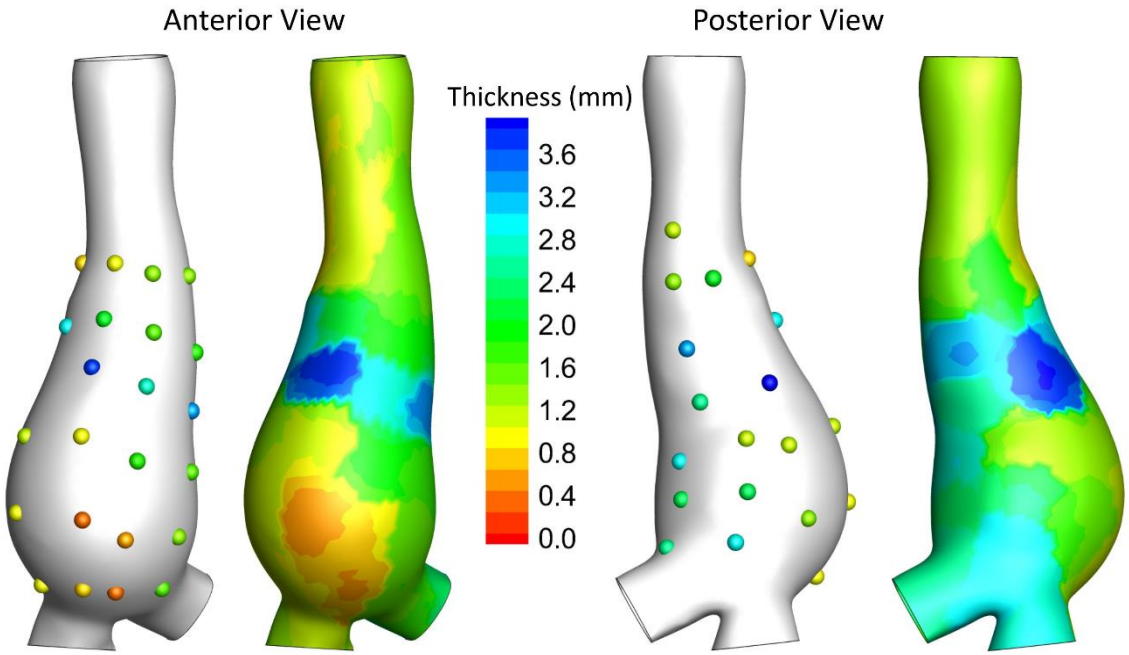

Figure 16: Anterior and posterior view of the original and interpolated thickness.

with the material properties as well, but due to the scarcity of the material data, the interpolated values were not as accurate as thickness.

A finite element model of all thirteen AAA at zero pressure geometry using shell elements (S3R Abaqus) with variable wall thickness and material heterogeneity was created in Abaqus (3DS, Waltham, MA). The simulations were performed by constraining the distal and proximal boundary nodes in all directions (x, y, and z) and rotationally (about the x, y and z axes). A pressure of ideal systolic pressure 120 mmHg (1.57 N/cm^2) was applied as a distributed load at the surface of each element as patient specific blood pressure was unavailable. Comparisons of peak wall stress (PWT), peak wall tension (PWT) and tension to failure tension ratio (TFT) were made Figure 15, peak values were chosen as the 99th percentile. It is reported that there was no statistical difference between the two groups, but there was a trend towards statistical significance between peak wall tension in ruptured AAA and unruptured AAA. The average peak wall tension (PWT) defined as 99th percentile value within the spatial distribution in ruptured group was higher than that in the unruptured group, but without statistical significance (mean ± SD: 4.98 ± 1.37 versus 3.49 ± 0.91 N/cm; P = 0.074; Figure 17). The peak wall stress was also higher in the ruptured group without statistical significance (47.5 ± 12.0 versus 41.6 ± 17.6 N/cm^2; P = 0.17). The peak tension to failure tension ratio was higher in the

ruptured group also without statistical significance (0.75 ± 0.35 versus 0.44 ± 0.20; p = 0.099).

This study was concluded without finding a definitive causative role of elevated PWS, PWT and TFT as these peak values did not match the rupture location of the four ruptured AAA. However, this was a first step in a comprehensive computational model that took account patient specific failure properties, wall thicknesses and heterogeneous material properties that investigated the roll of these traditional computational indices in AAA rupture.

1.7 – RESEARCH PLAN TO INVESTIGATE MULTIAXIAL FAILURE PROPERTIES AND FAILURE INDICES IN AAA RUPTURE

The aim of the proposed study is to assess multi-axial failure properties through bubble inflation test, compare uniaxial failure and multi-axial failure properties of various tissues and use these findings to gain insights on AAA rupture. To that end, the following aims are proposed:

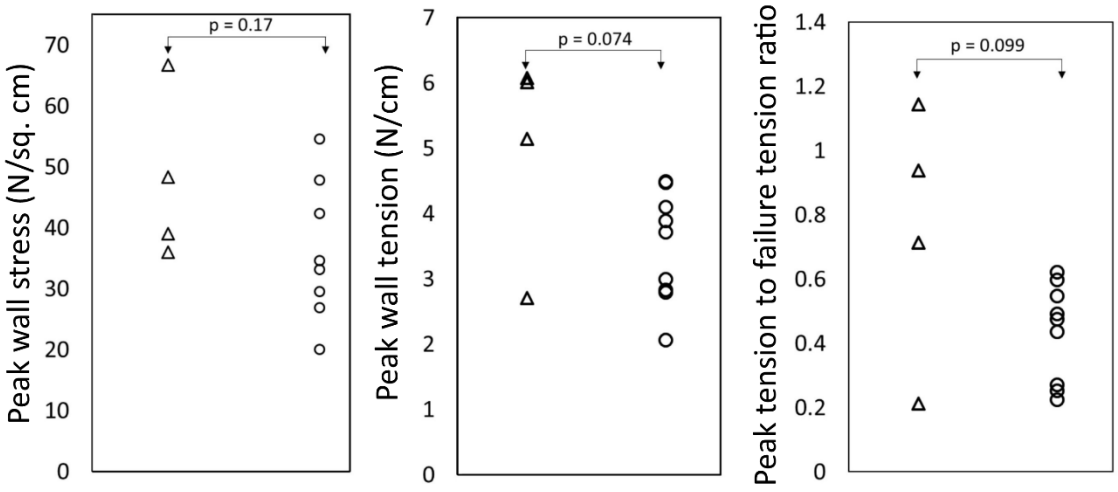

Figure 17: Comparison of PWS, PWT, peak tension to failure tension ratio of ruptured and unruptured AAA.

Aim 1. *Develop a bubble inflation test (BIT) apparatus and testing protocol for studying multiaxial tensile failure properties of soft tissues.*

Aim 2. *Compare failure characteristics gained from uniaxial and BIT methods using various types of soft tissues.*

Aim 3. *Assess various failure criteria using computational model of ruptured AAA.*

Cardiovascular diseases such as cerebral aneurysm and abdominal aortic aneurysms have been extensively studied since their rupture leads to high morbidity and mortality rates[58,59]. Computational modeling of these particular cardiovascular diseases have not established a causative relationship between pressure induced stress and rupture[9,28,39,40,42,45,49,60–62] Failure properties of various types of biological soft tissues have investigated in order to ascertain whether or not these catastrophic biomechanical events can be attributed to material weakness. A comprehensive understanding of failure properties may lead to a deeper understanding by identifying localized weaknesses in the arterial walls of cardiovascular disease. Experiments that have exclusively investigated the material properties of AAA tissue have tested the differences between AAA tissue and normal aortic tissue[3,4,63] the differences in material properties in various regions of the AAA[7] and the differences in material properties between ruptured and unruptured AAA. Raghavan et al found that ruptured AAA was no weaker on average than unruptured AAA which was not consistent with the premise that rupture occurs due to material weakness[6].

Computational finite element models have incorporated material models derived from multi-axial experiments for realistic response to pressure loads. It

was thought that the peak wall stress or stress to strength ratio may predict rupture site or propensity to rupture. Variable wall thickness and heterogeneous material computational models were developed for ruptured (n = 4) and unruptured (n = 9) AAA to further assess the peak wall stress and the stress to strength ratio. It was found that ruptured AAA was not subjected to a higher pressure induced wall stress/tension than unruptured AAA ($p = 0.053$). A major limitation to this study was the lack of uniaxial extension tests performed per aneurysm. A total of thirteen AAA (4 ruptured, and 9 unruptured) was investigated with an average of $n = 6 \pm 1$ strips per aneurysm. The spatial resolution of material properties' measurements was inadequate to find localized weaknesses of the AAA wall. New methodologies that can capture a higher density of material properties are needed to reveal weaknesses and material heterogeneity.

Uniaxial extension tests have been used in the past for failure properties[3,4,6,9,12,21,22,64]. However, it remains unclear whether the uniaxial extension failure properties are adequately representative of multi-axial nature of failure in AAA during rupture. Further development of the BIT will allow for a higher density of measurement of multi-axial failure properties in biological soft tissues and synthetic materials. Comparing failure modes using BIT and uniaxial extension tests of the proposed materials will help assess the validity of retrospective studies that measured failure solely with uniaxial extension. Bovine aorta, bacterial cellulose, elastane (Spandex), and silicone will undergo both uniaxial extension testing and BIT. The specific aims of this proposed project are

to design and fabricate a BIT apparatus, evaluate and compare failure properties inferred from BIT with those of uniaxial extension tests and assess multiaxial failure properties to provide insight into AAA rupture.

Aim 1: Develop BIT apparatus and testing protocols for studying multiaxial tensile properties of soft tissues.

Multiaxial failure properties have been studied by various groups with varying degrees of information that can be extracted from the bubble inflation test[14,33–37]. Two different BIT apparatus' will be built, one that is manually pressurized with manual measurements of optical strain (Manual BIT) and the other that is automatically pressured with automated optical strain measurements (automated BIT). The manual BIT allows for a high density of failure properties to be measured without the need for cutting while the automated BIT requires individual specimens to be procured from a sheet of material. A simple pressure volume relationship will be acquired from the manual BIT and three-dimensional surface reconstruction will be performed using the automatic BIT to capture material heterogeneity. Both manual and automated BIT will use a compliant balloon and an incompressible fluid (H_2O) as a pressurization media. Differences in pressurization of specimens are through a manual screw-type syringe and a PID controlled linear actuator for regulated pressurization.

Aim 2: Compare failure characteristics gained from uniaxial and BIT methods using various types of soft tissues.

Biological soft tissue samples from bovine aorta will be acquired to test failure in anisotropic biological tissues. Bovine aortic tissue will be examined via a uniaxial extension test and the aortic specimens will be oriented longitudinally

and circumferentially[65] near the specimen orifice area of the multiaxial BIT tests. The BIT will be deployed using the three modules found in Aim 1. The BIT will be loaded with biological tissue samples irrespective or orientation. The study of multi-axial extension of the bovine aorta will be compared to longitudinally and circumferentially oriented uniaxial extension tests in hopes to reveal any correlation between multiaxial failure and oriented uniaxial failure. Additionally, bacterial cellulose will also be tested using the same protocol as the fiber orientation of cellulose is highly randomized. A non-fibrous homogeneous isotropic manmade material, XP – 565 from Silicones Inc, will be used to create sheets of silicone to be tested with bot the BIT and uniaxially. Comparisons will be made with this material to determine if there are any differences between multiaxial failure and uniaxial failure materials for this type of material.

Aim 3. Assess various failure criteria using computational models of ruptured AAA.

There is little consensus for a failure criterion for aneurysmal aortic tissue. Traditionally, investigators employing finite element analyses of patient-specific AAA have used either von Mises Stress or maximum principal stress whose spatial peak values were compared with ultimate or yield stress determined through uniaxial extension experiments. A general criterion laid out was that when the pressure-induced maximum principal stress exceeded ultimate strength, then rupture would occur or is imminent. However, this rests on the premise that maximum principal stress is the appropriate failure criterion. This is certainly not farfetched because the aortic wall is made of structural fibers and maximum normal (diagonal) stresses are likely what causes the failure of

individual fibers at a microstructural level which aggregate into macroscopic rupture. However, rigorous studies that evaluate the validity of this premise are lacking. The above premise does not account for the fact that the material may be anisotropic and is made primarily of structural fibers – mainly collagen. It is conceivable that, given the complex fiber alignments, fiber-fiber and fiber-matrix interactions, failure of the aneurysmal aortic tissue is not necessarily a result of maximum principal stress along one principal direction, but rather a result of more complex interactions between principal stresses in multiple directions or perhaps a result of the strain energy stored. In other words, it is conceivable that rupture risk is associated with some other index of the stress field than simply maximum principal stress.

The controlled comparisons performed between uniaxial and inflation experiments and the induced-defect experiments in aim 2 will provide valuable insights into precisely the above issue. For example, it is plausible that there exists a correlation between the failure stresses obtained from uniaxial extension tests and BIT for the same specimen types, which may be used to derive a stochastic relationship. Or perhaps, another stress metric such as strain energy at failure or stress intensity factor may be most associated with weakness and failure susceptibility. Thus, the results from aim 2 will be leveraged to gain a deeper understanding of AAA rupture by performing new retrospective studies. For the four AAA described in the preliminary study which were ruptured, finite element analysis results will be retrospectively assessed. Spatial distributions of various stress and strain indices such as maximum principal stress, maximum

principal strain, and von Mises stress will be taken into consideration. Because the location of rupture in these AAA are known *a priori,* such comparisons would allow us to assess which failure criteria are most likely to be associated with AAA rupture

CHAPTER 2 - AIM I: DEVELOPMENT OF THE BUBBLE INFLATION TEST APPARATUS

INTRODUCTION

The bubble inflation test (BIT) apparatus is important in understanding multi-axial failure in biological soft tissues. The ability to extract failure properties subject to a multi-axial load is desirable as it is indicative of how the cardiovascular system is pressurized by the heart. Traditionally, uniaxial extension tests have been the only suitable method for obtaining failure stress and failure tension in biological soft tissues. It remains unclear if the uniaxial extension tests capture the failure properties of fibrous anisotropic biological soft tissues. Various groups have implemented different types of bubble inflation tests to retrieve different levels of information. The development of a manual BIT and automatic BIT allow for varying degrees of biological soft tissue interrogation and their development is further discussed in sections 2.04 and 2.05.

Two different BIT apparatus' were developed with differing purposes. The manual BIT was developed to test a large number of specimens on a single sheet of biological soft tissue in order to extract failure properties without procuring each specimen for experimentation. Reducing specimen procurement time and minimizing the number of physical cuts to the material helps increase the reproducibility and implementation of the manual BIT. The optical strain measurements are simple that allow for non-technical operators of the manual BIT to quickly extract failure properties. It is also noted that the manual BIT is easily manufactured (3D printed) and can be replaced readily if any components

were to fail. The manual BIT has the advantage of experimentation on a large number of adjacent samples in a single sheet of material (bacterial cellulose, aortic tissue, etc.). The motivation of recording a larger amount of failure properties is to understand if AAA rupture is caused by localized material weakness. A simple and easy to use design is a desirable feature in the operation of the manual BIT to quickly load and unload samples. Albeit, heterogeneity may not be captured, pressure-volume relationship, failure stress and maximum rupture pressure can be acquired. The pressure and volume information retrieved from the manual BIT is similar to that of other groups that have implemented a bubble inflation test[14,29,36]. Mohan et al attempted to elucidate the relationship between multiaxial failure and uniaxial failure properties but were unable to due to practical challenges in their experimental apparatus[35]. The manual BIT tests multiaxial failure properties in fibrous, anisotropic biological soft tissue and manmade homogeneous isotropic tissues to compare multiaxial failure properties with uniaxial failure properties.

Table 4: Differences in the manual BIT and automated BIT

BIT Type	Stress?	Volume?	Single Sheet	Easy to use?
Manual BIT	Yes	Yes	Yes	Yes
Automatic BIT	Yes	Yes	No	No

The automatic BIT requires specimens to be procured from a source material and clamped onto a stage where a two-camera system has the ability to capture geometric changes during an automatic BIT test. It is unclear whether cutting of specimens has an overall weakening effect on specimens during failure

testing. Although the ease of use is hindered due to the procurement and loading/unloading of specimens, surface geometry can be captured unlike the manual BIT apparatus. Table 4 summarizes the advantages and disadvantages of each BIT type. The development of both the manual and automatic BIT will provide invaluable insight to localized weaknesses in samples, multi-axial failure properties and material heterogeneity.

2.1 – THE THREE MODULES OF THE BIT APPARATUS

The BIT apparatus has three modules that are necessary to perform rupture tests irrespective of manual or automatic operation. These modules are identified as the clamp, pressurization and optical strain measurement modules (Figure 18). The automatic BIT and manual BIT have variations to how each module is implemented and will be further discussed later in sections 2.4 through 2.8. Variations of each module provide a difference in how the user applies pressure to the specimen (screw-type manual and PID-controlled syringe pump) and the manner in which the pressure-volume relationship is recorded. In both types of BIT experiments, the stress can be captured independent of pressurization method and volume measurement (Section 2.4.4).

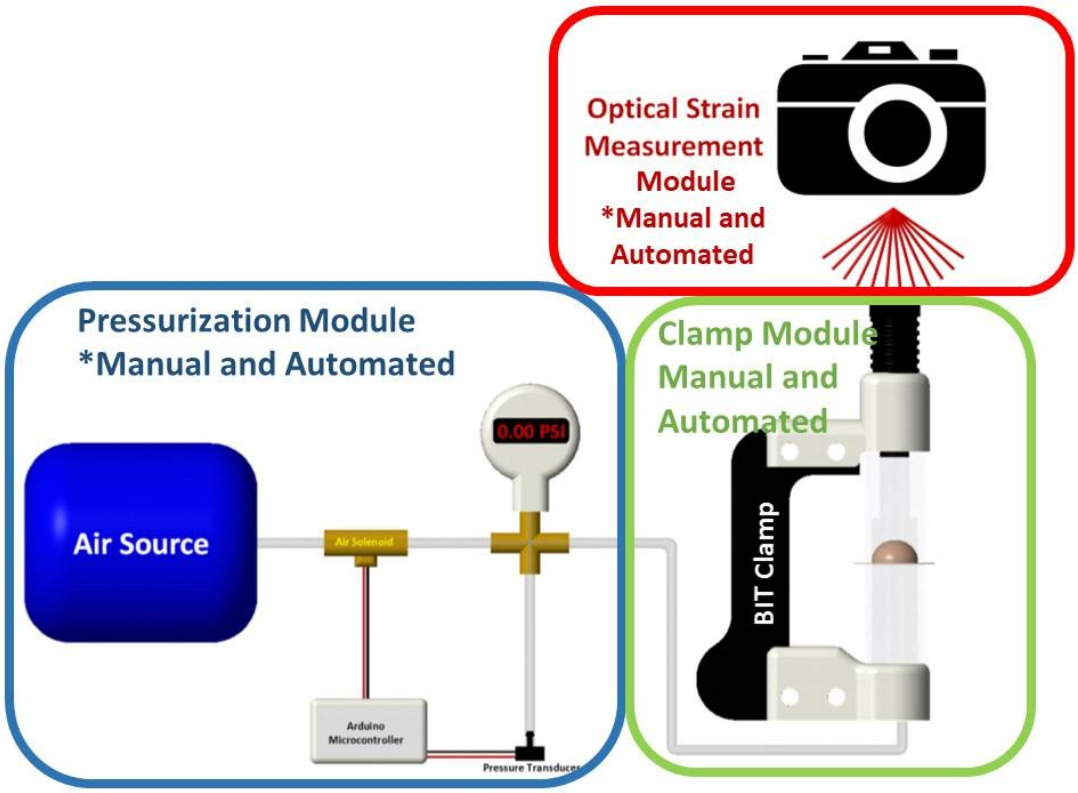

Figure 18: The three modules needed for manual and automated BIT.

2.1.1 - Clamp Module

The clamp module is composed of a pressurization chamber, a physical clamping mechanism of a biological soft tissue sample, and stage pieces that prevent the sample from slipping. The manual BIT has an upper and lower acrylic pressurization chamber, the lower chamber for the compliant balloon and the upper chamber for the specimen to expand during inflation. The stage pieces ensure that no slipping occurs between the clamping pieces and the specimen while reducing the specimen orifice area. The specimen orifice area is decreased to ensure that the specimen does not come into contact with the pressurization chamber wall (see section 2.3).

2.1.2 - Pressurization Module

The pressurization module serves as the means to pressurize specimens as well as record pressure information in real time through different modes. The pressurization module allows for the BIT operator to visually read the pressure as it increases during an experiment. As for the automated BIT, the pressure values are visually verifiable and interpreted through a microcontroller using a pressure transducer. Overall, the pressurization module includes a digital pressure gauge (pressure transducer for automatic BIT and a pressure gauge for manual BIT) and a pressurization source. Initially the pressure media was air, but eventually a syringe with an incompressible liquid (H_2O) was used as air requires a large amount of volume to achieve higher pressures do to its compressibility properties. Colored water (food dye) was used to visually identify fluid movement as well as check for any leaks in the system during the apparatus design phase.

2.1.3 - Optical Strain Measurement Module

Optical strain measurements are needed to capture the pressure – volume relationship information. The manual BIT utilizes a simple water column for recording volume displacement as the sample is pressurized while the automatic BIT uses a two-camera system to reconstruct the sample under pressure. Manual BIT experiments are video recorded and a post processing step is required to retrieve the pressure-volume data. The automated BIT also utilizes a post processing step from sets of two orthogonal digital photographs to reconstruct the surface. The reconstruction method is further described in section 2.3.4 and requires two orthogonal 2-dimensional images to be taken

simultaneously. The volume is calculated using the 3-dimensional surface reconstruction from two images during experimentation and a pressure-volume relationship is plotted (section 2.9).

2.2 – PRELIMINARY MANUAL BIT STUDIES IN BRAZIL

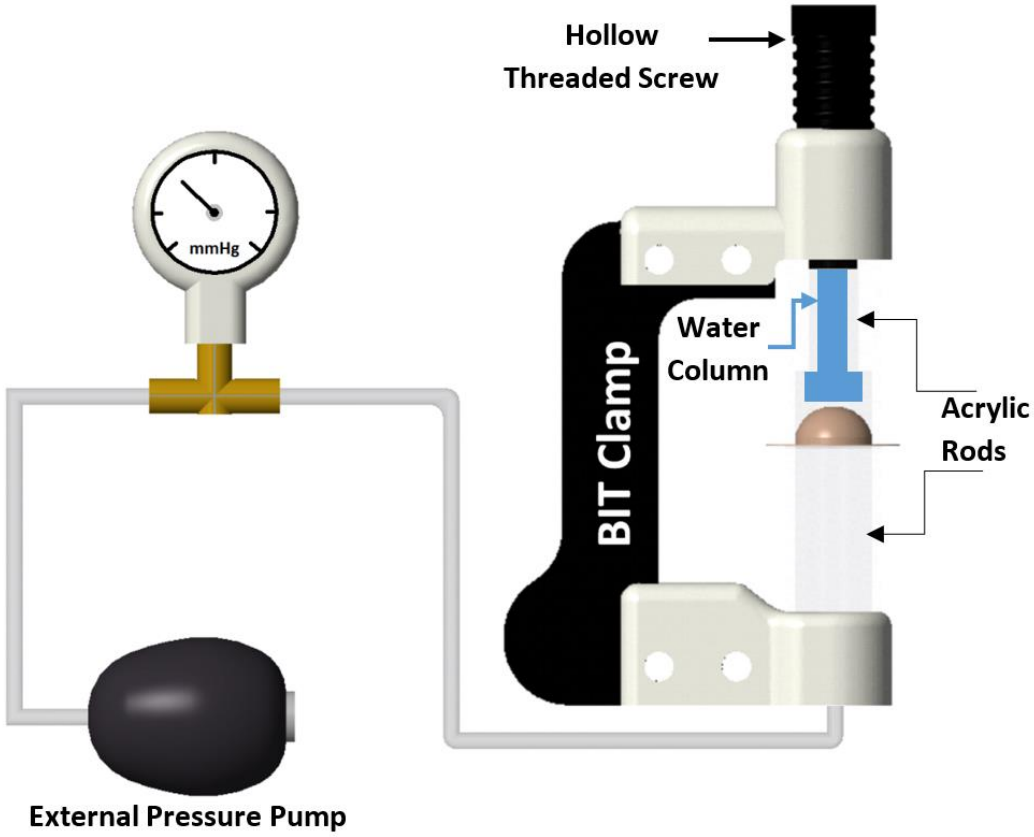

Figure 19: BIT apparatus with hand pump using air.

A 'proof of concept' version of a manual BIT apparatus was developed using rapid prototyping, fused deposition modeling (FDM)[66,67] 3D printing with polylactide (PLA)[68] that featured a single sided clamp, air pressurization source from a blood pressure cuff hand pump, blood pressure gauge and a water column to measure volume displacement (Figure 19). The pressure gauge had

an upper limit of 300 mmHg and the hand pump had a physical limit of roughly 500 mmHg while pumping air.

Preliminary studies using the manual BIT were performed at the University of Sao Palo with human aneurysmal aortic tissue. It was quickly realized that the maximum pressure of 500 mmHg was insufficient in creating rupture of human thoracic aorta samples. The BIT apparatus was retrofitted with a Presta valve[69] (bicycle tube valve) that had a maximum pressurization limit of 100 pounds per square inch (psi).

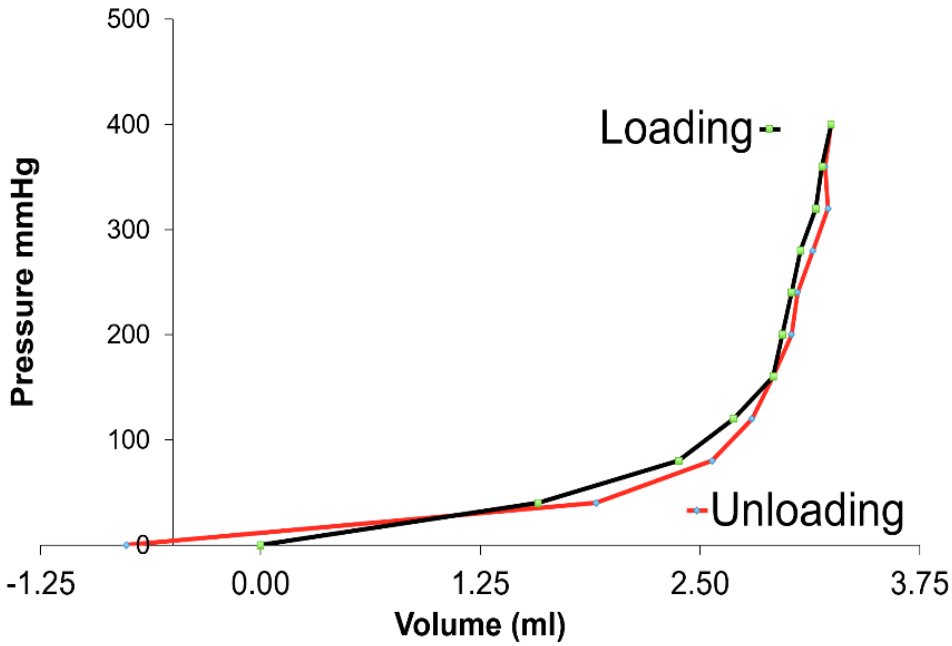

Figure 20: Pressure - volume relationship in human aortic tissue.

Elastic properties of the loading and unloading curve using the BIT is shown in Figure 20. The load deformation curve exhibited nonlinear behavior with increasing stiffness as the pressure increased. It was also noted that the water column had a negative displacement indicating plastic deformation and material hysteresis. Additional design iterations were made by creating two

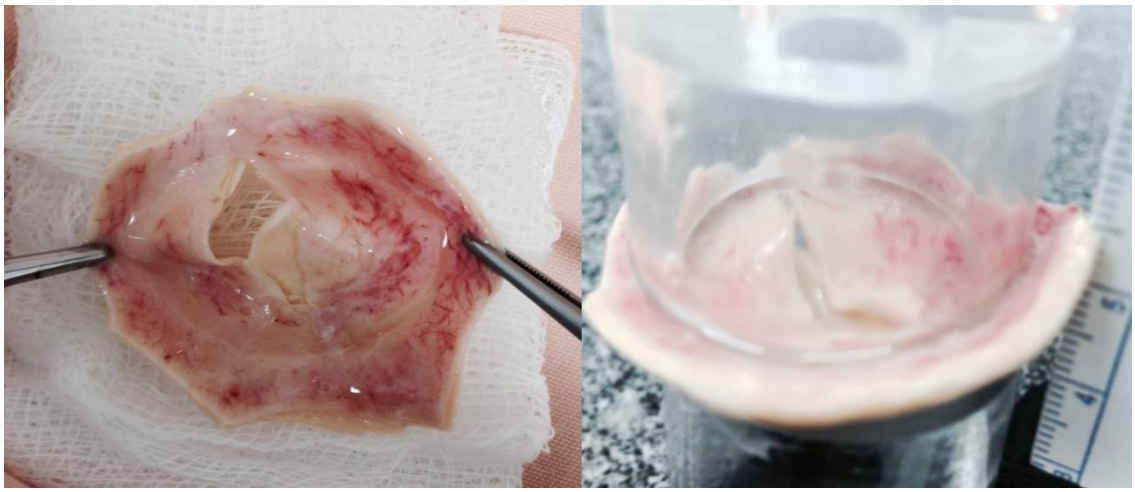

Figure 21: Line rupture in human thoracic aortic tissue.

additional BIT apparatus' one with a doubled specimen area and the other with the Presta valve. Figure 21 displays multi-axial failure of Thoracic aortic tissue using the BIT apparatus. Rupture of the sample occurred at the center of the

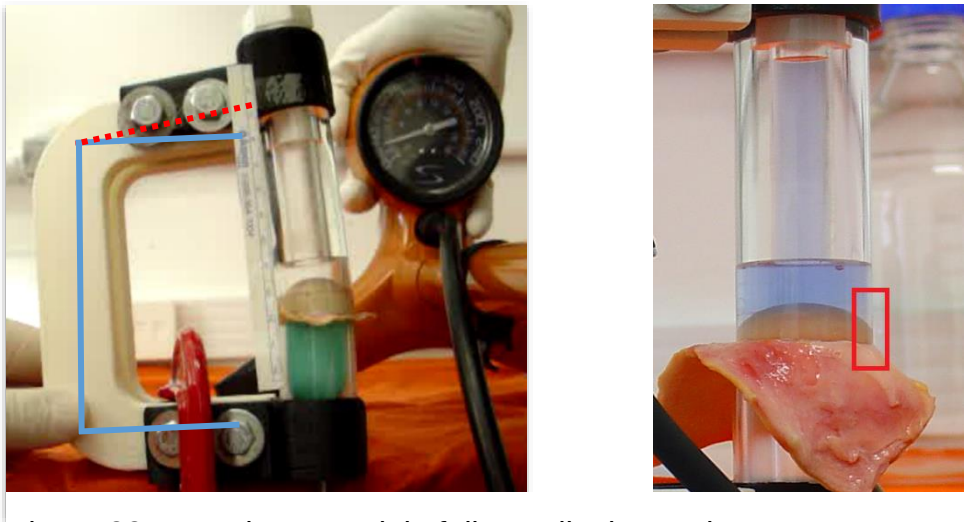

Figure 22: BIT clamp module failure, slipping and pressure attenuation.

specimen where the peak stress is located. The BIT apparatus began to fail over time as samples were subsequently loaded and unloaded. Albeit, the initial experiments were successful, there were several drawbacks to the BIT apparatus design that include: Clamp frame bending (Figure 22) under pressurization, specimen touching the wall of the clamping chamber during pressurization, slipping of the sample in between the clamping pieces, and that a large volume of air is necessary to achieve higher rupture pressures. The blue indicates the intended frame angle and the red dotted line indicates the bending that occurred. Design changes to the manual BIT clamp frame are discussed in section 2.4.2.

2.3 - ADDRESSING SHORTCOMINGS OF THE PRELIMINARY BIT APPARATUS

Revisions to the existing manual BIT design were necessary due to the clamp frame deforming during pressurization, pressure attenuation, specimen slipping and the requirement for a large volume of air to invoke specimen rupture. The design changes that affect both the manual and automatic BIT were the specimen stage pieces and changing the pressurization medium from air to an incompressible fluid (H_2O).

2.3.1 - Stage Pieces

Initial stage pieces were designed to address stress attenuation of the specimen by touching the side wall of the acrylic clamping pieces and the slipping of the specimen during pressurization. Figure 23 was proposed as a method to solve both issues by decreasing the specimen orifice diameter

(reduction from 25.4 mm to 17 mm) and adding teeth to grip the specimen when clamped.

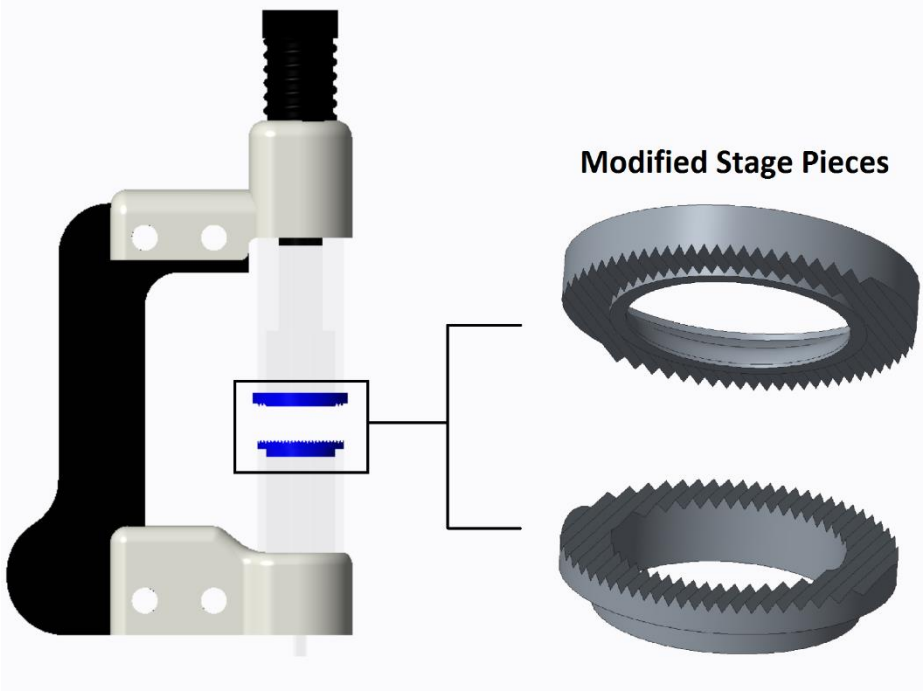

Figure 23: Modified stage clamps to prevent pressure attenuation.

The modified stage pieces prevented specimens from touching the side wall, but it did not prevent slipping. There were limitations to the resolution in which the FDM 3D-printer could reliably print the serrated teeth. The specimen would not clamp reliably between the 3D-printed stage pieces and slipping

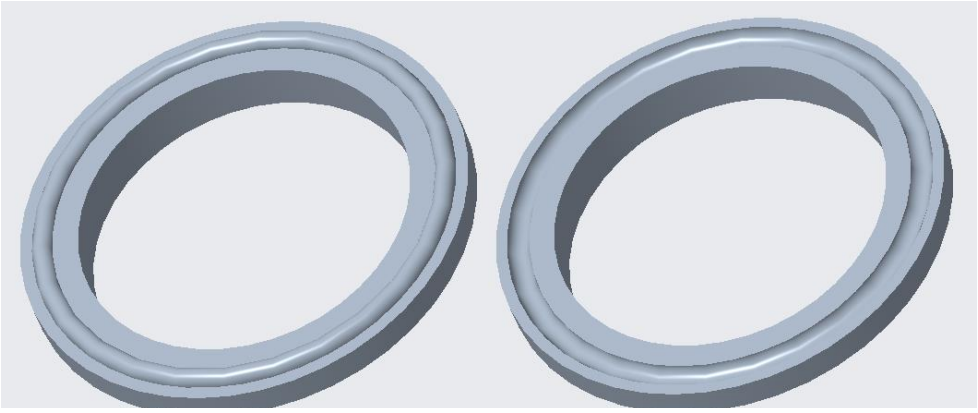

Figure 24: Radial clamp ring to prevent slipping.

occurred when pressurized. Additional attempts to create radial ring also failed due to the limitations of the FDM 3D printer (Figure 24).

The next step was to find a suitable manufacturing technique that could address the limitations that 3D printing had. It was found that laser cutting (50W CO_2 laser) addressed the manufacturing concerns that were mentioned previously. The material for the stage clamp pieces were 3 mm thick sheets of extruded acrylic. Extruded acrylic is desirable as it leaves no rough edges during laser cutting operations due to flame polishing[70] while allowing for variable depths of cut. Having no rough edges ensures that no stress concentrations would be present on the specimen during pressurization. The finalized laser cutting settings were 32.5 Watts (W) at 6 mm/min for cuts and 32.5 W at 100 mm/min for the gripping lines. Figure 25a represents the finalized design of the stage pieces and Figure 25b is representative of the completed stage pieces.

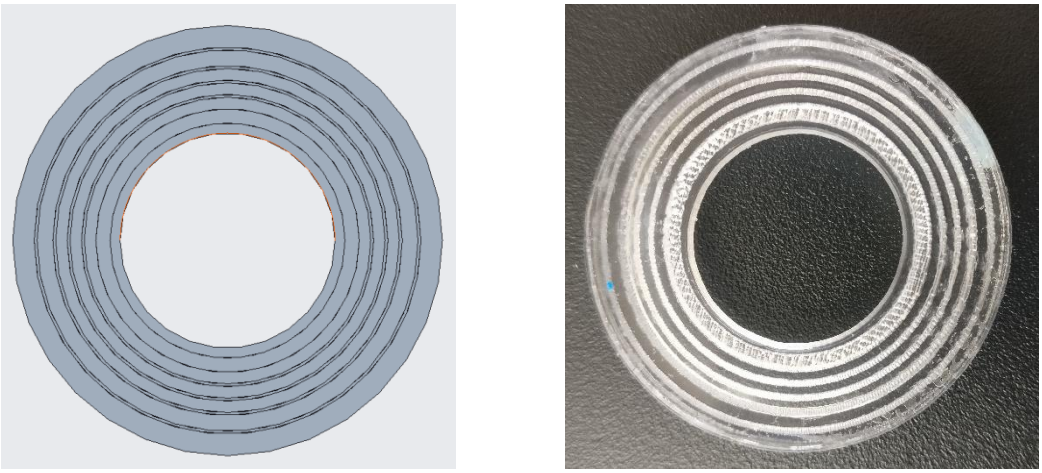

Figure 25 (a): Graphic of proposed clamp piece (b) Laser cut clamp piece

In subsequent experiments using the laser cut acrylic stage pieces, it was found that there was no evidence of slipping in biological soft tissues (bovine and bacterial cellulose) and in silicone. The clamping of the stage pieces left impressions on the various materials without any perceptible elongations that would suggest slipping had occurred during a BIT experiment. Figure 26 and Figure 27 show the impressions of the clamp on the bovine aorta and bacterial cellulose.

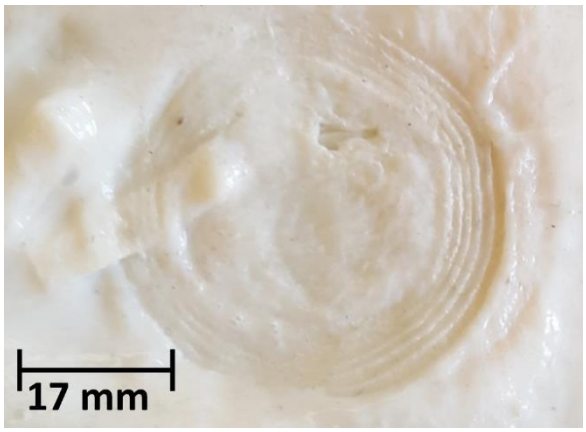

Figure 26: Gripping marks indicate no slipping in bovine aortic samples.

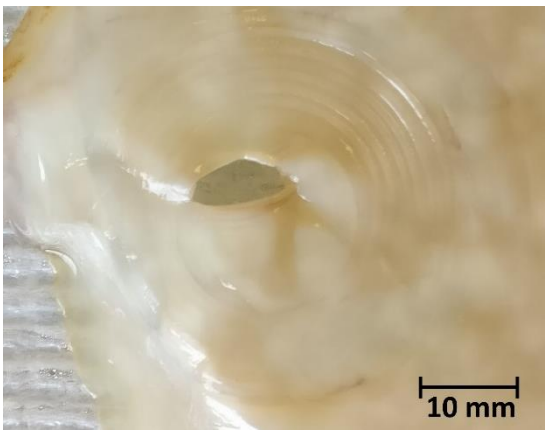

Figure 27: Gripping marks indicate no slipping in bacterial cellulose.

2.3.2 - Pressurization Media

The preliminary experiments performed in Brazil used a bicycle pump to pressurize the thoracic aorta specimen to rupture. However, compressibility of air and the inability to provide constant pressurization created practical challenges to the BIT pressurization module itself. A decision was made to use an incompressible fluid (H_2O) to reduce the amount of volume necessary to pressurize tissue to rupture. A modified 30 milliliter (mL) syringe was used to pressurize the manual BIT by mechanically screwing the plunger during a BIT experiment along with a compliant balloon.

The maximum pressure that could be achieved by the manual BIT was 100 pounds per square inch (psi) that was verified in closed loop operation with a digital pressure SSI., Technologies pressure gauge (+/- 0.1 % accuracy). The pressurization module for the automatic BIT had a maximum pressure of 40 psi limited by the force generated by a linear actuator (discussed in section 3.3.2).

2.3.3 - Effects of using a compliant balloon

It was necessary to find a compliant balloon that could conform to the surface of any sample during a BIT experiment, that would not have any pressure attenuation effects and that would prevent any liquid from leaking during pressurization. A decision was made to use a thin compliant latex balloon that was cylindrical with the potential for a large volume capacity. Two

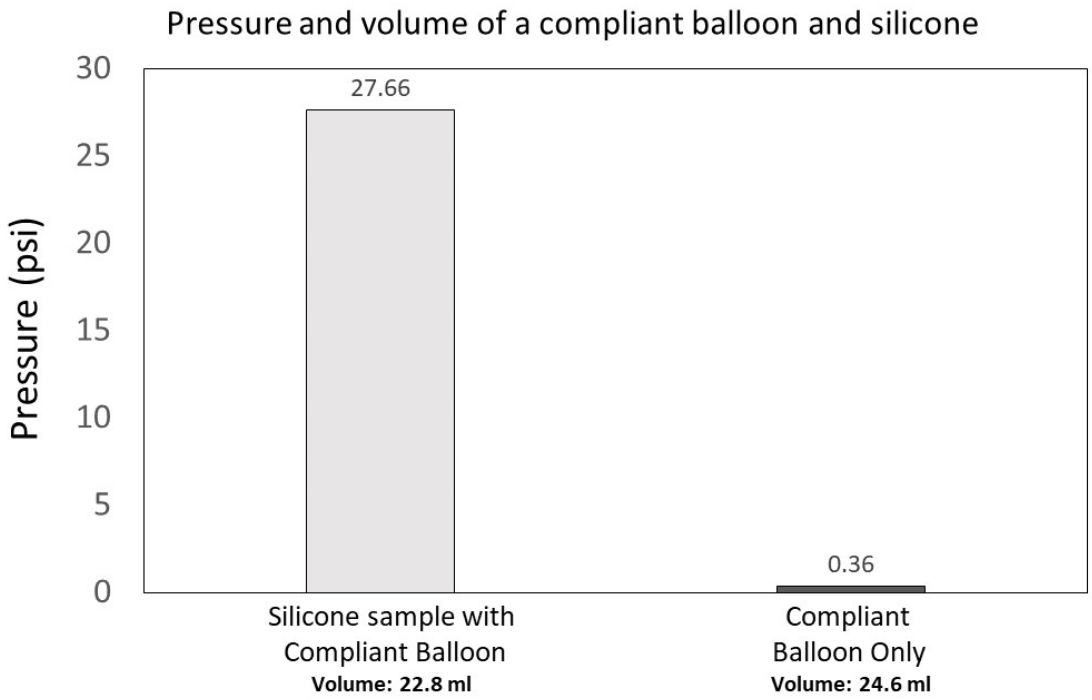

Figure 28: Pressure at a similar volume while using a compliant balloon, compliant balloon with silicone sample.

experiments were developed to ensure that the latex balloon chosen did not exhibit significant p attenuation. The first experiment filled the entire upped BIT chamber with the compliant balloon and measure the pressure without a specimen loaded. A 4.00 mm thick isotropic homogeneous silicone specimen was loaded into the manual BIT apparatus and pressurized until rupture. The maximum pressure at the given volume were recorded and can be seen in Figure 28.

Figure 29 (a) Compliant balloon filling the upper chamber (b) compliant balloon with a silicone sample filling the upper chamber.

The silicone sample was loaded to its maximum pressure and the volume was calculated. Figure 29a and 29b demonstrates that the compliant balloon filled the lower and upper chamber (24.6 mL) with little pressure (0.36 psi), whereas the silicone sample loaded filled the chamber to 22.8 mL at a pressure of 27.66 psi.

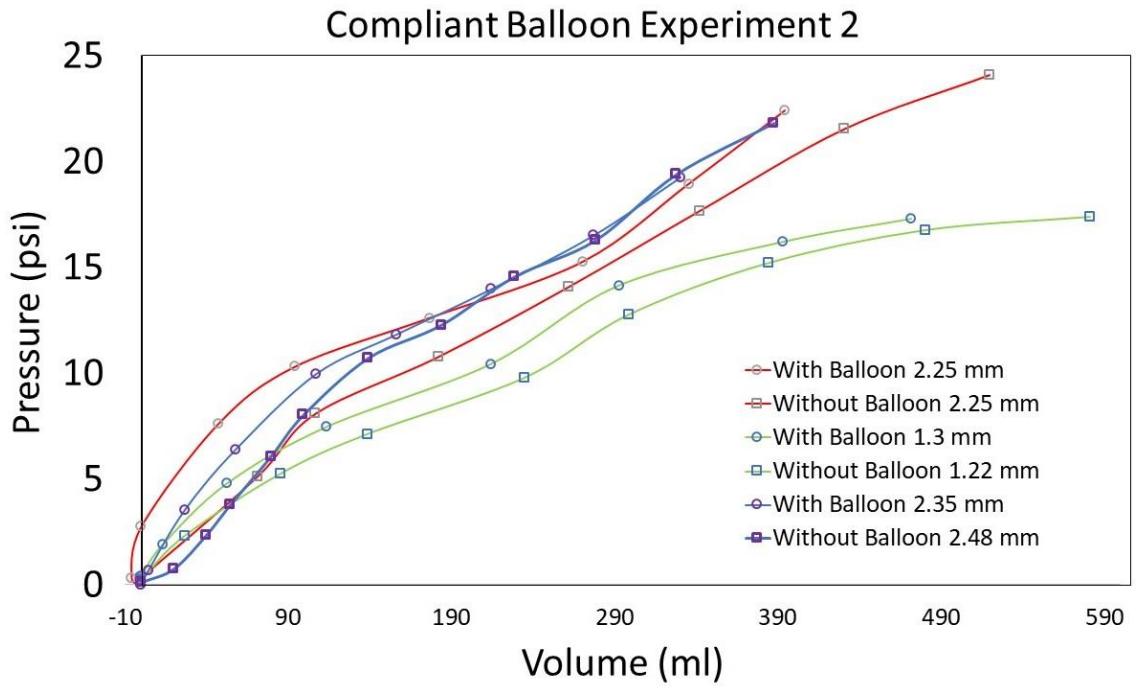

Figure 30: Paired silicone sample tests with and without compliant balloon.

The second experiment that was developed used the manual BIT with and without the compliant balloon. A modified lower clamp piece was designed to ensure water tight operation of the BIT during pressurization. Sheets of silicone

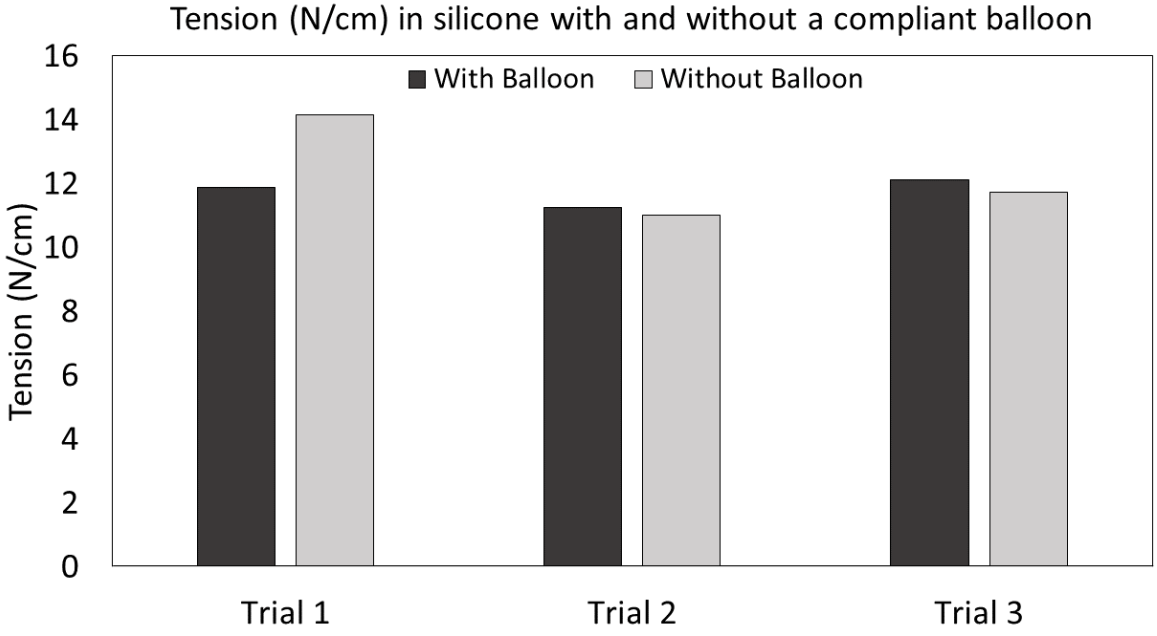

Figure 31: Tension in silicone with and without the compliant balloon.

were molded onto a flat glass plate. Six specimens were cut in pairs that were adjacent to one another. Three silicone samples were pressurized using the modified lower clamp piece and three samples were pressurized using the lower chamber with the compliant balloon.

Figure 30 displays both pressure-volume curves in direct comparison with and without the compliant balloon. The thicknesses of the silicone specimens were also recorded as they varied in thickness. Figure 31 reports the stress resultant or tension (N/cm) at a similar pressure for each paired trial and Figure 32 reports the stress (N/cm^2). The paired tension comparison had an average difference of 0.538 ± 0.611 (N/cm) and the stress comparison was reported to have a percent difference of 3.12 ± 2.77 (N/cm^2).

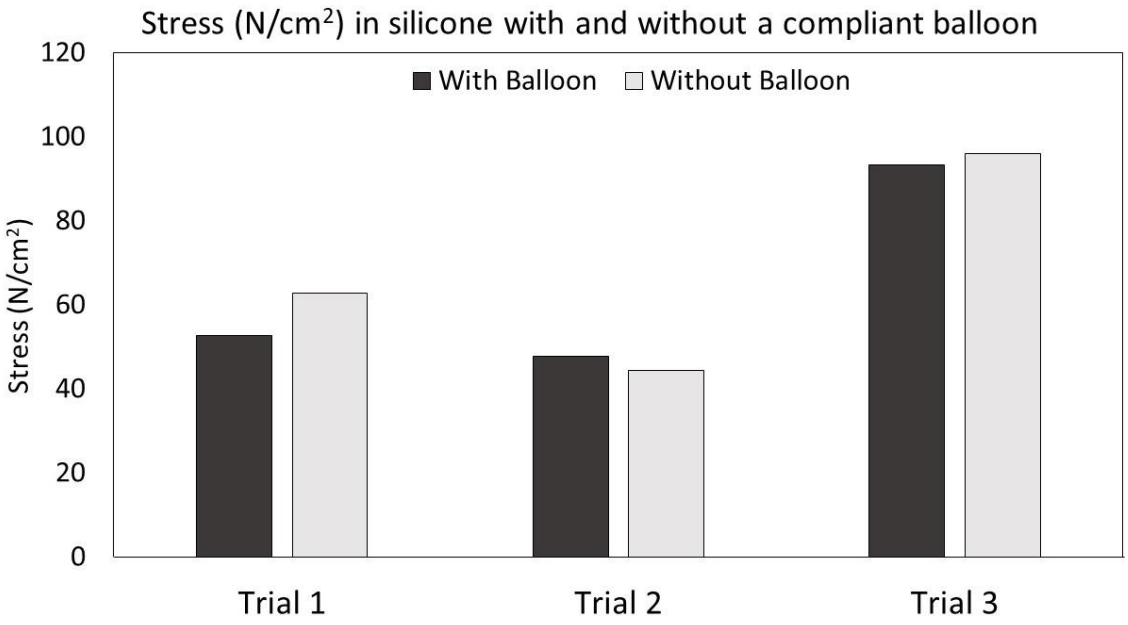

Figure 32: Stress in silicone with and without the compliant balloon.

Although the sample size was low in both experiments, it was concluded that using the compliant balloon would not significantly attenuate the stress during experimentation with the BIT. However, it remains unclear if the complaint balloon has the ability to space fill into smaller inclusions, peripheral arteries or defects that may be present in biological soft tissues. In a manual BIT experiment with the compliant balloon and a bovine aortic sample, a peripheral artery was placed in the specimen orifice area (Figure 33).

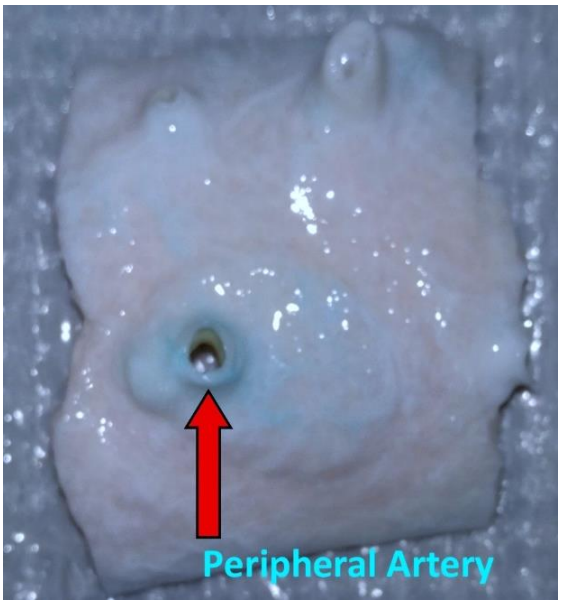

Figure 33: Peripheral artery BIT experiment with compliant balloon.

At 18.53 psi, the compliant balloon penetrated the peripheral artery and immediately reduced in pressure to 0.07 psi. This may be indicative of the compliant balloons' inability to conform to the specimen shape. Albeit, testing a sample with a peripheral artery would not be effective without a compliant balloon due to the simple fact that the pressurization media would flow through the peripheral artery. A compliant balloon was used both the manual BIT and automatic BIT (see Chapter 3) for experimentation as it was an acceptable compromise to the ease of use of the BIT apparatus.

2. 4 DEVELOPMENT OF THE MANUAL BIT APPARATUS

2.4.1 - Manual BIT Introduction

The manual BIT is a biological soft tissue apparatus that has the ability to test specimens of pressures up to 100 psi. Overall, the design of the manual BIT is meant to test a large number of adjacent samples in a biological soft tissue sheet or any other material. Testing a large number of samples to investigate whether localized material weaknesses exist is a desirable advantage of the manual BIT apparatus. Ease of use and the durability of the manual BIT lend itself well to seek out localized weaknesses and additional design changes were needed to make this plausible.

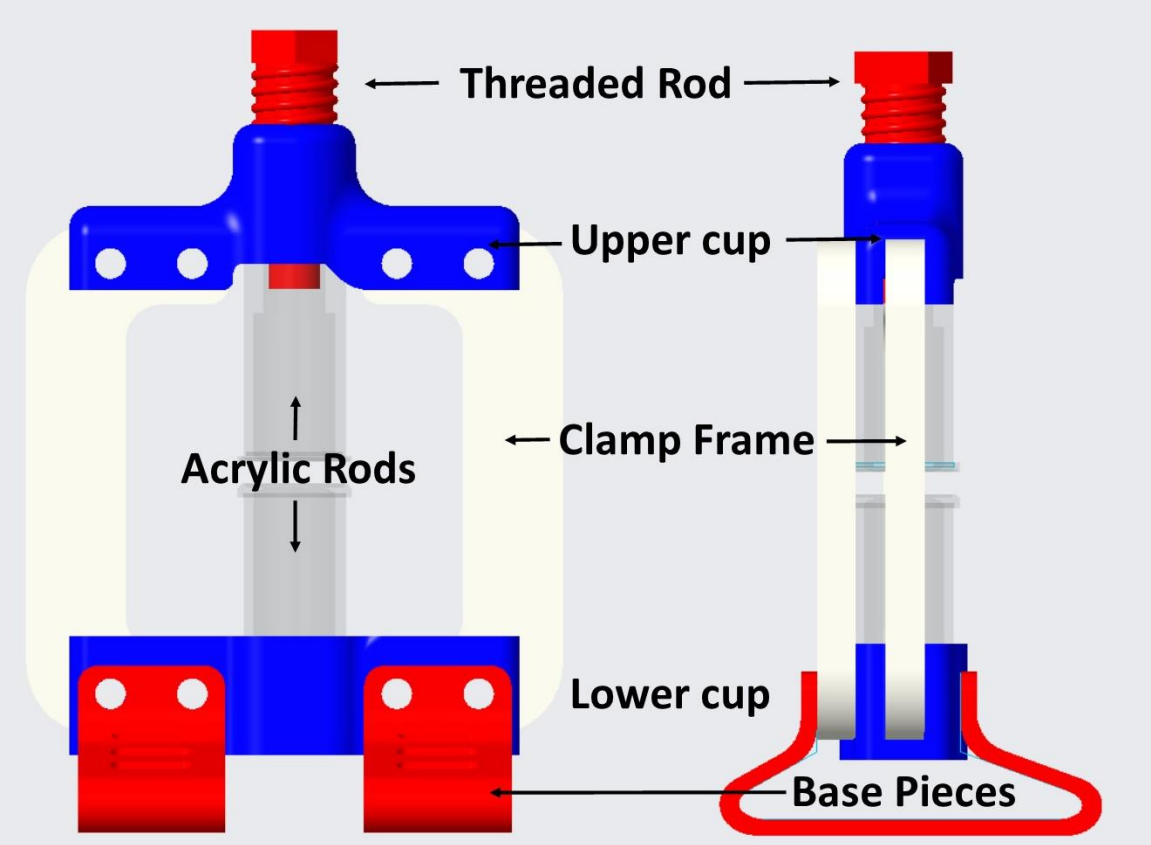

Figure 34: Double sided clamp frame with stage pieces.

Sections 2.3 addressed the changes that were made to both BIT apparatus'. The development of the manual BIT included the re-design of each of the three modules from the earlier manual BIT design performed in Brazil (see section 2.2). Modifications to the clamp frame and pressurization modules were made to improve the operation of the manual BIT.

2.4.2 - Manual BIT clamp frame modification

The clamp module that was implemented in Brazil featured a single sided clamp frame. The clamp frame began to deform and bend during BIT pressurization which is undesirable for operation (See Figure 22 in section 2.2). It is critical that the clamp frame does not bend to maintain clamping pressure on the specimen against the stage pieces. To ensure center alignment, a two-sided clamp frame was designed. Figure 34 represents the double-sided clamp module with modified lower and upper cup. The legs of the clamp frame were shortened to reduce bending and having the two-sided clamp frame ensured center alignment. Additional base pieces were designed to allow for clearance of the lower pressurization tubing.

Implementing these design changes allowed for center aligned clamping, reduced bending, and prevented specimen slipping. There were no critical failures of the clamping module that occurred during the loading and unloading of multiple specimen types (n > 100).

2.4.3 - Manual BIT pressurization module

Incremental pressurization is desirable when pressurizing specimens during a BIT experiment. Others have attached a pump to a uniaxial load cell use a compressed air source[33,35]. The ability to have a portable manual BIT apparatus was a beneficial design feature. A screw-type syringe was sought after with a volume larger than 10 mL, but there were none that could achieve a large amount of pressure due to the use of glass. A 30-mL plunger-type syringe was modified with 3D-printed components and fasteners found at a local hardware store. Figure 34 represents the syringe assembly and its components and Figure 35 is the assembled syringe. The syringe was modified by converting the push mechanism into a screw-type syringe.

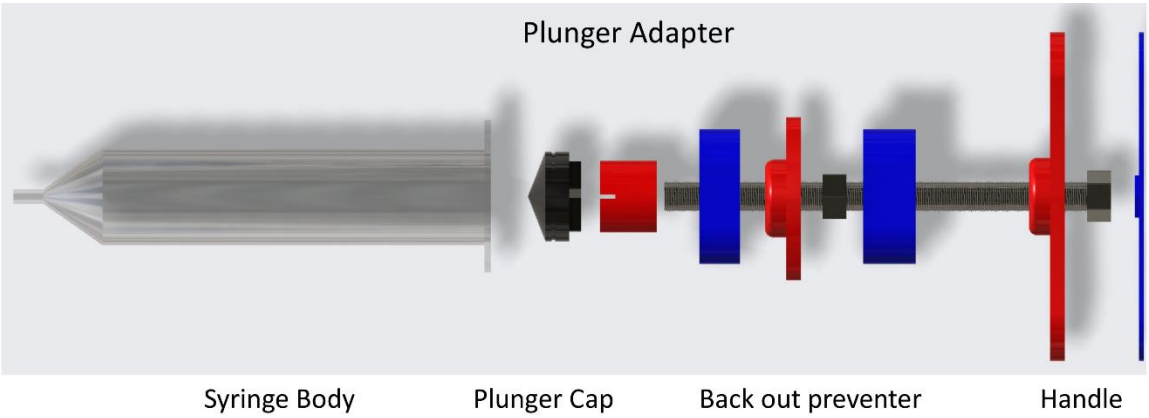

Figure 35: Expanded view of the modified plunger assembly with 3D printed parts for manual screw-type operation.

Additional pieces were design using computer aided design to ensure that the handle did not back out during pressurization. The plunger adapter piece featured an embedded nut during 3D printing (printing was paused to place the threaded hex nut inside of the model). Epoxy was used to attach the plunger

capwith the plunger adapter affix the threaded rod in the embedded nut to ensure that the plunger would be able to return to its original position.

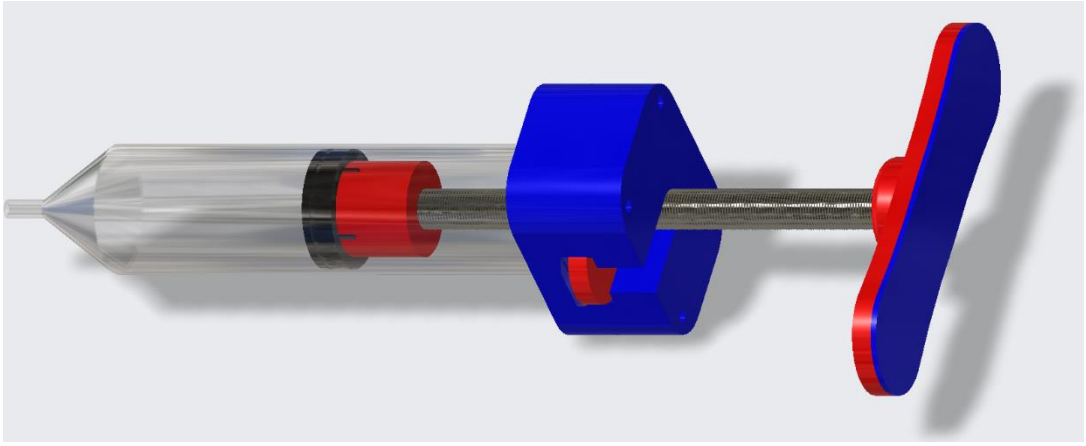

Figure 37:Assembled view of the modified screw-type syringe for manual pressurization.

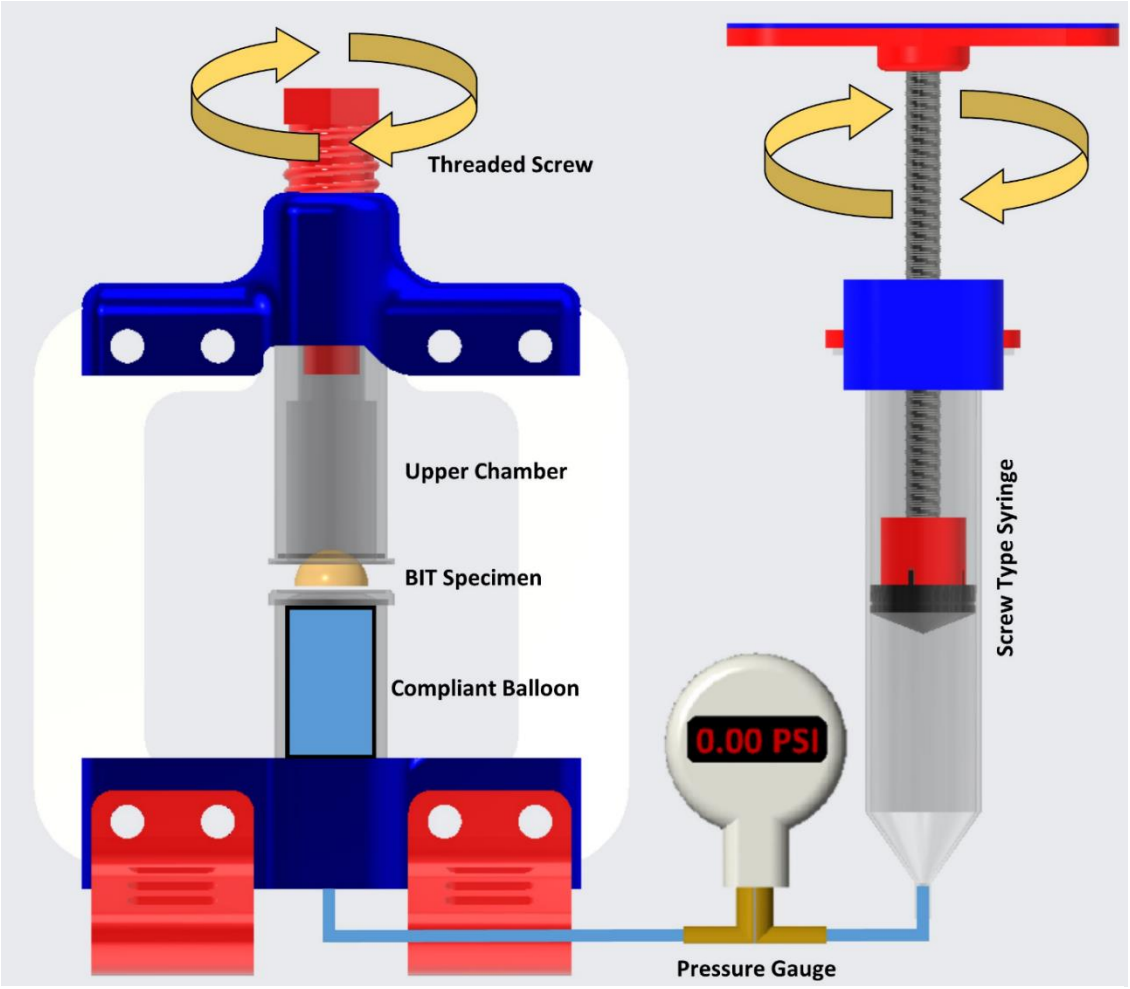

Figure 37: Manual BIT apparatus with the three modules.

Additional tubing, pipe fittings, hose clamps and a digital pressure gauge were assembled along with the compliant balloon. The SSI Technologies, Inc., digital pressure gauge (max 100 psi with 0.1% error) was mounted onto a base. Figure 37 is representative of the manual BIT assembly.

2.4.4 - Manual BIT data acquisition

To record volume displacement, the upper acrylic chamber is filled with blue water (food coloring) and the measurements are made digitally in MATLAB. During pressurization, the water column inside the upper acrylic piece moves upward. The upper chamber has an inner column that has a fixed diameter of 15.9 mm (measured with a digital caliper) while the outer diameter of the upper chamber is 31.9 mm. The outer diameter is used as a reference for scaling digital pixels to real world dimensions in millimeters. Due to the variability in the distance from the camera apparatus, scaling is necessary for every BIT experiment performed.

Each manual BIT experiment is loaded and the scaling data, frame number, pressure (psi) and height of the water column are recorded with static images by manually entering video frames using the MATLAB user interface (using the '*implay' command*). A separate script is used to calculate the volume change of the water column and pressure (Figure 38). In the case of rupture, the frame right before rupture occurs is taken to record the final volume and pressure data.

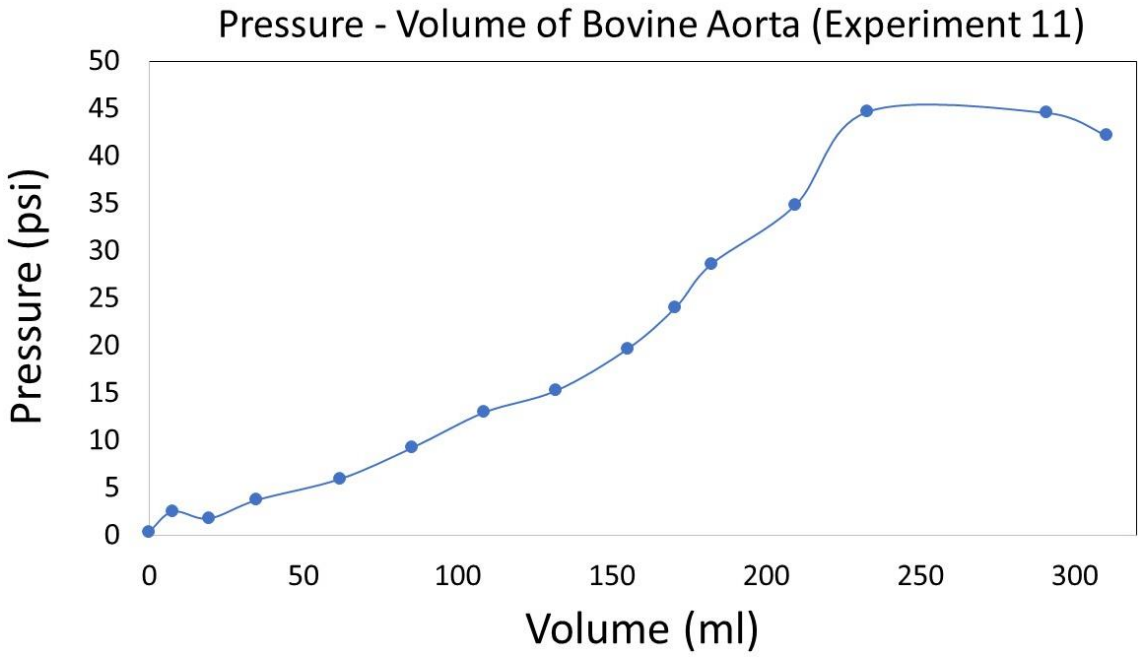

Figure 38: Pressure Volume relationship in bovine aorta.

Due to the simplicity of acquiring the data, stress calculations are performed with two-dimensional shape information. Hoop stress for a hemisphere is used to calculate the stress (N/cm^2) and tension (N/cm) for the respective peak values (Equations 6a and 6b) which simply rely on knowing the pressure, radius and thickness of the material. Therefore, the following stress calculations can also be applied to the automatic BIT with the same assumptions.

Equation 6(a) Hoop stress (b) and tension

$$Hoop\ Stress\ for\ Hemisphere = \frac{pr}{2t}$$

$$Hoop\ Tension\ for\ a\ Hemisphere = \frac{pr}{2}$$

$$p = pressure, r = radius, t = thickness$$

Images are captured from each experiments' video at the peak pressure to calculate the peak stress/tension for each experiment. The assumptions of the material being homogeneous and isotropic are made to accommodate these calculations. A MATLAB script was created to load each image and record the circle chord length and Sagitta of the BIT under pressure. Figure 39 represents the computer aided guide to ensure that the correct height is chosen after the chord length points are picked.

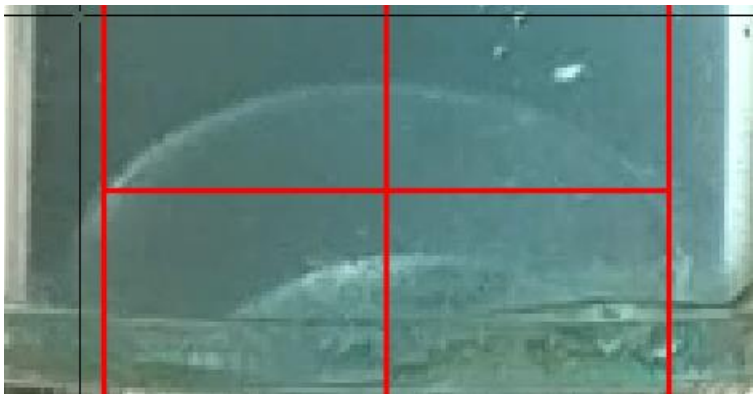

Figure 39: Extracting width and height information from a silicone sample.

Figure 40, 41 and derivation 1 is representative of the radius calculation with the data acquired from the script. The yellow region would be indicative of a specimen being pressurized in the BIT while the height represents the Sagitta (perpendicular from the center of the arc to the center of its base).

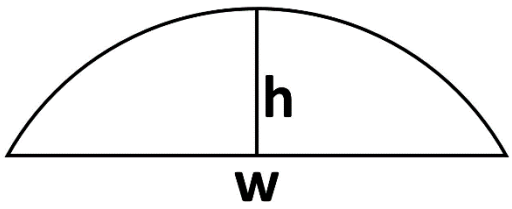

Figure 40: Width and height of a circle section.

$$h = height, w = width$$

Derivation 1: Finding radius with intersecting cord theorem.

$$Intersecting\ chord\ theorem:$$

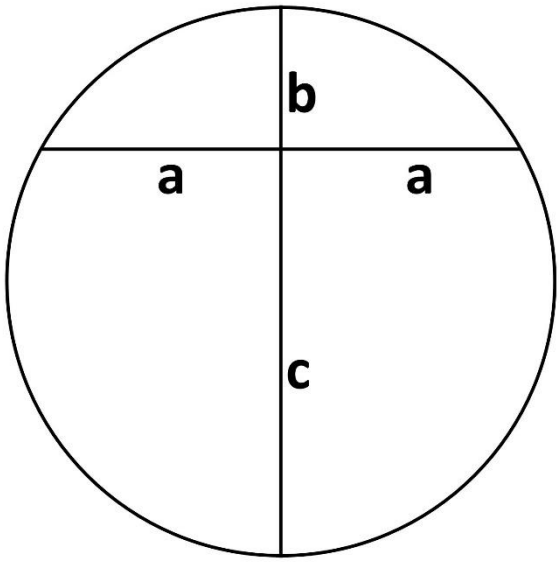

$$a \cdot a = b \cdot c$$

$$a = \frac{w}{2}, therefore$$

$$\frac{w^2}{4} = h \cdot c;\ \ c = \frac{w^2}{4h}$$

$$Diameter = h + c$$

$$Diameter = h + \frac{w^2}{4h}$$

$$Radius = \frac{h}{2} + \frac{w^2}{8h}$$

Figure 41: Circle with intersecting lines.

Equation 7(a) Modified Hoop stress equation for stress (b) and tension.

$$Hoop\ stress = \frac{p}{2t}\left(\frac{h}{2} + \frac{w^2}{8h}\right)$$

$$Hoop\ tension = \frac{p}{2}\left(\frac{h}{2} + \frac{w^2}{8h}\right)$$

Equations 7a and 7b feature the final derivation of stress and tension calculations that allow for simple measurements of the width and Sagitta height of a domed sample. Utilizing the intersecting cord theorem, any width taken above the equator of a given BIT sample will net the equivalent radius and in turn, the stress and tension. The results of the peak stress calculations are found in Chapter 3.

2.5- MANUAL BIT DISCCUSION AND CONCLUSION

A manually operated bubble inflation test apparatus was constructed with the aid of 3D printing, a digital pressure gauge, low-cost fittings and hardware. The finalized design addressed the concerns that were raised in the preliminary studies while operating the BIT (sections 2.2 and 2.3). The manual BIT allows for multiple experiments to be performed adjacent to one another without the need of cutting specimen as it is not understood how cutting specimens out of the material affects its material properties. However, due to the simplicity of the data collected, the manual BIT is unable to interpret any material heterogeneity or anisotropy that may exist. Hoop stress and tension are calculated by taking the radius and pressure of the BIT specimen right before rupture graphically and it is unclear how reliable this calculation is. Albeit, groups have used a similar method to estimate stress in BIT experiments (Milankovic et al) in the past with human thoracic aorta. The operation of the manual BIT allowed for quick loading and unloading specimens, and the use of the compliant balloon ensured no leakage occurred during pressurization. It was demonstrated that the manual BIT can achieve large pressures (100 psi) and can maintain this load on the 3D printed parts. As the manual BIT was implemented in ($n > 100$) experiments, there was no sign of warpage or damage to the 3D printed clamp frame module and this continued during the experimentation with biological soft tissues. Future studies with the manual BIT may give insight to whether material weaknesses exist in wholly harvest AAA tissue or any other biological soft tissue.

2.6 - AUTOMATIC BIT INTRODUCTION

The automatic BIT is a multiaxial testing apparatus that can collect a richer set of data than the manual BIT. The main advantage of the automatic BIT is that the data acquisition is automated and the capability of reconstruction of surface geometry in biological soft tissues during pressurization. The maximum pressure that can be applied to the automatic BIT is ~44 psi due to physical limits of the linear actuator that is used in the apparatus. Due to the nature of collecting the images during experimentation, the specimens must be cut prior to pressurization, disabling the ability to test adjacent samples in a more rigorous manner. The automatic BIT contains the same three modules (section 2.1) that are necessary to pressurize samples and collect data.

2.7 - AUTOMATIC BIT CLAMP MODULE

The automatic BIT requires that the sample is 'top loaded' in order to capture the shape of the specimen during pressurization. This clamp module features a similar clamping and gripping mechanism as the manual BIT with laser cut stage pieces that ensure no slipping occurs during pressurization. All of the components except for the laser cut acrylic pieces were 3D –

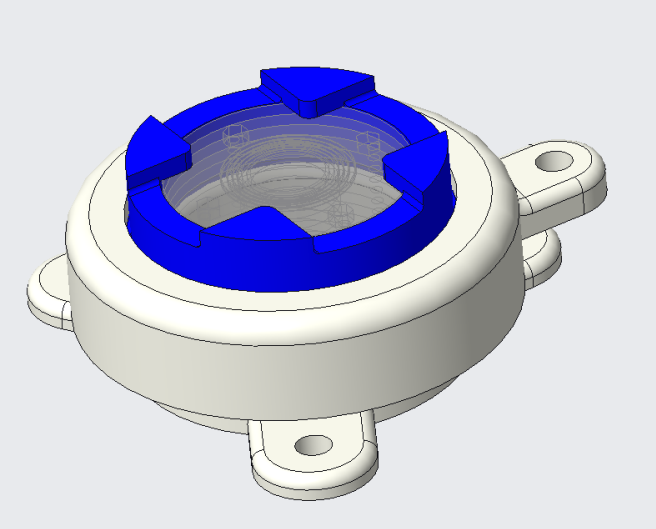

Figure 42: Assembled top loaded clamp frame to view sample from two orthogonal views.

printed using PLA. Figure 42 is the assembled clamp module and Figure 43 includes individual components that make up the clamp module. The top clamp piece applies pressure to the intermediate clamping ring to clamp a specimen with the base while the clamping ring prevents the specimen from rotating. The acrylic core is composed of laser cut acrylic pieces that are fastened together while the stage pieces are not fixed. This allows specimens to be loaded onto the stage pieces before clamping. The base of the clamp module is attached to a laser cut base that houses two cameras for optical strain measurement. Subsequent experiments using the 3D printed automatic BIT clamp module did not suffer from catastrophic failure or undergo specimen slipping of various types (n > 50) during pressurization.

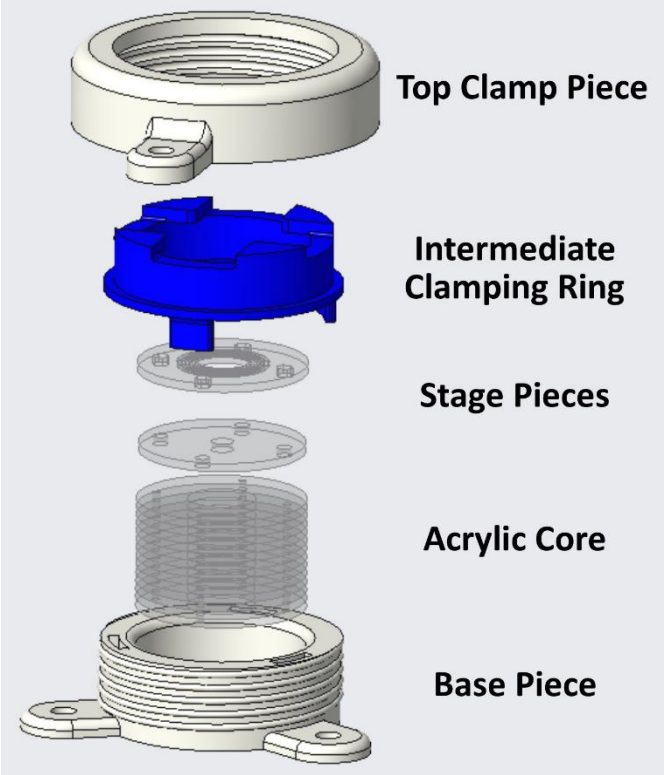

Figure 43: Expanded assembly view of components of the top loaded clamp frame.

2.8 – AUTOMATIC BIT PRESSURIZATION MODULE OVERVIEW

Pressurization of the automatic BIT relied on the use of a microcontroller (Arduino Uno), pressure transducer, analog pressure gauge and a linear actuator. Water (H_2O) was used as the pressurization media with the use of the

compliant balloon (section 2.3.3). A 30-ml syringe coupled with the linear actuator provided pressurization to the specimens during experimentation while the pressure transducer provided real time pressure data to the microcontroller with an external pressure gauge providing quick visual reference of pressure information. Figure 45 is the overall design of the pressurization module that includes various components that are used to attach the linear actuator with the

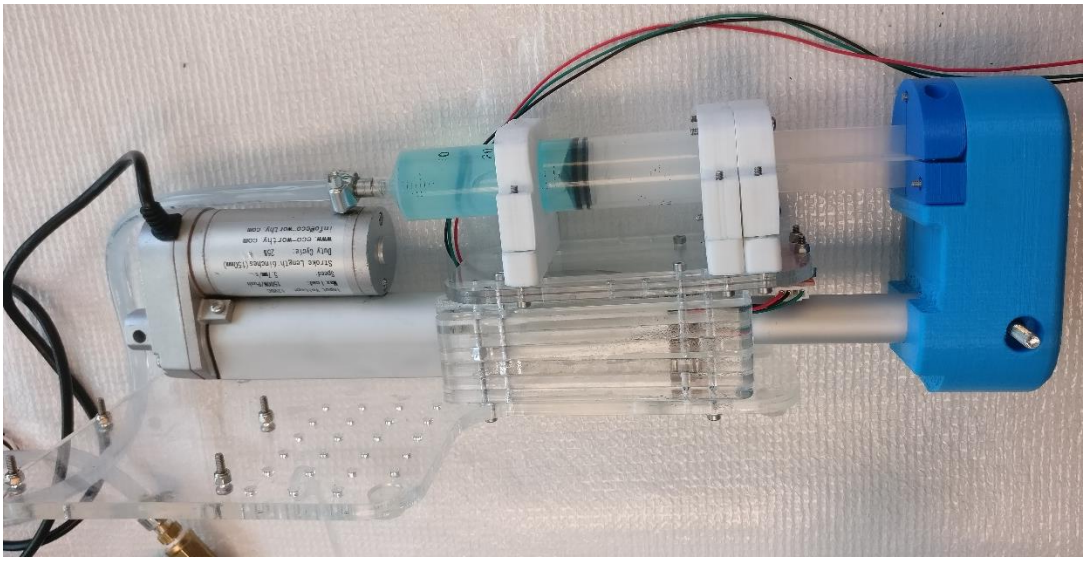

Figure 44: Syringe attached to linear actuator with laser cut and 3D printed parts.

30 ml syringe.

A screw-type syringe was not suitable in this instance as proportional integral derivative (PID) control schema was used to drive the linear actuator based on the pressure transducer values. Sections 2.8.1 – 2.8.4 discuss each of the hardware and software components that were implemented to create a cohesive pressurization module for the automatic BIT.

2.8.1 – Pressure Transducer Calibration

A pressure transducer with a range of 0 to 100 psi was used to send in a voltage reading to the Arduino microcontroller which in turn converted it to an analog value. It was necessary to calibrate these analog values to actual pressure values. The pressure transducer was attached directly to the manual BIT syringe module and SSI Technologies, Inc. pressure gauge (range of 0 to 100 psi with 0.1% error) and pressurized to 55.0 psi. An analog to digital convertor (Arduino microcontroller) interprets voltage from 0 to 5V into analog values from 0 to 1024. The pressure transducer has a working voltage range between 0 and 5 volts (V) and their corresponding analog sensor values range between 0 and 1023. Figure 45 represents the calibration data with a conversion

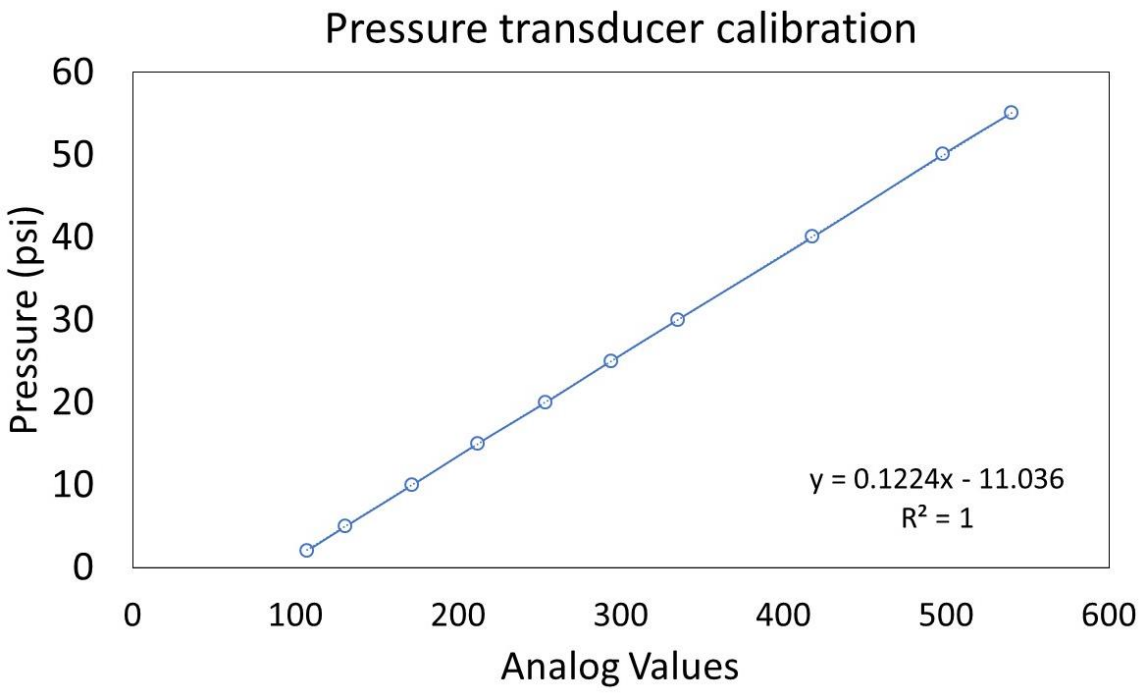

Figure 45: Pressure transducer calibration with analog values and pressure measurements.

equation from the trendline ($R^2 = 1$) that exhibited a linear relationship. Using the

conversion equation (equation 8), the pressure will be converted from analog values to pressure in psi.

Equation 8: Pressure (psi) relationship to pressure transducer analog values

$$Pressure\ (psi) = 0.1224 * analog\ value - 11.036$$

Converting pressure values occurs in MATLAB rather than the Arduino microcontroller to reduce the number of calculations performed on the ATMEL328 microchip.

2.8 2 – Automatic BIT basic pressure control system

A basic control system was implemented to interpret pressure transducer values and drive the linear actuator forward and backward. Using relatively low cost components, a simple proportional integral derivative (PID) controller was implemented with the Arduino microcontroller with an external PID library[71]. Equation 9 is the general form of the proportional, integral and derivative components that are implemented in this control system.

Equation 9: PID Output equation

$$Output = K_p e(t) + K_I \int e(t)dt + K_D \frac{d}{dt} e(t)$$

$$e = Setpoint - Input$$

In the system that is used for pressurizing specimens, the setpoint is the assigned pressure given by an analog value. A stepwise loading scheme was chosen for the pressurization of each specimen where the setpoint is iterated for 250 cycles until the next setpoint is selected. The initial setpoint that was chosen

was an analog value of 100 (1.2 psi) and incremented by an analog value of 25 every 100 iterations for each setpoint.

Initially, a two-relay system was used to change the polarity of the linear actuator. However, the relays had a two second minimum switch time and was not effective in implementing a PID controller. A linear actuator with a maximum load (push configuration) of 330 lbs. was used to generate forward and backward motion of the syringe. An Arduino Uno and a motor shield featuring a L293D Dual H-bridge driver was used to control the linear actuator. The L293D H-bridge has the capability of quickly changing the polarity of the linear actuator, ideal for generating rapid forward and backward movements. As the PID controller operated with a given setpoint the linear actuator would move the syringe plunger forward or backward depending on the output of the PID. After each iteration of the PID, the microcontroller would serial print the following variables: time of testing in milliseconds (ms), raw pressure transducer values, ± output from the PID and the iteration number.

Manual tuning of the system was performed using initial gain parameters (proportional, integral and derivative terms), linear actuator on/off time, and a setpoint. Figure 46 represents the analog pressure values for a setpoint analog value of 250 (19.6 psi). Initial proportional, integral and derivative gain values were chosen as 0.8, 0.07, and 0.12 base on a control system that was implemented in Arduino[72]. These initial gain parameters were perturbed along with the on/off time of the linear actuator. To test these parameters, a silicone sample with a thickness of 2.6 mm was loaded into the automatic BIT. The

sample had a target setpoint pressure of 19.6 psi (analog value of 250) and the PID would operate in accordance with the setpoint that was applied to the system. Various tuning parameters were chosen to determine which combination of parameters minimized error to the setpoint. Table 5 displays the perturbations of the initial gain values, linear actuator on/off time, PID output limits, and the mean error and standard deviation for a setpoint given at an analog value of 250.

Table 5: Tuning parameters used for the PID control system.

	Kp	Ki	Kd	Output +/-	On/off time	Mean Setpoint Difference	STD Setpoint Difference
Case 1	0.8	0.07	0.12	5	5	5.23	5.22
Case 2	0.8	0.07	0.12	10	10	3.17	4.53
Case 3	0.8	0.07	0.12	25	5	3.89	4.43
Case 4	1.6	0.14	0.24	5	5	1.39	3.66
Case 5	1.6	0.14	0.24	10	10	4.09	3.50
Case 6	3.2	0.28	0.48	5	1	1.43	4.00
Case 7	3.2	0.28	0.48	5	5	-1.45	2.94
Case 8	3.2	0.28	0.48	10	10	-3.51	4.80
Case 9	3.2	0.28	0.48	15	15	3.35	2.90
Case 10	3.2	0.28	0.48	20	20	-1.64	4.27

Additionally, Figures 47 and 48 represent sets of the same initial gain parameters (doubled and quadrupled from initial values). plotted against one

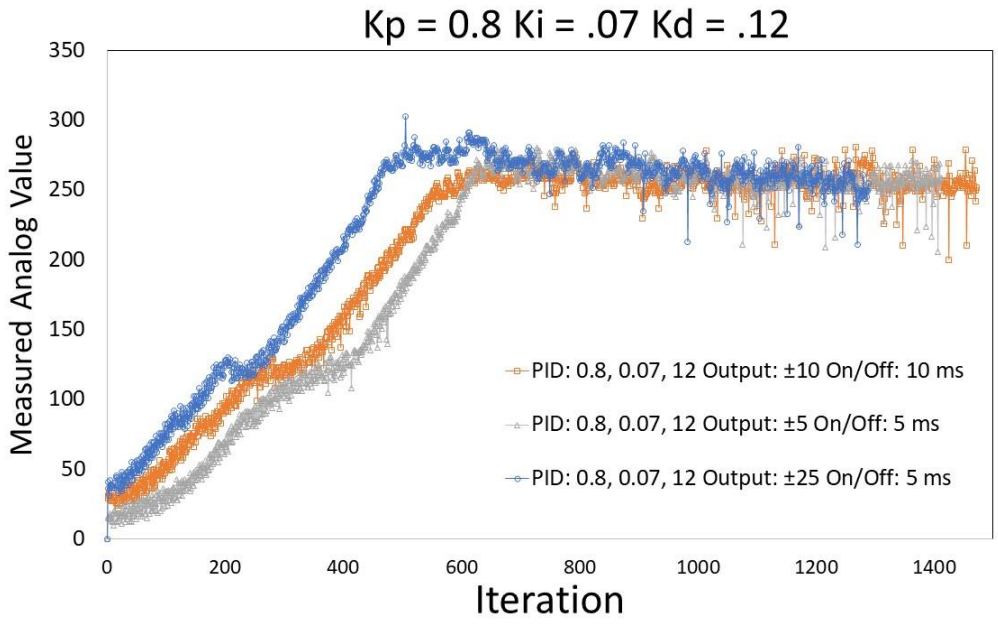

Figure 47: PID gains 0.8, 0.07, 0.12 with various output and on/off times

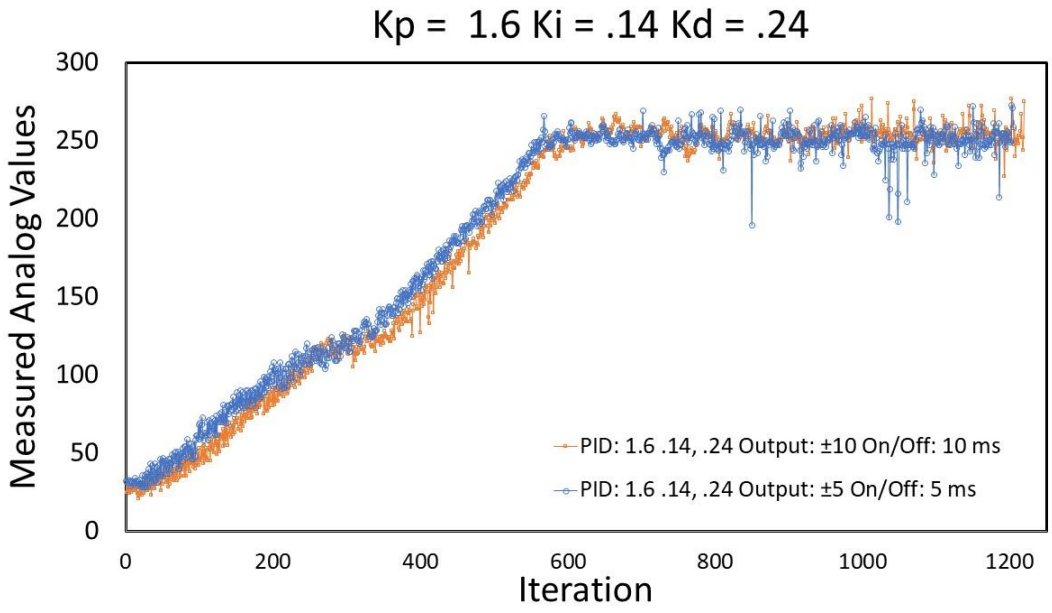

Figure 47: PID gains 1.6, 0.14, 0.24 with various output and on/off times

another and a plot (Figure 49) of the lowest error gain parameters compared to one another (cases 2,4 and 7).

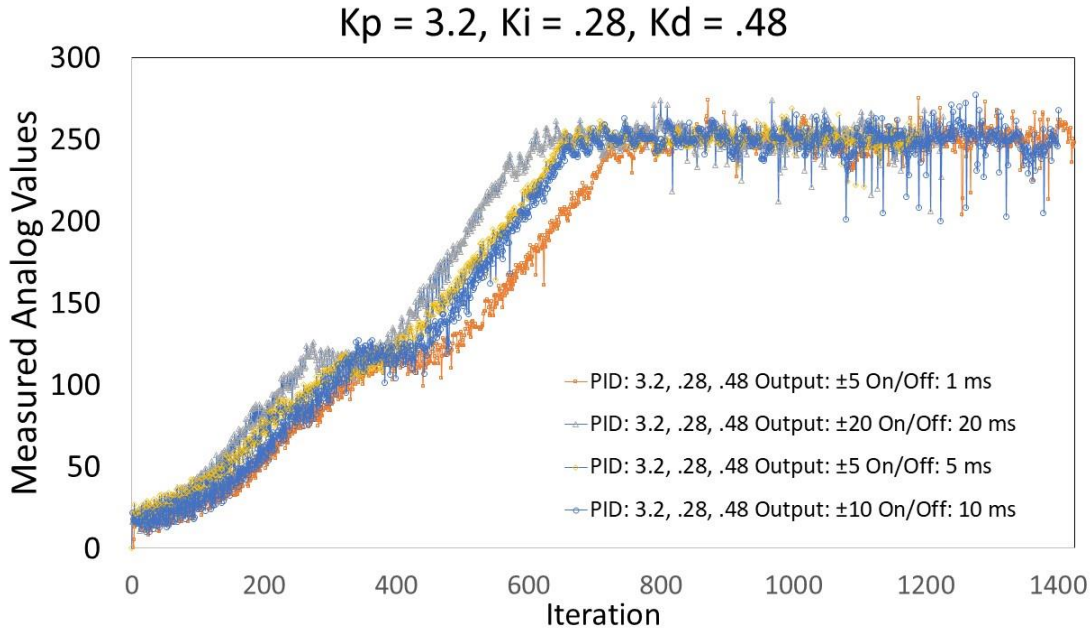

Figure 49: PID gains 3.2, 0.28, 0.48 with various output and on/off times.

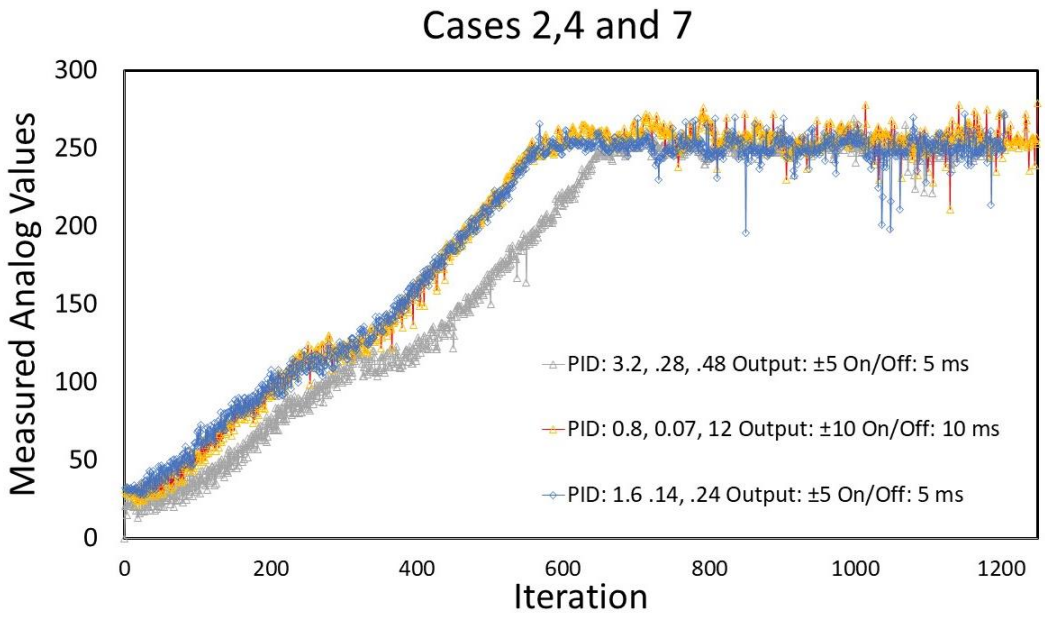

Figure 49: Cases 2,4, 7 lowest error with given PID gains.

Inherit nonlinear behavior of the test specimen along with the viscoelastic behavior of the tubing may have also reduced the efficacy of the PID controller. The system did not experience any performance gains by reducing the on and off time of the linear actuator, and case 4 (from Table 5) was determined to minimize error in the system. It was also noted that increasing the baseline parameters by a factor of four had a net effect of underestimation compared with the setpoint. These parameters were subsequently used for the automated BIT experiments.

2.8.3 – Stepwise Loading with the Automatic BIT

A stepwise pressurization load to the test specimen was implemented by changing the setpoint incrementally (Figure 50). The range of setpoints were from an analog value of 100 (1.2 psi) to 450 (44 psi) incremented by an analog value of 25 (3.06 psi) for 250 iterations per setpoint until the system reached an

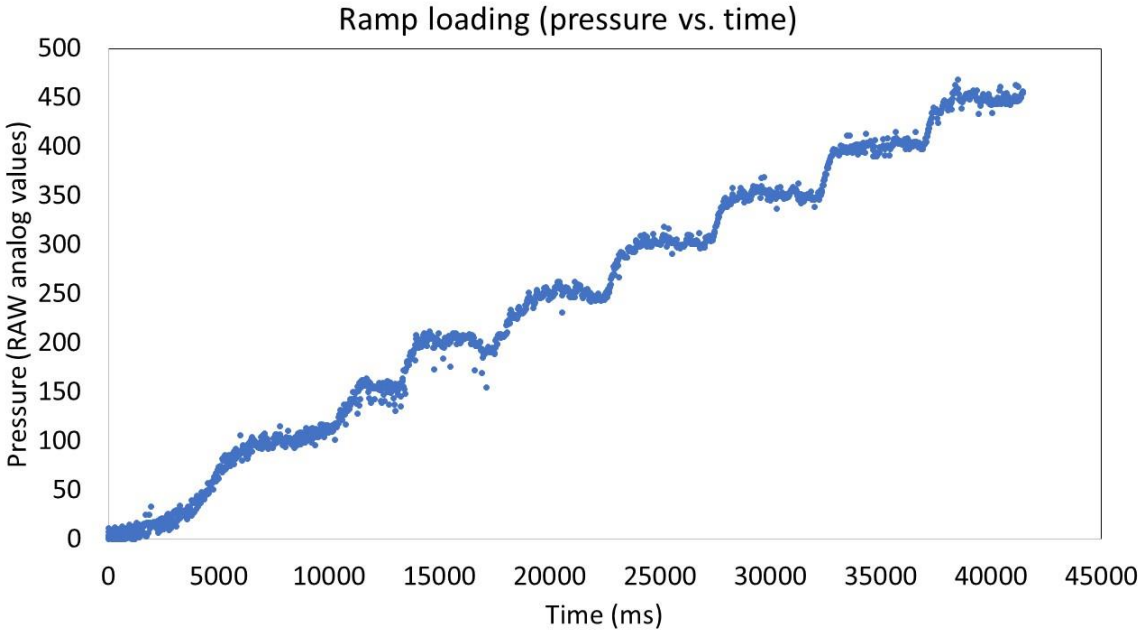

Figure 50: Stepwise pressurization of a Bovine Aorta Sample

analog value of 450 (44 psi). The initial gain values were chosen based on the

findings from section 3.3.2. When the number of iterations reached half of the total amount of iterations (125 of 250), a trigger variable was sent to take a snapshot of the deformation of the specimen.

2.8.4 – Automatic BIT volume measurement verification

Initially, a Microsoft Kinect camera (V2) was attempted as a means to capture the three-dimensional shape of the specimen during pressurization. However, it was quickly realized that the reconstruction of the test specimen with a small diameter (0.675" or 17 mm) was difficult to resolve in the z-depth direction. An alternative method proposed by Raghavan et al of reconstructing three-dimensional brain aneurysm based on two-dimensional orthogonal planar images[73]. A curve evolution algorithm that was developed by Sederberg and

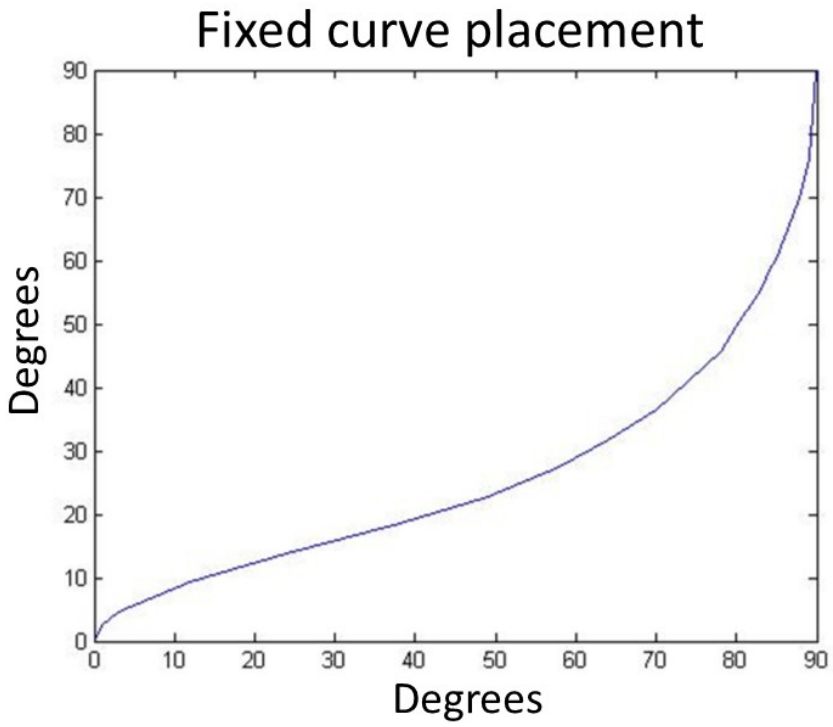

Figure 51: Fixed curve placement based on an angle table

Greenwood generated smooth intermediate curves between two 2-dimensional

shapes[73,74]. Piecewise curves of these shapes were used to generate intermediate curves using Bezier curves[74]. The application of the curve evolution was performed on two orthogonal images (xz-plane and yz-plane) taken of a pressurized automatic BIT test specimen and the subsequent intermediate curves were placed at intermediate angles to create a three-dimensional volume. Sharda et al placed the intermediate curves based on a fixed table (constant angle, θ), found in figure 52

The overall effect of having a fixed θ table created a 'pinching' effect at every quadrant when viewed from the positive z-axis of the xy-plane (top view). Figure 51 demonstrates this phenomenon in a reconstructed brain aneurysm. An alternative curve placing algorithm was derived based on intermediate curve radii rather than having a fixed θ. Derivation 2 from an ellipse formula created quadrant-based curve placement with function θ(r, a, b).

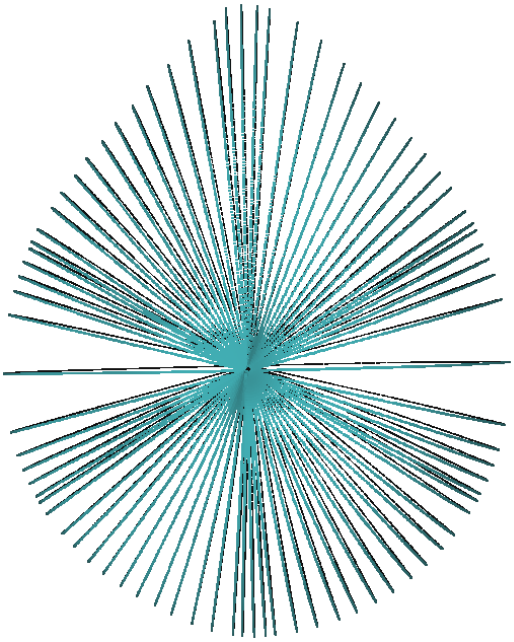

Figure 52: Pinching effect on a reconstructed brain aneurysm.

Figure 53a is a view of the xy-plane from positive z axis, that splits the major and minor axis of intersecting ellipses, while Figure 53b displays the first quadrant with a_1 being half the major axis and b_1 half the minor axis.

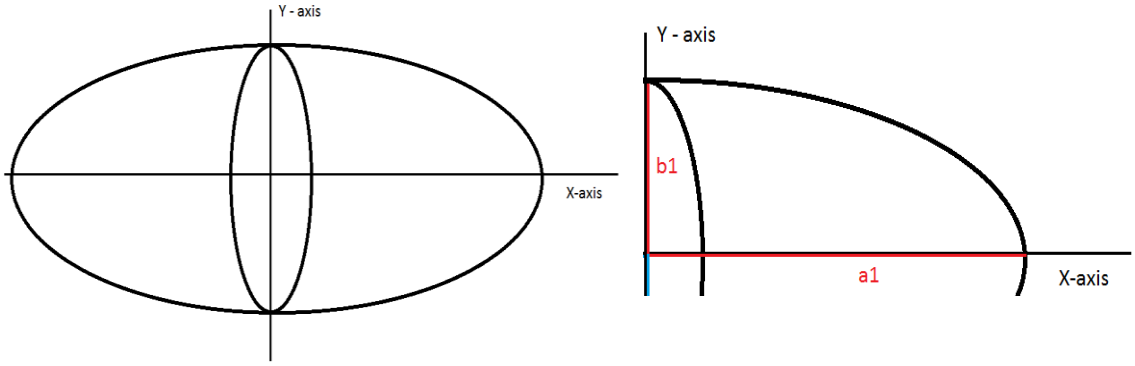

Figure 53 (a) xy view of an ellipse from the +z axis. (b) First quadrant with major and minor axes.

Derivation 2: R-Theta relationship derivation.

$$x = a1\cos(\theta)\,;\; y = b1\sin(\theta)\,;\; r = \sqrt{x^2 + y^2}$$

$$r = \sqrt{a_1^2\cos^2\theta + b_1^2\sin^2\theta}$$

Equation 10: Relationship of radius, major/minor axis and theta.

$$\theta(a_1, b_1, r) = \cos^{-1}\left(\frac{\sqrt{r^2 - b_1^2}}{\sqrt{a_1^2 - b_1^2}}\right)$$

The intermediate curves yield intermediate radii corresponding to a quadrant-specific major and minor axis. This information is passed into Equation 10 to calculate the appropriate angle in which the intermediate should be placed (bounded by quadrant ellipse). For the same reconstruction found in Figure 52, the ellipse formula is implemented in figure 54. Figure 55 is the corresponding r-theta curve that places the intermediate curves based on their respective ellipse quadrants.

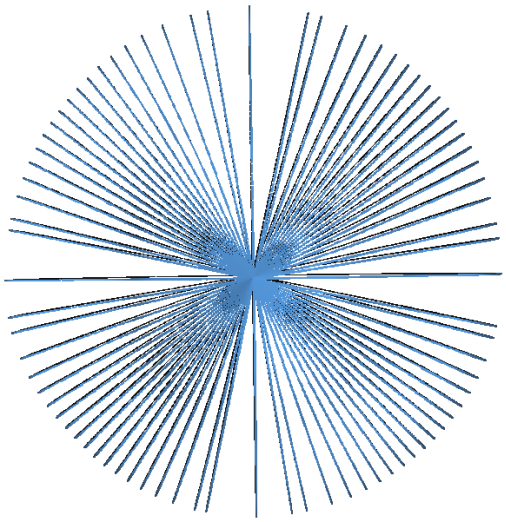

Figure 55: Improved curve placement based on r-theta formula.

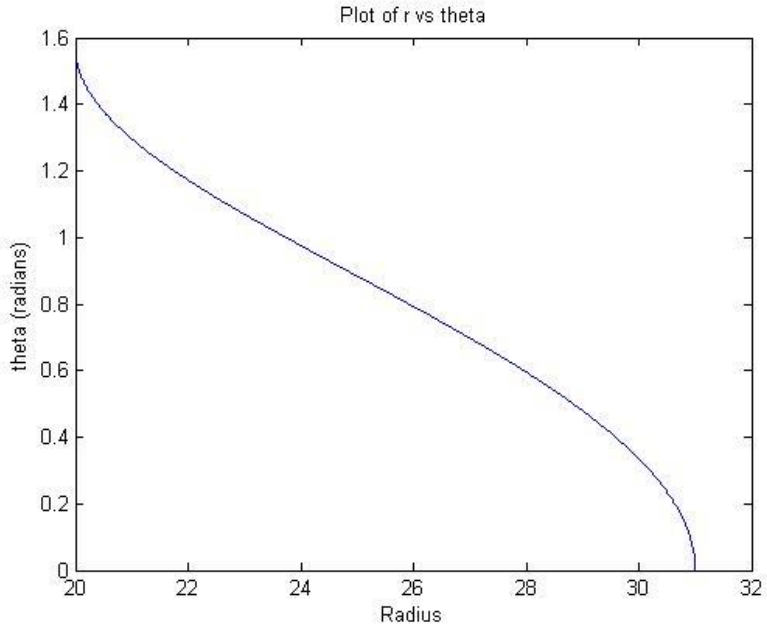

Figure 54: Corresponding r-theta curve that was used to place curves.

Albeit, the surface reconstruction was qualitatively improved, it was important to verify if this change was quantitatively appropriate. Further verification was carried out by reconstructing a three-dimensional hemisphere with two 2-dimensional semicircles (Figure 56a) and tested against Equation 11, the volume of a hemisphere. Figure 56b represents the hemisphere split into two proper quadrant placements in three-dimensions. Several parameters were perturbed to determine to optimize shape metrics and computational time. These parameters included the number of intermediate curves per quadrant, mesh size and the number of points per closed curve.

Equation 11: Volume of a hemisphere.

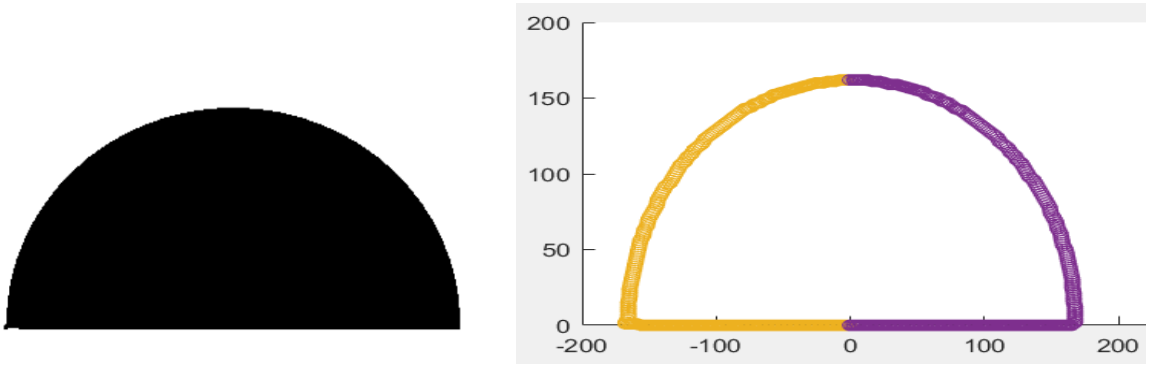

Figure 56 (a): Semicircle to be reconstructed (b) Creating a curve and dividing it.

$$Volume\ of\ Hemisphere = \frac{2}{3}\pi r^3$$

Figure 57 represents the three-dimensional reconstructed hemisphere with 20 intermediate curves per quadrant. Quadrants I,II, III and IV are colored yellow, green, red and blue, respectively.

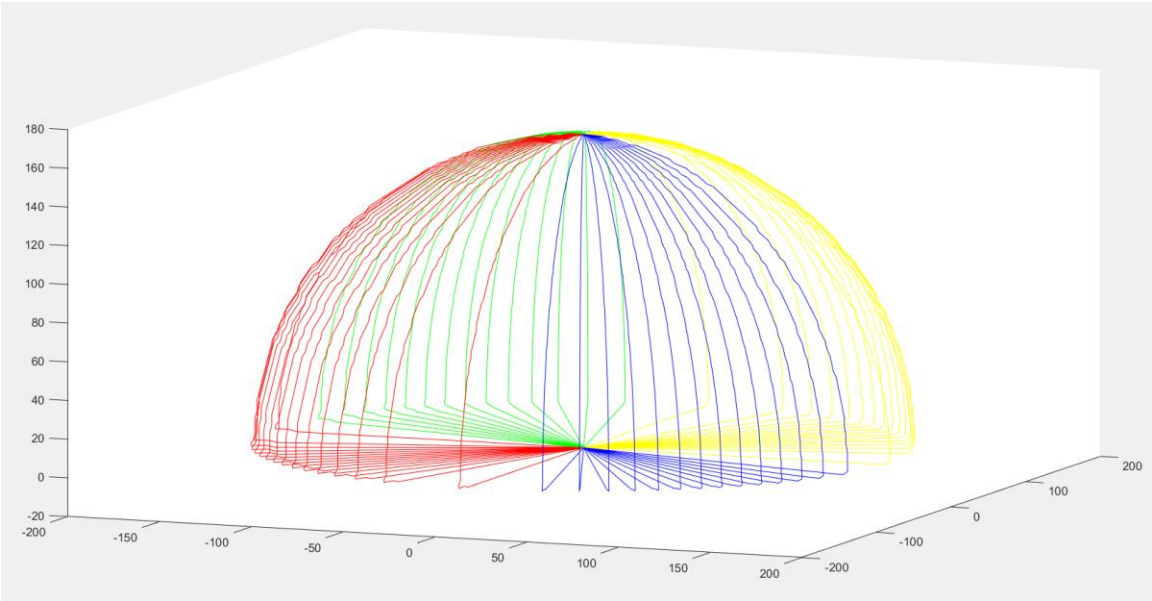

Figure 57: Three-Dimension reconstructed hemisphere with 20 curves per quadrant.

Figure 58 displays the hemispheres in a top view (viewed from positive z axis to xy-plane) and an orthogonal view of the reconstructed surface mesh (reconstructed with 20 curves).

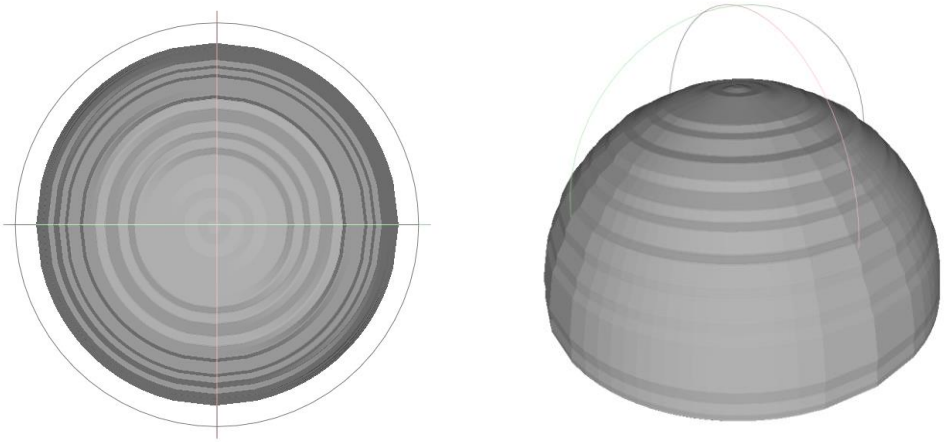

Figure 58: Surface rendered hemisphere.

Figure 59 is the total number of curves and computational time to reconstruct the entire volume. An inflection point occurs around 40 curves and the maximum number of curves that could be placed was 70.

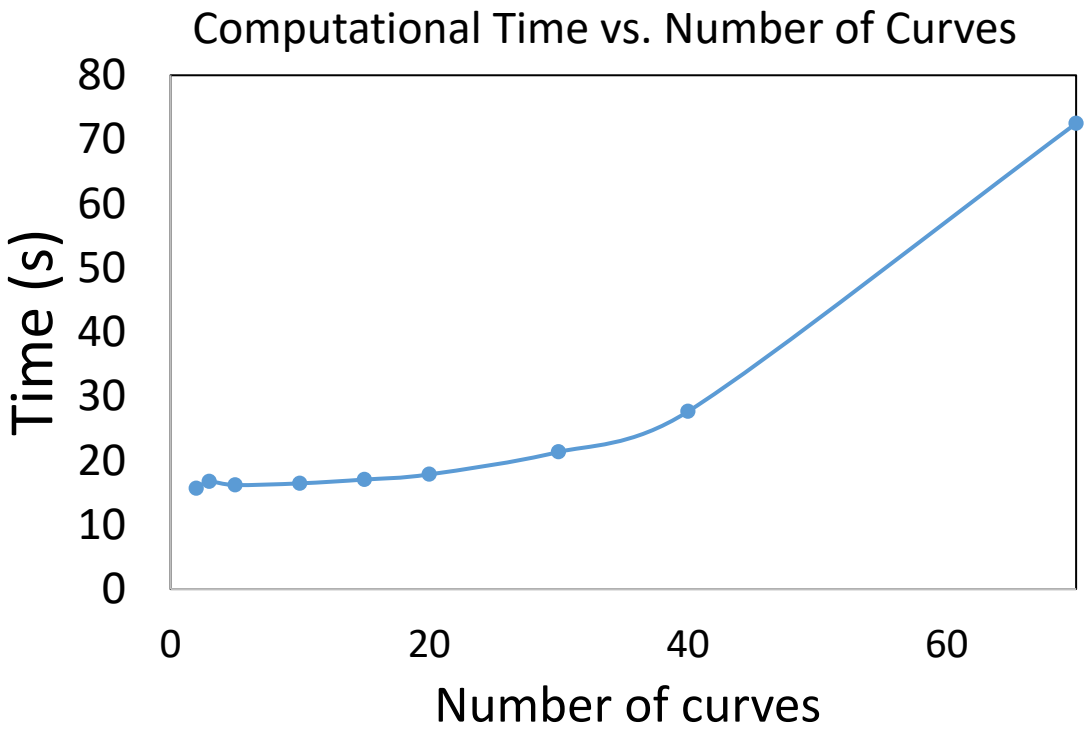

Figure 59: Computational time vs. the number of curves when performing the reconstruction algorithm.

Hemispheric volume calculated from Equation 11 and the reconstructed hemisphere are plotted on Figure 60 with variable number of curves. The percent error compared to the calculated hemispheric volume was less than 5% when using 15 curves or more. Twenty curves will be used in the reconstruction of the test specimens during pressurization to reduce overall computational time.

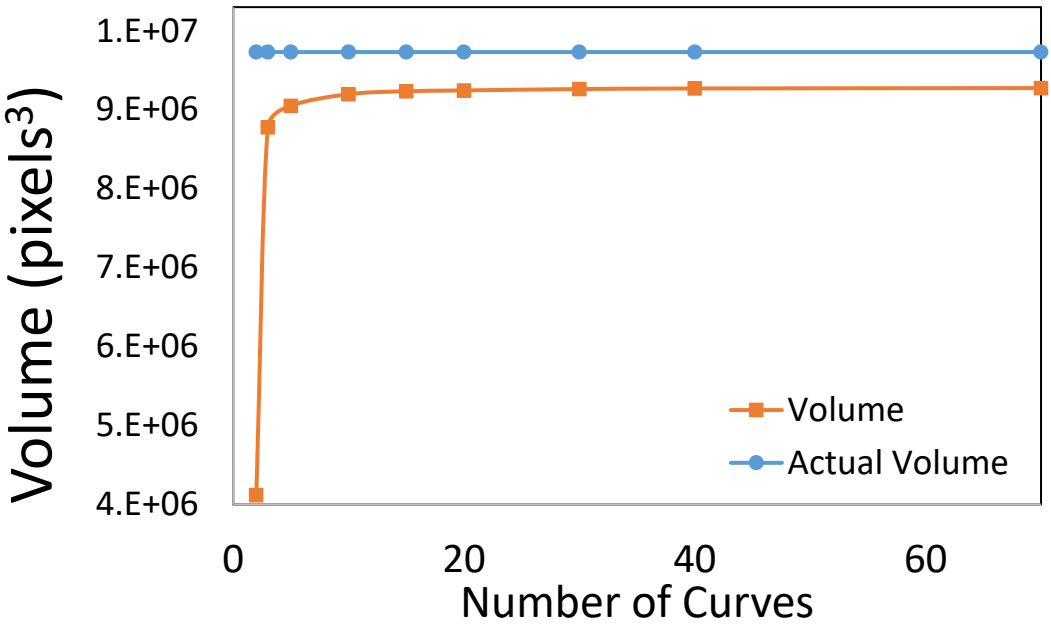

Figure 60: Volume of hemisphere using a range of intermediate curves from 2 to 70 per quadrant.

2.9 – AUTOMATIC BIT DATA ACQUISITION

A base that holds the automatic BIT clamp and two cameras orthogonally was constructed along with a backdrop (Figure 61). Figure 62 represents the entire automated BIT assembly. A video calibration protocol is initiated prior to performing the stepwise pressurization of each specimen. During the protocol, the user

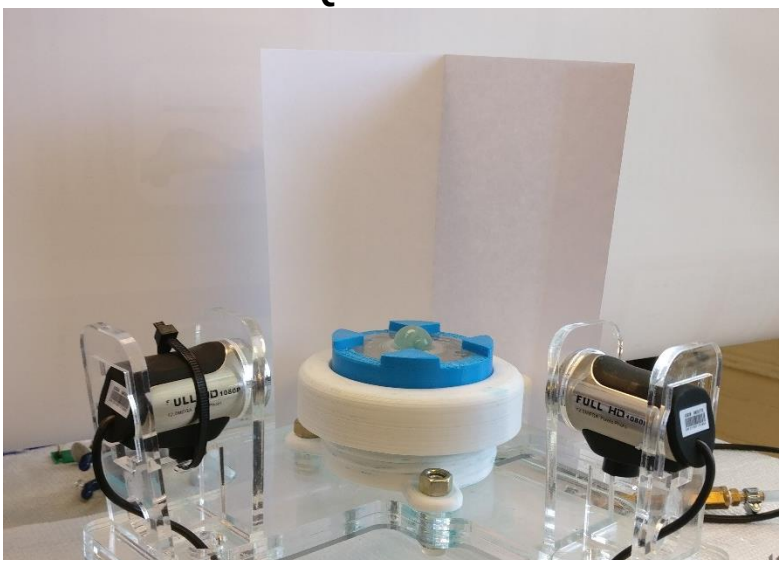

Figure 61: Two orthogonally placed cameras with a backdrop

masks off a region of interest that captures the base of the specimen and reference points that are found in blue in figure 63, the width of these reference points are 33.1 mm (for pixel to millimeter scaling).

After the video calibration is performed, a MATLAB script reads in serial

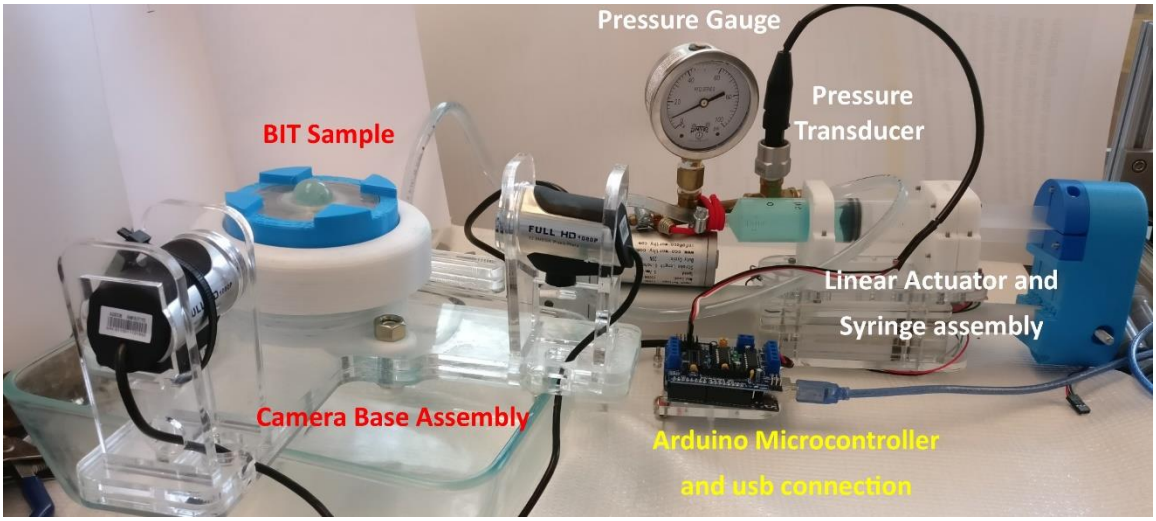

Figure 62: Assembled automated BIT assembly.

data from the Arduino board in real time during the stepwise pressurization load.

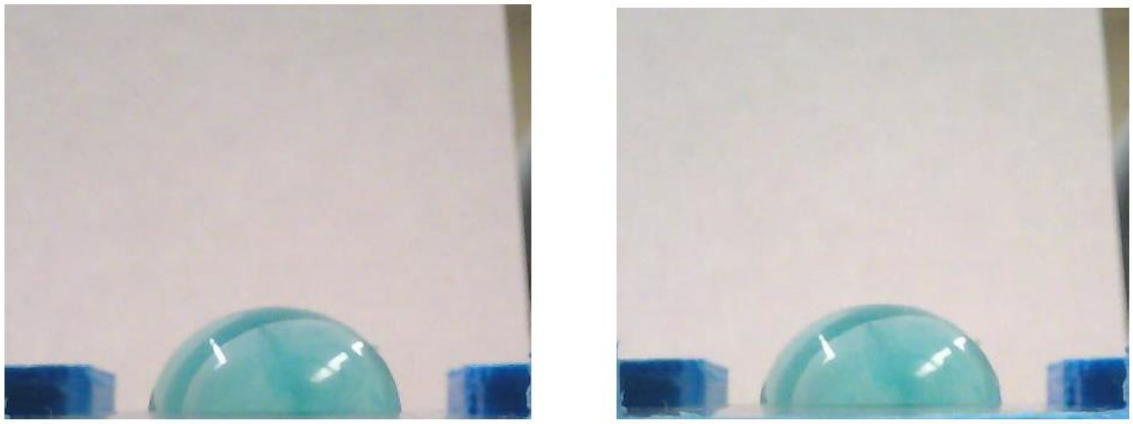

Figure 63 Two orthogonal view of a silicone sample.

A trigger variable from the Arduino board informs the two cameras to take a

snapshot while exporting the analog pressure value simultaneously for reference of the pressure and volume change after reconstruction. Figure 63, displays the orthogonal snapshots during pressurization.

The pressure volume relationship is a post-processing step after the

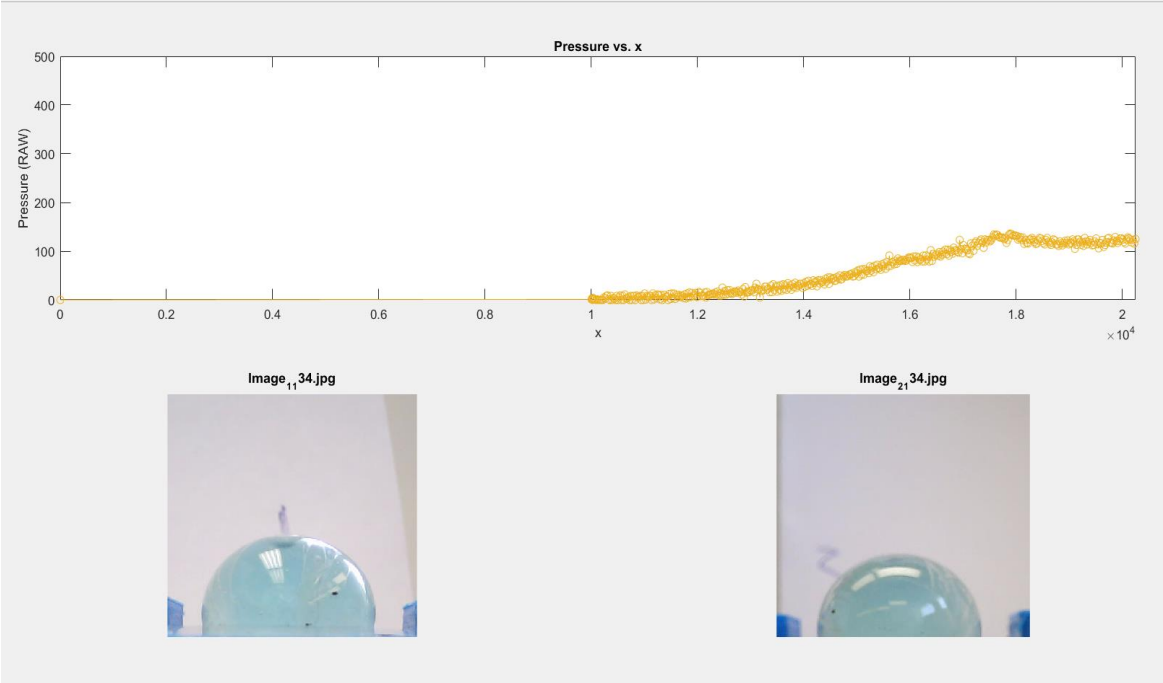

Figure 64: Real time pressure data and orthogonal snapshots.

snapshots and stepwise pressurization is completed. Figure 64 displays the real-time pressure information in analog values per iteration, while the cameras display the region of interest of both the front and side view. Simple image processing was used to segment the specimen from the background. After the geometry has been reconstructed, the volume is calculated.

2.10 – AUTOMATED BIT DISCUSSION AND CONCLUSION

An automated BIT apparatus composed of 3D printed components, basic electronics (Arduino and pressure transducer) with a simple software control system, a serial read interface and a two-camera imaging system to reconstruct specimens was developed. It was demonstrated that the reconstruction method was suitable in capturing volume information (section 2.8.4) but it is unclear on how accurately material heterogeneity can be captured using this method (i.e. calculate stress at various points during pressurization). The automated BIT apparatus accomplished successful rupture of a bovine aorta specimen and is discussed in section 3.5.

The reconstruction method for the automated BIT is post processing step that allows for quick reconstruction of the surface geometry at a given pressure. Due to an initialization error, the automated BIT failed to capture one orthogonal view of the ruptured bovine aorta sample and the reconstruction was not performed. Additional experimentation with silicone samples were performed to ensure the two-camera system was operational, but these data sets were not used to reconstruct the three-dimension surface because of their homogeneity. A simple PID control system and a stepwise pressurization was developed to test specimens with the automated BIT. However, the limitations of the system included the viscoelasticity of the tubing and the nonlinearity of the specimen. Further testing needs to be performed to understand where the data acquired from the automated fit in the current methods for multiaxial failure testing.

CHAPTER 3 - AIM 2: MULTIAXIAL AND UNAXIAL FAILURE PROPERTIES OF BIOLOGICAL SOFT TISSUES AND SILICONE

INTRODUCTION

Comparison between multiaxial and uniaxial failure properties is of great interest as uniaxial extension has been the primary mode of understanding material strength in biological soft tissues[14,33,35]. Several materials were investigated including non-fibrous silicone, fibrous bacterial cellulose and bovine aorta. As mentioned previously, several groups have begun to look at multiaxial failure properties[14,33–36,75] and have found material heterogeneity during experimentation. The capabilities of the automatic BIT did not include localized stress calculations, therfore localized material heterogeneity cannot be addressed. However, the design of the manual BIT allows for adjacent samples to be tested that allow for understanding localized weaknesses in a biological soft tissue. It is not yet apparent how uniaxial failure properties relate to multiaxial failure properties or even if a relationship exists. The purpose of the following experiments is to shed light on whether a relationship between multiaxial and uniaxial failure properties exist in fibrous biological soft tissues.

3.1 – FAILURE TESTING METHODS

It was necessary to develop testing protocols for both the uniaxial extension tests as well as the manual BIT experiments. These were the two apparatus' that were used to compare failure properties. The automatic BIT has its own self-contained methodology found in sections 2.6 – 2.10. Both uniaxial

and the manual BIT were used to test bovine aorta, bacterial cellulose and silicone. Silicone is non-fibrous and is homogeneous and isotropic whereas the bovine aorta and bacterial cellulose are considered to be fibrous, heterogeneous and anisotropic biological soft tissues. The comparison of fibrous and manmade materials will aid in understanding if failure occurs in a preferred fiber orientation.

3.1.1 Uniaxial Extension Testing Methods

Uniaxial extension test requires samples to be cut prior to experimentation. The desirable aspect ratio of uniaxial specimens is 4:1, however, a compromise of 3:1 was made due to the size of procured bovine aorta specimens. The bovine aorta specimens were cut in longitudinal and circumferential strips outside of the manual BIT specimen orifice area. All uniaxial extension test specimens had an aspect ratio of 3:1 or a specimen gauge length of 15 mm and a width of roughly 5 mm. Specimen thicknesses were measured with a digital caliper and recorded prior to testing. Preconditioning was performed at 3 mm/min for one cycle prior to extension, and the extension rate chosen was 9 mm/min for bovine aorta and 15 mm/min for silicone due to its high strain. Each specimen is hydrated prior to extension to prevent desiccation during uniaxial failure tests. A commercially available uniaxial extension tester (INTRON) was used to test all of the specimens. Post processing included calculating stress, tension and strain.

Failure stress and tension are defined as the maximum stress or tension calculated for a given uniaxial extension test. As evident in equations 1a,b, tension is the preferred metric to report as thickness is not required as thickness

is an uncontrollable experimentally measured quantity. However, both metrics will be reported.

3.1.2 Manual BIT Methods

One of the reported advantages of the manual BIT was the ability test a large number of adjacent specimens without the need for cutting them out of the entire material. Tests on planar bacterial cellulose sheets were performed in this manner, but not for bovine aorta due to the practical constraints of having a tubular vessel. Each specimen is loaded onto the laser-cut stage pieces and colored water is filled into the top acrylic clamp piece to calculate volume displacement. The colored water serves two purposes: clear indication of the water column level and the hydration of the biological soft tissues during experimentation. The screw-type syringe found in section 2.4.3. was used to push water into the compliant balloon, whereby applying the load to the

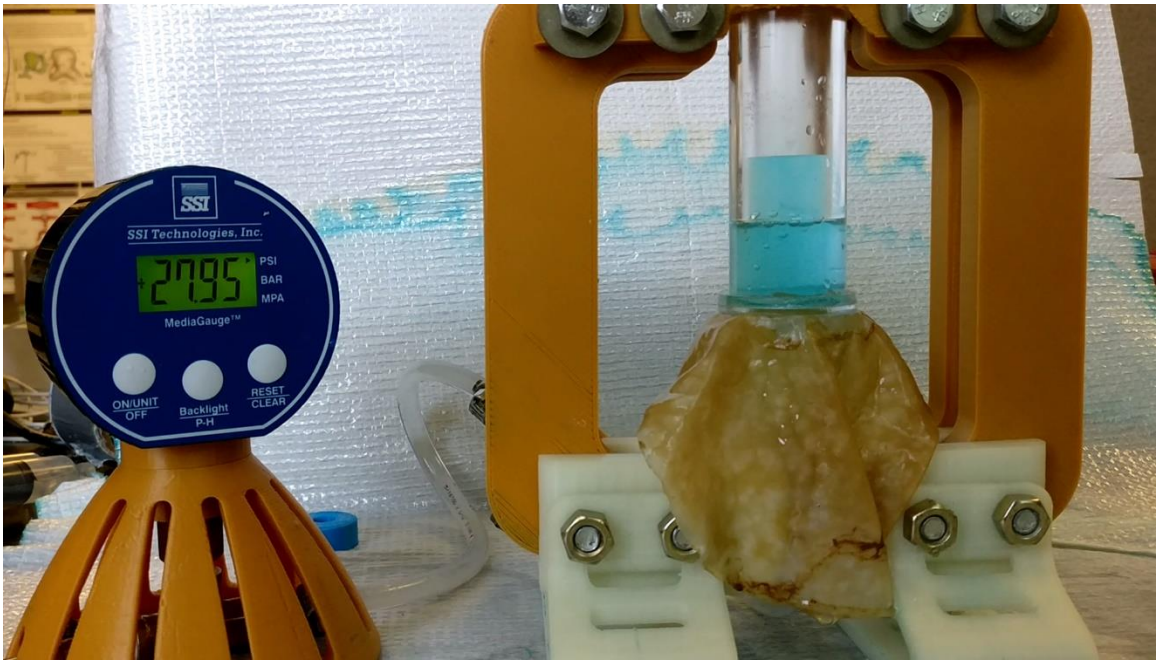

Figure 65: Manual BIT with bacterial cellulose specimen.

specimen. Figure 65 is representative of the setup with the pressure gauge being visible with a planar sheet of bacterial cellulose loaded.

Video recordings of each experiment were taken to extract the pressure-volume relationship and calculate the failure stress and tension right before specimen rupture (failure properties). After the specimen was unloaded, additional photographs were taken of the rupture (both the lumen and adventitia layers) to make note of how each specimen failed.

3.2 – FAILURE TESTING WITH SILICONE

It was previously mentioned that silicone would be tested to failure as it is a non-fibrous and homogeneous isotropic material. The comparison between multiaxial failure properties of silicone are found in section 4.2.3. XPS-565 silicone from Silcones, Inc. was molded into flat sheets in a round dish. Five BIT experiments were performed with silicone and 12 uniaxial extension tests were performed with silicone and the failure properties were compared.

3.2.1 – Manual BIT with Silicone

Figure 66 and Table 6 summarizes the BIT experiments along with reporting peak tension and stress (calculated by the method prescribed in section 2.1.3). The average thickness of the silicone sheets was 1.33 ± 0.165 mm, average failure stress was 178.9 ± 34.6 N/cm^2, and average failure tension was

22.4 ± 4.42 N/cm. It was noted that the rupture site had a semicircular jagged shape and did not have any preferred direction of failure.

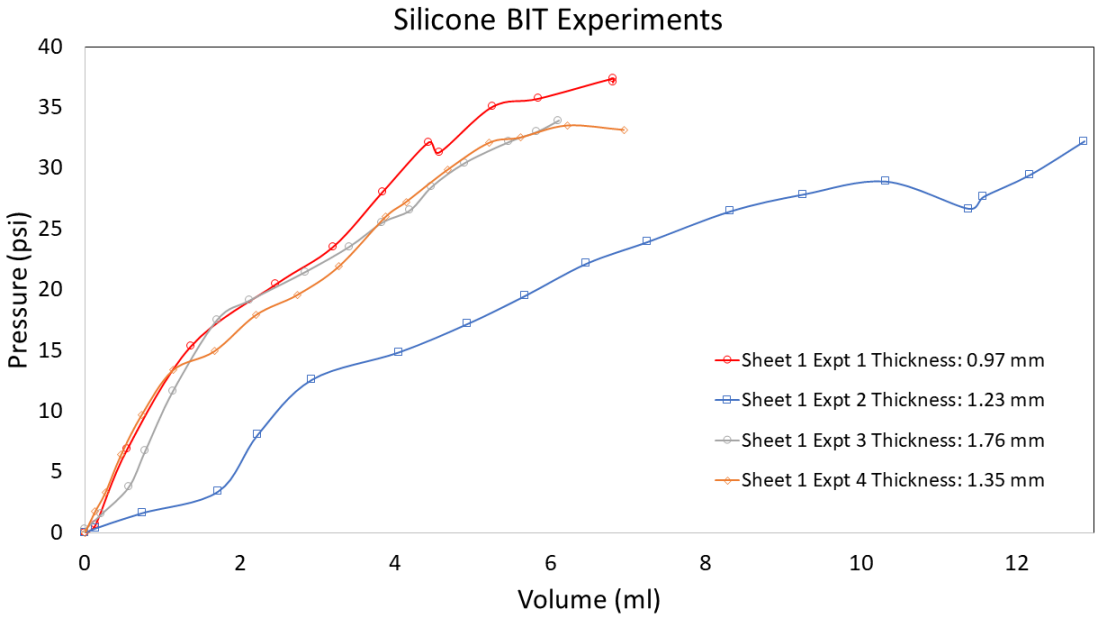

Figure 66: Pressure volume with silicone sheets.

Table 6: Summary of multiaxial failure properties.

Experiment	Thickness	Failure Stress	Failure Tension
Sheet 1 expt 1	0.97 mm	281.4	27.3
Sheet 1 expt 2	1.23 mm	159.9	19.7
Sheet 1 expt 3	1.76 mm	142.0	25.0
Sheet 1 expt 4	1.35 mm	132.3	17.9

3.2.2 – Uniaxial Extension Tests with Silicone

Figure 67, 68 report the uniaxial stress-strain and tension-strain curves while Table 7 summarizes the uniaxial experiments with silicone reporting thickness, failure stress and failure tension. Experiment 3 slipped at the clamp

and was not included in the analysis. The average thickness of the silicone specimens was 2.22 ± 0.49 mm, average failure stress was 256 ± 90.9 N/cm^2, and the average failure tension was 26.2 ± 6.2 N/cm. Because silicone does not contain any fiber, failure occurs rapidly and the stress goes to zero as soon as the specimen tears.

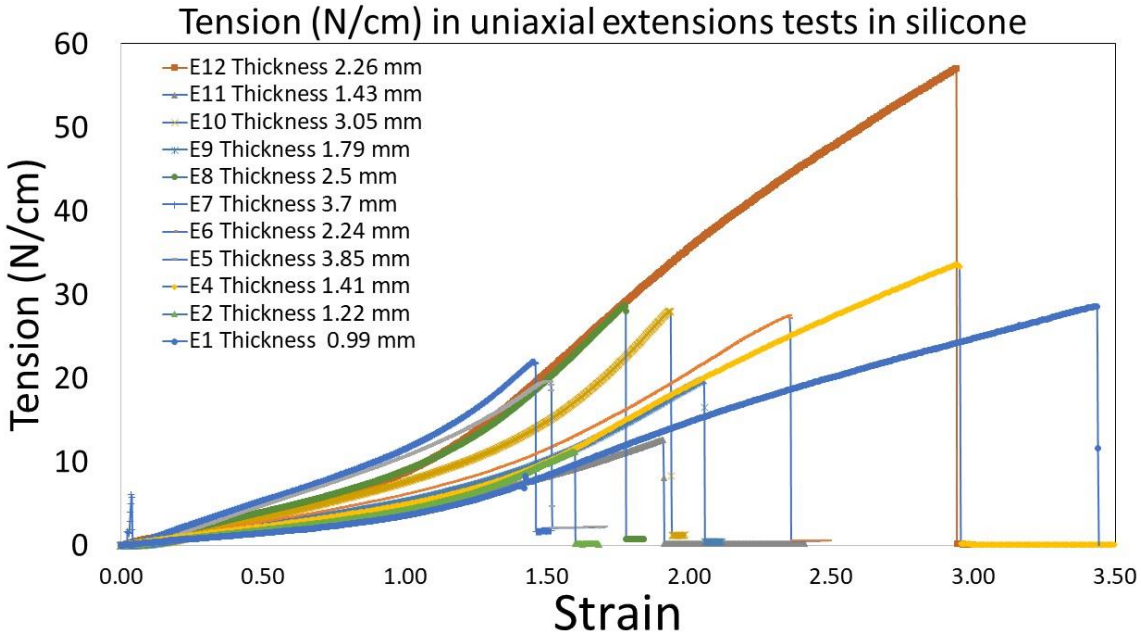

Figure 67: Uniaxial extension tests tension-strain curve.

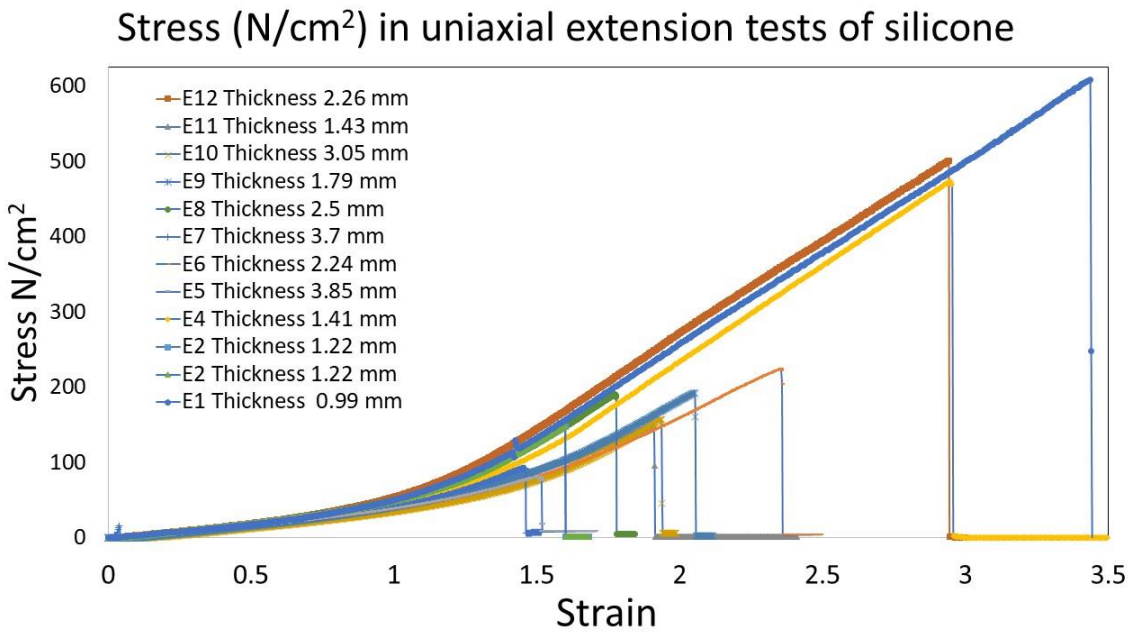

Figure 68: Uniaxial extension tests stress-strain curve.

Table 7: Summary of uniaxial extension tests in silicone.

	Thickness (mm)	Stress (N/cm^2)	Tension (N/cm)
Experiment 1	0.99	608.20	28.59
Experiment 2	1.22	147.97	11.20
Experiment 4	1.41	473.41	33.59
Experiment 5	3.85	80.64	19.62
Experiment 6	2.24	224.42	27.46
Experiment 7	3.7	92.90	21.93
Experiment 8	2.5	191.03	28.67
Experiment 9	1.79	192.82	19.76
Experiment 10	3.05	157.40	28.03
Experiment 11	1.43	150.07	12.58
Experiment 12	2.26	501.35	57.07

3.2.3 – Comparison of multiaxial and uniaxial failure in silicone

A statistical comparison between the failure properties of the BIT and uniaxial extension tests were performed using a Mann-Whitney test. Albeit, the sample size is small for both the BIT experiments and uniaxial extension tests, the statistical analysis can quantify any statistical significance between the failure properties of multiaxial BIT experiments and uniaxial extension tests. It was found that there was no statistical difference between multiaxial and uniaxial failure properties in silicone for both tension ($p = 0.21$) and stress ($p = 0.29$) in Figure 69. This finding supports the notion for a non-fibrous homogeneous material, the material behaves similarly in multi-axial failure and uniaxial failure.

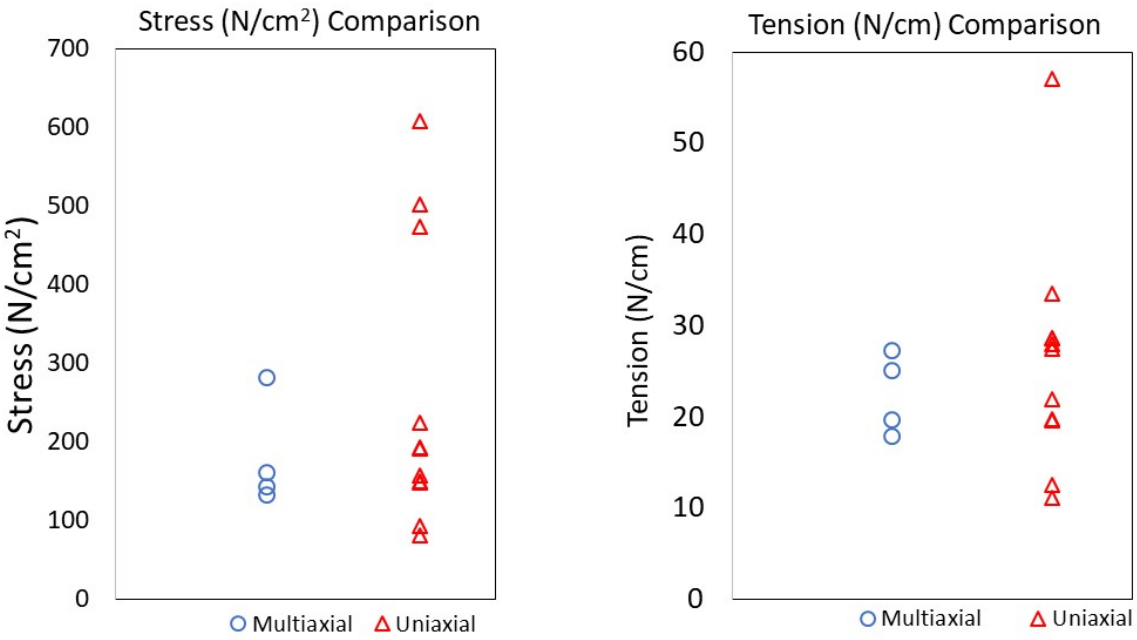

Figure 69: Multiaxial failure properties comparison with stress and tension in silicone.

3.3 – MULTIAXIAL FAILURE PROPERTIES OF BIT WITH BACTERIAL CELLULOSE

Partially dehydrated bacterial cellulose sheets derived from Kombucha tea was obtained for BIT testing (as the generation of sheets of bacterial cellulose is not within the scope of this study). The bacterial cellulose sheets were preserved in distilled water and manual BIT experiments were performed. Bacterial cellulose is considered to be a heterogeneous biological soft tissue with unknown fiber orientation. Manual BIT experiments were performed on each sheet without any additional cutting of specimens. This served as a pilot of testing adjacent specimens without interfering with the structural components of the material by any manner of cutting. Figure 70 display sheet 2 of the bacterial cellulose that

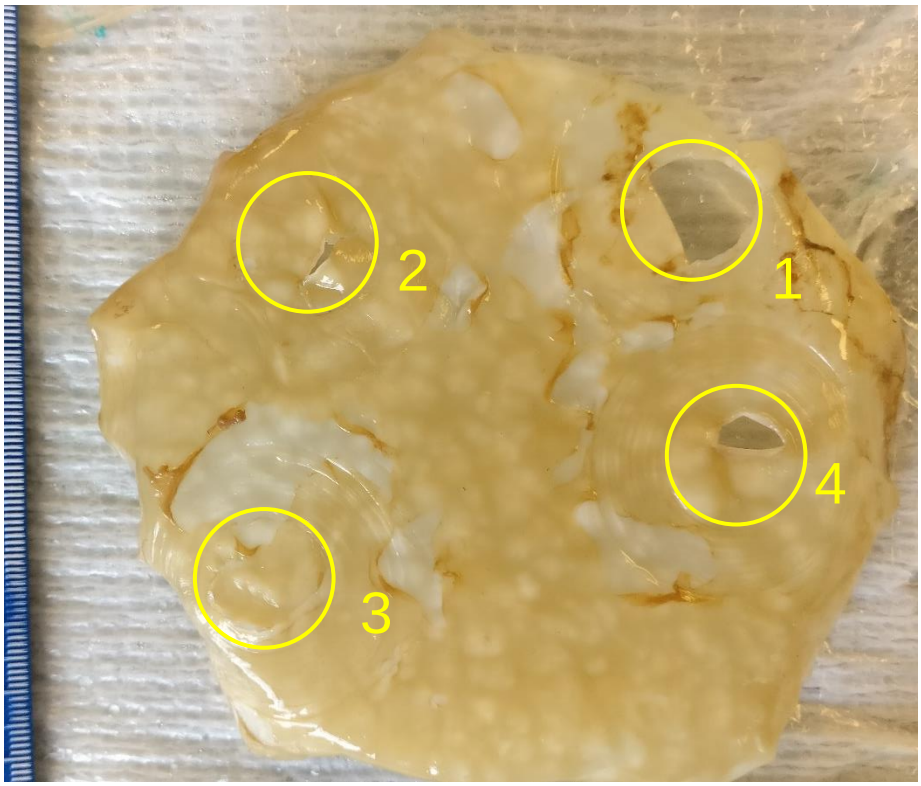

Figure 70: Sheet 2 of bacterial cellulose.

had qualitatively more material heterogeneity. Impressions from the stage pieces

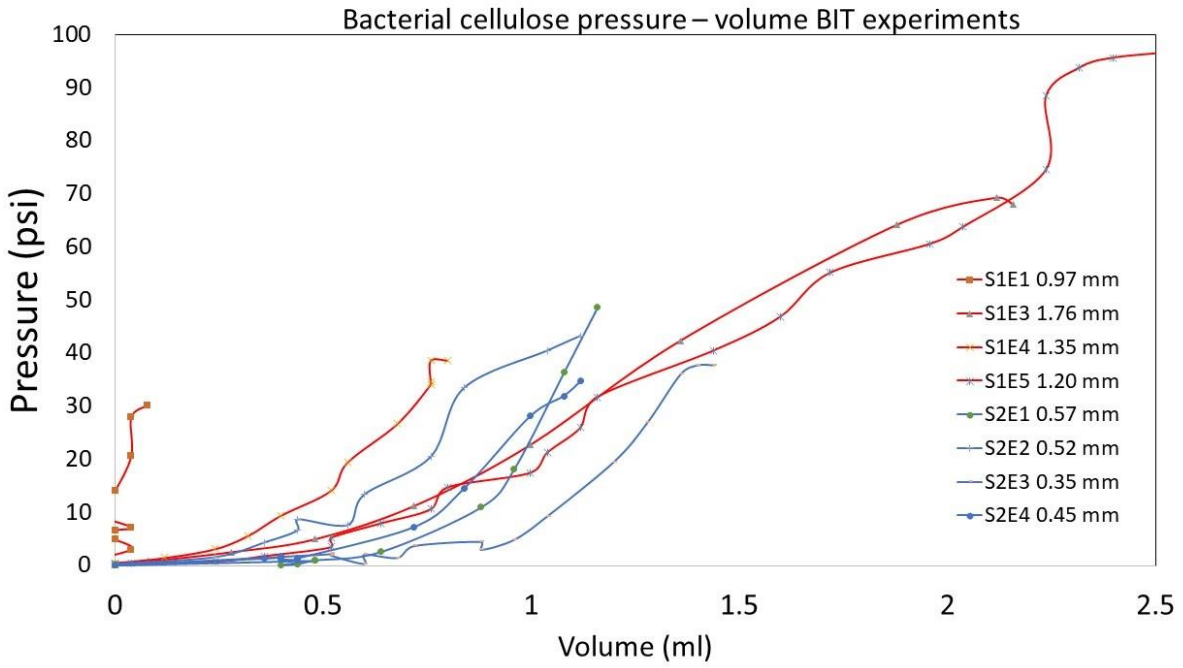

Figure 71: Pressure-volume data of all bacterial cellulose experiments with BIT.

were made along with several rupture sites of the bacterial cellulose sheet. Thickness measurements were performed prior to experimentation at the center of the specimen area to be tested. Bacterial cellulose did not rupture at the

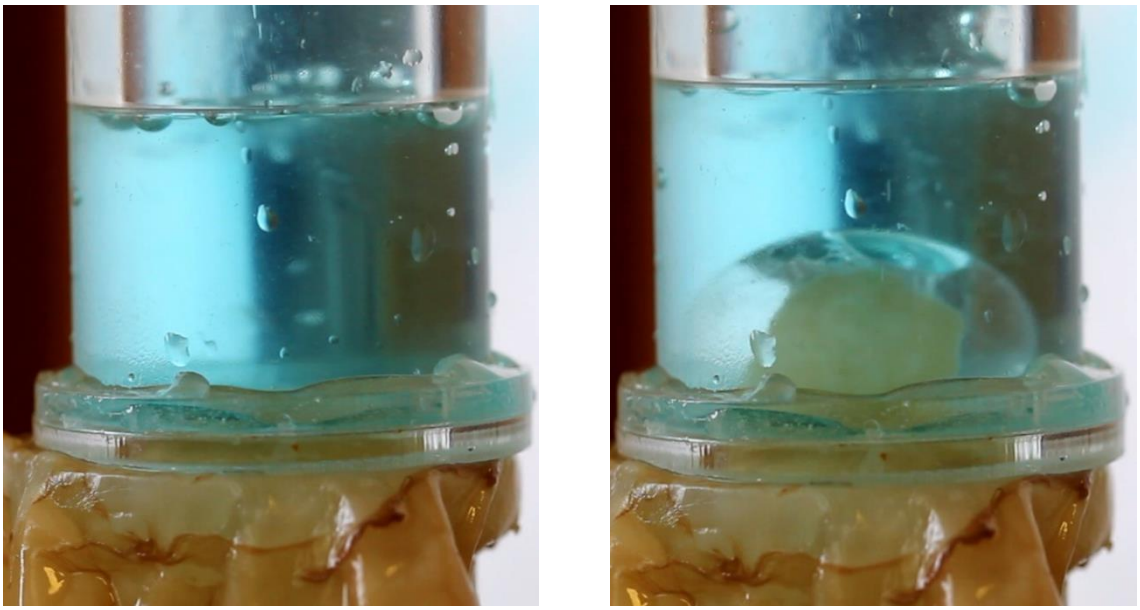

Figure 72(a): Bacterial cellulose low strain behavior before rupture (b)after rupture.

center specimen during experimentation as experiment 4 ruptured away from the center of the specimen orifice area. This is an indication that the BIT is able to capture localized weaknesses and that specimens will not always rupture at the center.

Unfortunately, due to the low strain behavior exhibited by the bacterial cellulose, stress calculations could not be performed. Figure 71a shows the bacterial cellulose several frames before rupture displaying how the stage pieces occluded the bacterial cellulose and Figure 71b shows the moment of failure of the bacterial cellulose. The inability to calculate stress for bacterial cellulose, uniaxial extension tests were not performed and their respective failure properties were not compared. However, pressure-volume data was compiled for each bacterial cellulose experiment. Figure 72 displays all the bacterial cellulose samples with their respective thickness in mm (red line for sheet 1 and blue line for sheet 2). At one site of testing (Sheet 1 experiment 5) a bacterial cellulose had a maximum volume change of 2.5 ml and had a peak pressure of 97.53 psi. The ability to test adjacent sites with the manual BIT is benefit as the specimen procurement time is greatly reduced. However, it is worth mentioning that measuring thickness with a digital caliper may not be possible for specimens that are close to the center of the material and that the hydration for adjacent sites of the sheet is necessary during experimentation.

3.4 – FAILURE TESTING OF BOVINE THORACIC AORTA

A two-foot segment of a bovine thoracic aorta was retrieved from a local butcher's shop within 24 hours of death. Fatty tissue and connective tissue were

carefully removed using a scalpel and stored in a 0.9% saline solution. Figure 73 displays the processed bovine aorta in saline solution.

Figure 73: Bovine aorta with removed fat and connective tissue.

The bovine aorta was cut in rings starting with the distal end towards the aortic arch, and two specimens per ring was tested with manual BIT. The thickness of the aortic tissue increases proximally and is noted in section 4.4.1. After the successful rupture of a specimen, 5 mm wide specimens were cut in the longitudinal and circumferential orientation away from the specimen orifice area for further experimentation with the uniaxial extension tester. Furthermore, the rupture sites on two specimens (circumferential tear and multi-direction tear) were imaged using differential interference contrast (DIC) microscopy to visualize collagen fiber alignment.

3.4.1 – Manual BIT with bovine aortic tissue

Figure 74 and Table 8 summarizes the BIT experiments along with reporting peak tension and stress (calculated by the method described in section 2.1.3). The average thickness of the bovine aortic tissue was 4.19 ± 0.75 mm, average failure stress was 139.1 ± 56.5 N/cm^2, and average failure tension was 45.0 ± 8.15 N/cm. The primary direction of rupture occurred in the circumferential direction and is noted in Table 8, two specimens had oblique rupture and one specimen did not have a linear tear (oblique direction). Data from experiment 10 was not included in the analysis as the digital pressure gauge was occluded in its video.

Table 8: Summary of multiaxial failure properties in bovine aorta.

	Thickness	Rupture Orientation	Stress (N/cm)	Tension (N/cm)
Experiment 2	2.81	Circumferential	162.9	45.8
Experiment 3	1.69	Non-line Tear	300.6	50.8
Experiment 4	2.26	Circumferential	364.3	82.3
Experiment 5	3.49	Circumferential	104.8	36.6
Experiment 6	3.94	Circumferential	124.7	49.1
Experiment 7	4.71	Circumferential	80.1	37.7
Experiment 8	4.53	Circumferential	71.3	32.3
Experiment 9	5.17	Circumferential	82.5	42.6
Experiment 11	6	Multi-directional	42.3	25.4
Experiment 12	5.89	Multi-directional	81.3	47.9

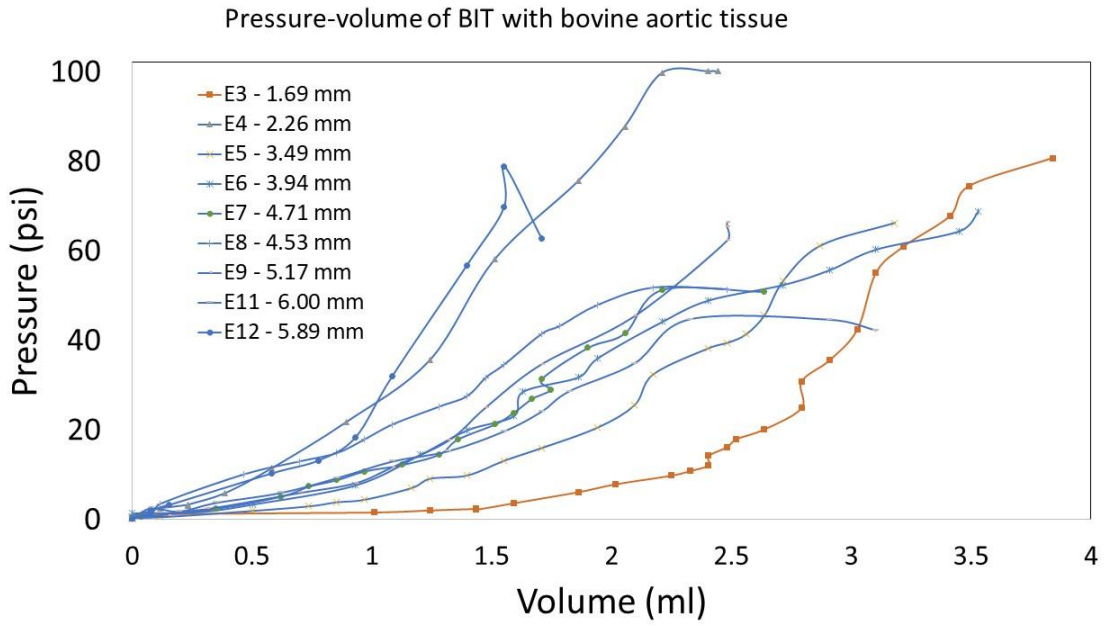

Figure 74: Multiaxial pressure-volume with BIT using bovine aortic tissue.

3.4.2 – Rupture orientation in bovine aortic tissue

It is relatively unknown how rupture propagates through the thickness of an AAA wall. Characterizing the orientation of the ruptured BIT specimens may shed light on the direction of rupture and the propagation of the tear through the thickness of the biological soft tissue. Although the exact moment of rupture is not captured, the ruptured samples provide invaluable information to whether a preferential fiber orientation exist, and the general direction of rupture (longitudinal or circumferential). Appendix I include photographs of the ruptured specimens displaying the lumen and adventitial views of each rupture site. Figure 75 and 76 is an example of ruptured specimen 11 (multi-directional rupture) and specimen 4 (circumferential rupture). The circumferential tear in specimen 4 has a longer visible tear on the lumen than the on the adventitia.

Experiments 11 and 12 were closest to the curved portion of the thoracic aorta and exhibited multi-directional rupture.

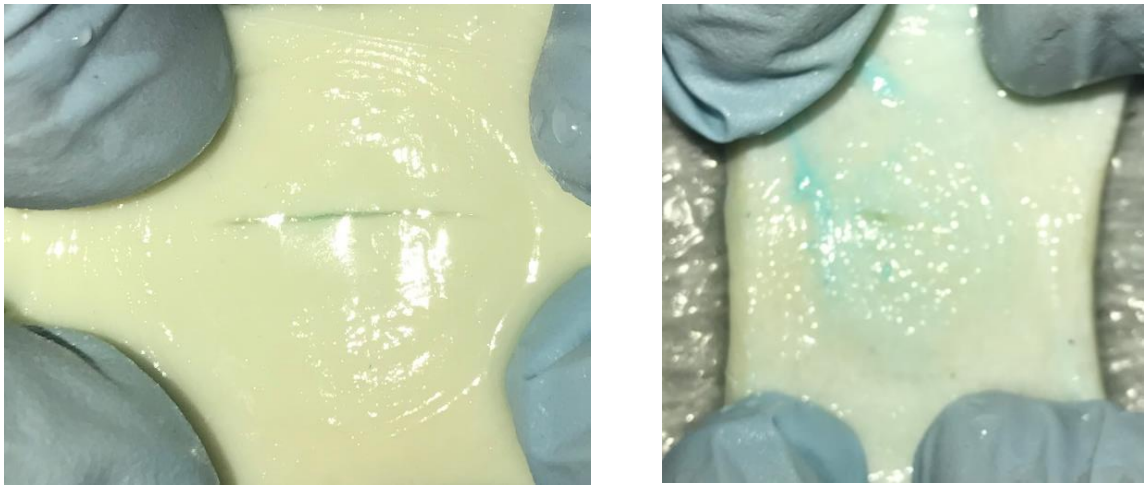

Figure 75: circumferential tear, inner and outer layer view for experiment 11.

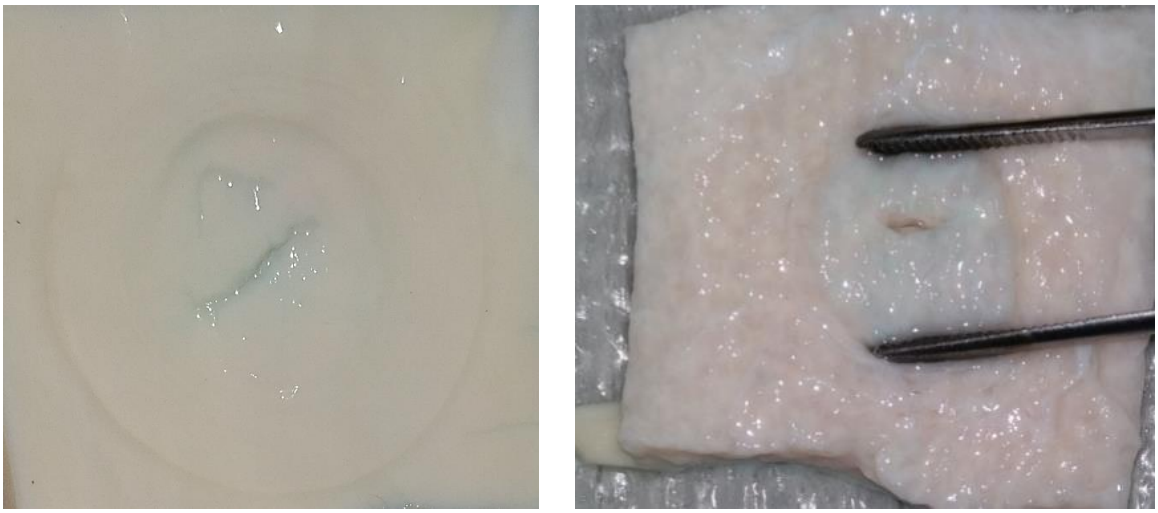

Figure 76: Oblique tear, inner and outer layer view for experiment 4.

Additional images using differential interference contrast microscopy at 4x and 10x optical zoom were captured in interest of viewing the collagen fiber orientation. No contrast agent was used to mark collagen fibers and the specimens had been stored in 0.9% saline solution. Each sample was loaded in

a glass petri dish with the circumferential axis as the x-direction and the longitudinal axis as the y-direction. Several images were taken of a circumferentially ruptured specimen and a multi-directionally oriented specimen.

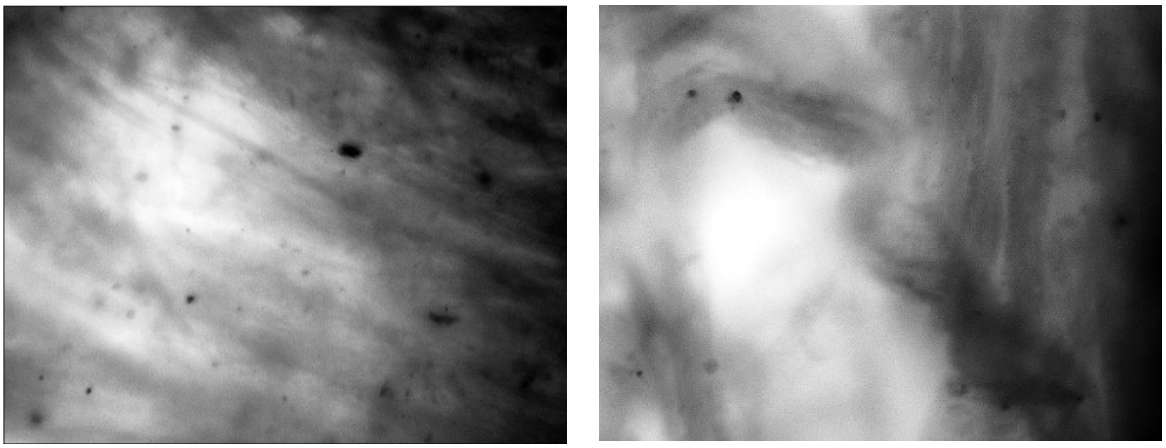

Figure 77(a) left edge of the rupture line (b) center of the rupture line.

There were difficulties to visualize the multi-directional tear due to its relatively large thickness (6 mm). Contrast enhancement and an unsharpen filter was performed on the images to improve fiber visualization. Figure 77a and 77b show the left edge of the rupture and the center of a circumferential rupture line (at 10x optical zoom). The left edge of the rupture site displays banded collagen fibers in the circumferential direction. It is demonstrated that the collagen bands have been disrupted at the central rupture site.

Figure 78a displays the lower left corner of the multi-directional tear at 4x zoom and figure 78b displays the center of the multi-direction tear at 10x zoom. The collagen fibers in both images do not appear to have any preferential orientation and discontinuities exist where ruptured occurred, this may be

attributed to the location of the specimen being closest to the proximal end of the thoracic aorta where the geometry begins to curve.

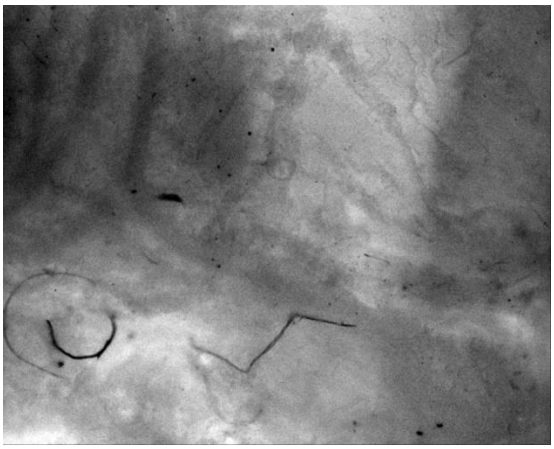
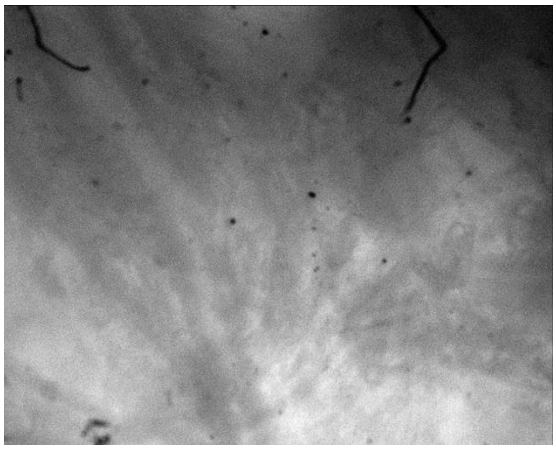

Figure 78 (a) lower left of the rupture line (b) center of the rupture line.

3.4.3 – Uniaxial extension tests with bovine aortic tissue

Uniaxial extension tests were performed in longitudinal and circumferential strips. These strips were procured from the surrounding tissue (outside of the BIT specimen orifice area) unused by the manual BIT experiments found in section 3.4.2. Table 9 summarizes the experiments that were performed on both longitudinal and circumferential strips. Due to the specimen size, specimen 3 did not have enough material to test a circumferential strip. Uniaxial extension tests were not performed on specimen 10 as there was no direct comparison to the BIT because of peripheral artery. It is reported that longitudinal specimens, the average thickness was 3.72 ± 0.65 mm, the average failure stress was 170.5 ± 90.26 N/cm^2 and the average failure tension was 30.03 ± 11.14 N/cm. It was also reported that circumferential specimens had an average thickness of 4.07 ± 0.63 mm, an average failure stress of 168.42 ± 34.12 N/cm^2 and a failure tension of 38.69 ± 2.33 N/cm.

Table 9: Summary of uniaxial failure properties in bovine aorta (L = longitudinal, C = circumferential).

	L Thickness (mm)	*C Thickness (mm)*	*L Failure Stress (N/cm)*	*C Failure Stress (N/cm)*	*L Failure Tension (N/cm)*	*C Failure Tension (N/cm)*
E1	2.50	2.06	111.33	337.70	18.78	45.90
E2	2.56	3.23	227.35	184.05	36.38	38.93
E3	1.83	-	475.03	-	58.84	-
E4	2.30	2.85	596.54	161.73	88.19	32.71
E5	3.29	2.83	83.01	235.00	19.07	44.48
E6	3.64	4.18	67.06	167.40	16.85	42.03
E7	4.58	4.73	79.58	136.96	21.81	40.66
E8	4.12	3.86	55.77	134.06	14.97	32.19
E9	5.54	5.41	83.12	126.74	26.14	40.86
E10	-	-	-	-	-	-
E11	4.71	5.84	57.69	101.04	15.13	34.17
E12	5.90	5.71	38.98	99.47	14.12	34.96

Comparison between longitudinal specimens and circumferential specimens were made for both stress and tension. Using a Mann-Whitney test, it was found that there was statistical difference of failure stresses between longitudinal and circumferentially oriented specimens ($p = 0.042$) and failure tension ($p = 0.016$). Figure 79a,b plot the peak stress and tension of longitudinal and circumferentially oriented specimens.

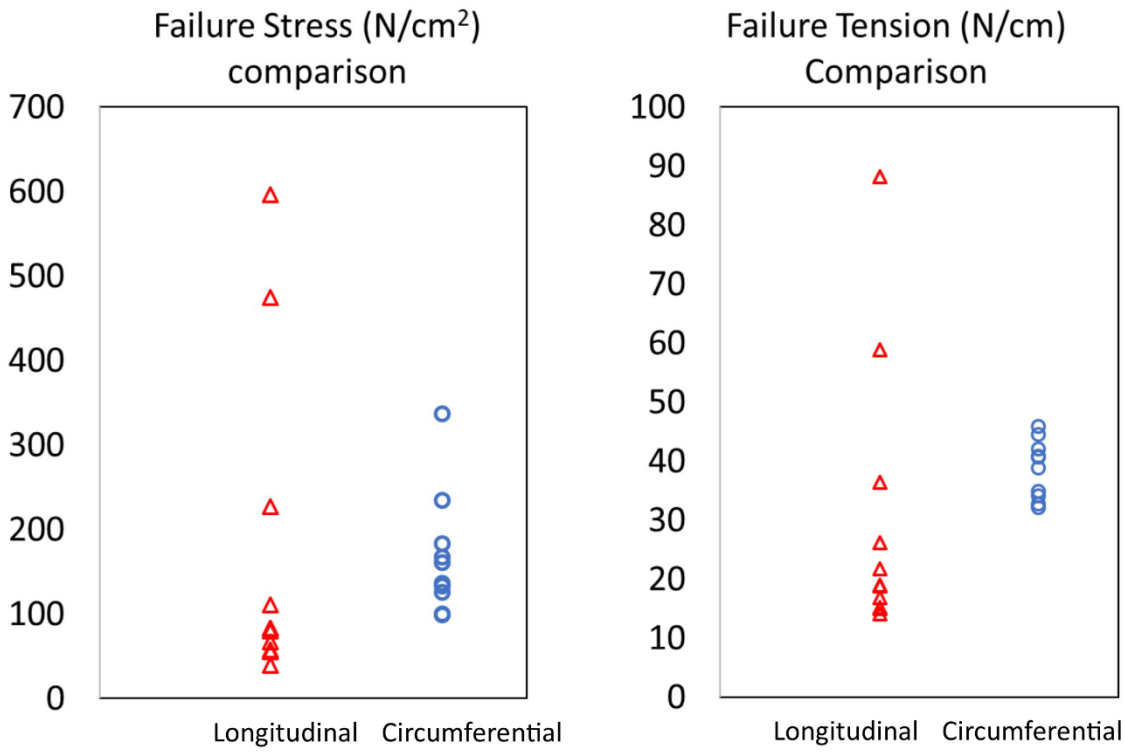

Figure 79(a): failure stress comparison between L and C strips (b) failure tension comparison. (L = longitudinal C = circumferential).

3.4.4 – Comparison of multiaxial and uniaxial failure properties in bovine aortic tissue

Multiaxial and uniaxial failure properties (stress and tension) were measured experimentally using the BIT apparatus and uniaxial extension tester. Two BIT experiments (11, 12) exhibited oblique tears and one experiment did not have line rupture (experiment 3). Experiments 2, 4 – 9 with the BIT experienced rupture circumferentially. Longitudinal and circumferential specimens taken from the BIT specimens were tested uniaxially and their failure properties were compared. Tables 10 and 11 display only the circumferentially oriented ruptured specimens and failure stress and tension are reported for each experiment type.

Table 10: Paired multiaxial failure stress of multiaxial and uniaxial tests.

	BIT Failure Stress (N/cm^2)	*Longitudinal Failure Stress (N/cm^2)*	*Circumferential Failure Stress (N/cm^2)*
Experiment 2	162.9	227.4	184.1
Experiment 4	364.3	596.5	161.7
Experiment 5	104.8	83.0	235.0
Experiment 6	124.7	67.1	167.4
Experiment 7	80.1	79.6	137.0
Experiment 8	71.3	55.8	134.0
Experiment 9	82.5	83.1	126.7

Table 11: Paired multiaxial failure tension of multiaxial and uniaxial tests.

	BIT Failure Tension (N/cm)	*Longitudinal Failure Tension(N/cm)*	*Circumferential Failure Tension (N/cm)*
Experiment 2	45.8	36.4	38.9
Experiment 4	82.3	88.2	32.7
Experiment 5	36.6	19.1	44.5
Experiment 6	49.1	16.8	42.0
Experiment 7	37.7	21.8	40.7
Experiment 8	32.3	15.0	32.2
Experiment 9	42.6	26.1	40.9

Figure 80, 81 plots BIT failure stress, tension against the uniaxial failure stress, tension in both longitudinal (red) and circumferential (blue) orientations. It is reported that multiaxial failure stress was more linearly related to longitudinal failure stress ($R^2 = 0.969$) than circumferential failure tension ($R^2 = 0.0191$). It was also found that multiaxial failure tension was more linearly related to longitudinal failure tension ($R^2 = 0.89$) than circumferential failure tension ($R^2 = 0.175$).

Table 12: Paired failure tension of multi-oriented rupture.

	RUPTURE ORIENTATION	FAILURE TENSION (N/CM)	LONGITUDINAL FAILURE TENSION	CIRCUMFERENTIAL FAILURE TENSION
EXPERIMENT 2	Circumferential	45.8	*36.4*	*38.9*
EXPERIMENT 3	Multi	50.8	58.8	-
EXPERIMENT 4	Circumferential	82.3	88.2	32.7
EXPERIMENT 5	Circumferential	36.6	19.1	44.5
EXPERIMENT 6	Circumferential	49.1	16.9	42.0
EXPERIMENT 7	Circumferential	37.7	21.8	40.7
EXPERIMENT 8	Circumferential	32.3	15.0	32.2
EXPERIMENT 9	Circumferential	42.6	26.1	40.9
EXPERIMENT 11	Oblique	25.4	14.1	34.2
EXPERIMENT 12	Oblique	47.9	88.2	35.0

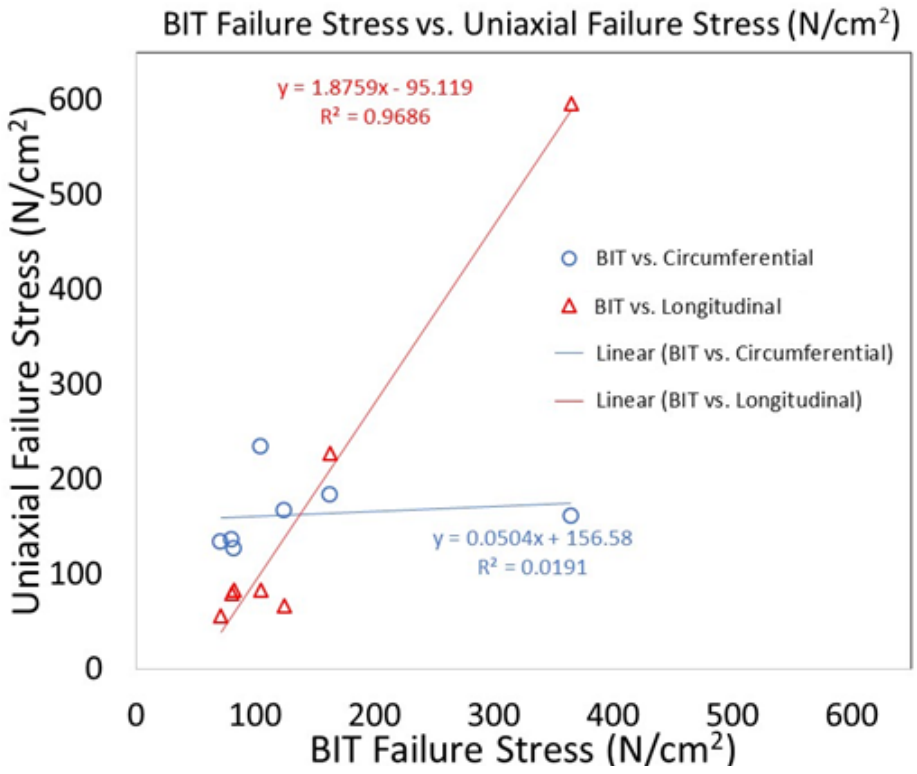

Figure 80: BIT failure stress vs. longitudinal and circumferential failure stress.

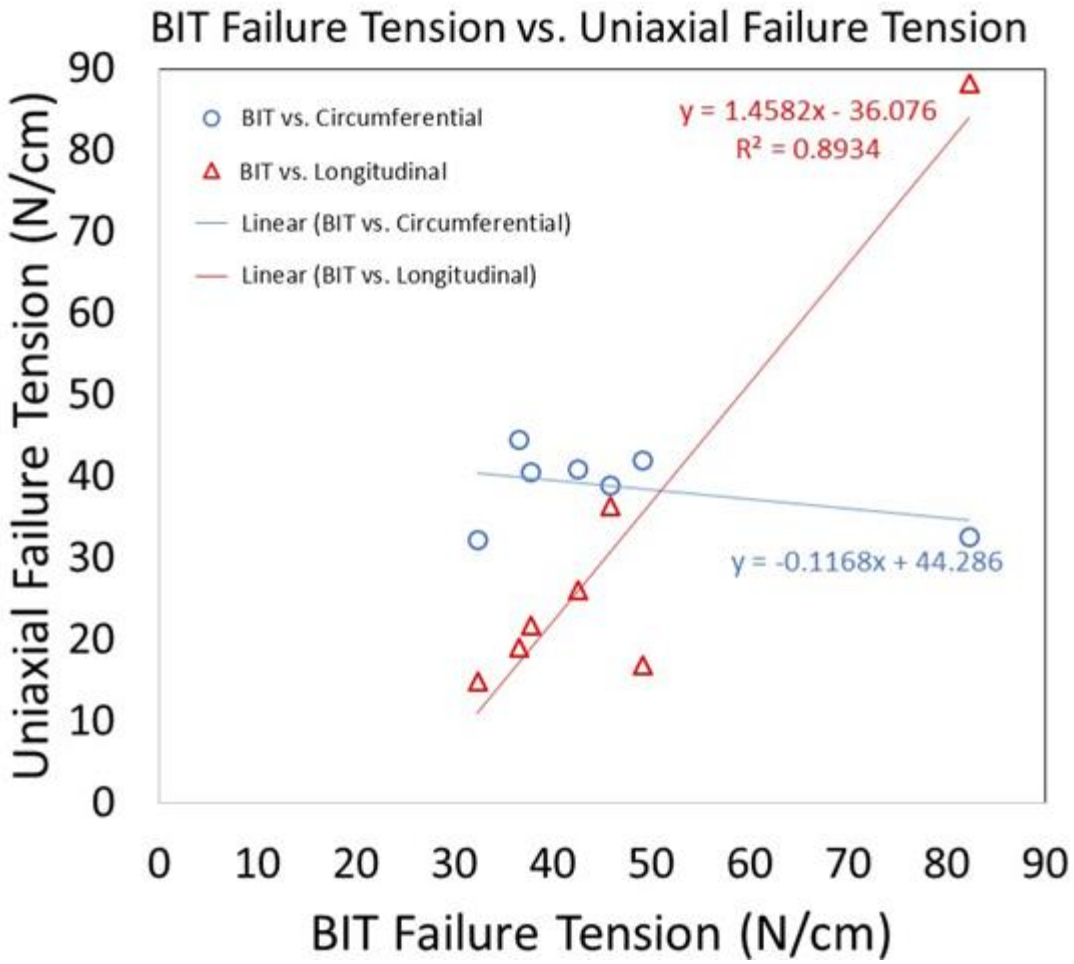

Figure 81:BIT failure tension vs. longitudinal and circumferential failure tension.

3.4.5 – Discussion of BIT and uniaxial failure properties

Multiaxial failure properties and uniaxial failure properties were reported in section 3.4.4. There have been very little reports of the multi axial failure properties of biological soft tissues, and the potential relationship (if any) between multiaxial failure and uniaxial failure remains unclear. It was reported for circumferential rupture, BIT failure properties shared a strong relationship with longitudinally oriented uniaxial failure properties. This is coherent as the circumferential rupture line was perpendicular to the longitudinal specimens. It

should be mentioned that the uniaxial failure properties were procured for surrounding tissue (8 mm to 15 mm radius from the center of the rupture line) and not directly adjacent to the rupture line. Although regional variations may exist in the bovine aortic tissue, the uniaxial failure properties were taken relatively close to the rupture site.

When the circumferentially oriented BIT failure properties were appended with the BIT experiments having oblique rupture lines, the relationship between BIT failure properties and longitudinally oriented uniaxial failure properties weakened (Figure 82). This is indicative of the fiber alignment not being longitudinally and circumferentially oriented. For both oblique tears (Experiment 11, 12), the circumferential failure tension was higher than the longitudinal failure tension. It is unclear if this would be the case for all oblique rupture as the sample size was small (n = 2).

This study comparing the multiaxial failure properties with uniaxial failure properties gives a first look if uniaxial failure properties have been a suitable metric for failure in fibrous biological soft tissues. It was found consistently with circumferentially oriented tear, a relationship between multiaxial failure properties and uniaxial failure properties exist. However, for oblique rupture orientation, it is not clear on what relationship (if any) can be found between multiaxial failure properties and uniaxial failure properties. Additional studies with fibrous biological soft tissue are necessary to confirm or refute aforementioned claims

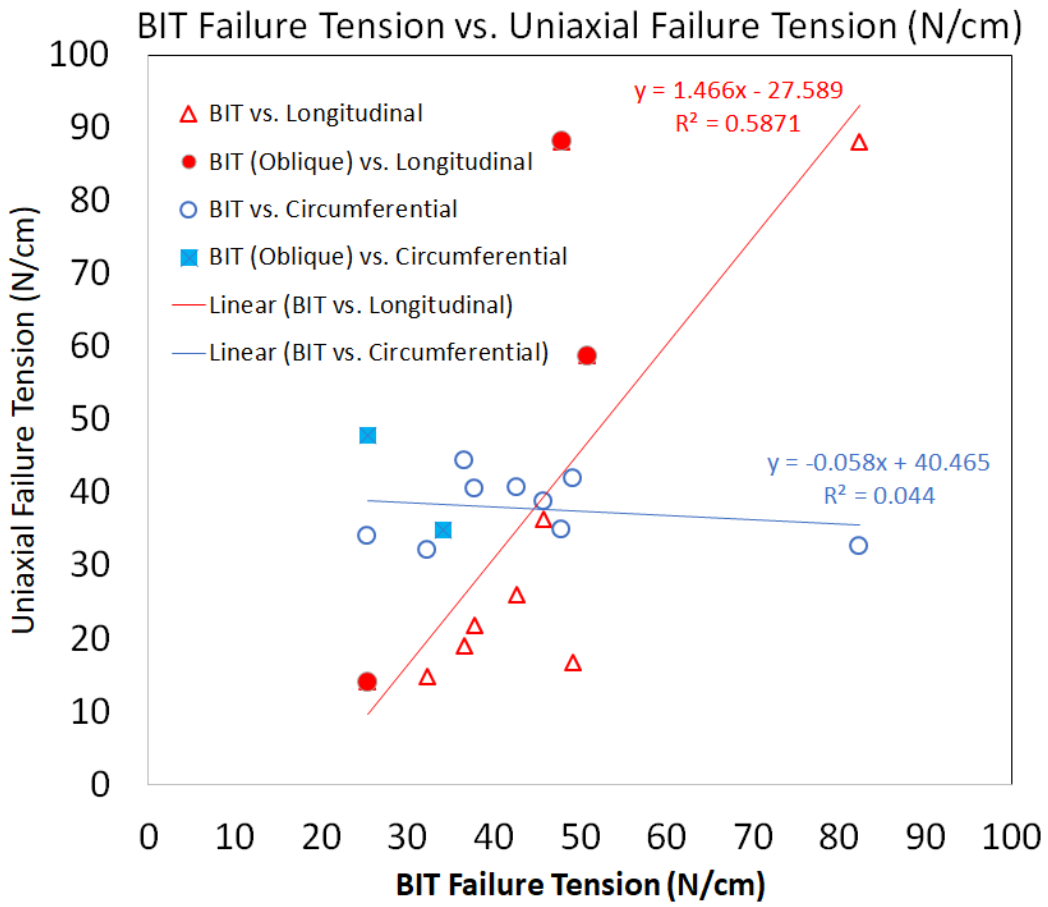

Figure 82: Failure tension with all multiaxial samples compared to oriented uniaxial failure tension.

3.5 – AUTOMATIC BIT FAILURE IN A BOVINE AORTA SPECIMEN

A single Automated BIT experiment with a bovine aorta specimen was performed. As the pressure limit of the automated BIT is 40 psi a 19 mm specimen orifice area was chosen to reduce the maximum stress required to rupture the specimen. This particular bovine aorta specimen did not undergo a catastrophic rupture through the thickness but slowly began to tear. Figure 83 displays the ruptured sample and the various fibers that are intact. The initial

tear appeared when the pressure reached 27.2 psi and the final pressure recorded was 31.7 psi. The failure tension when the initial tear propagated was 14.5 N/cm and stress was not reported because the thickness information was not recorded.

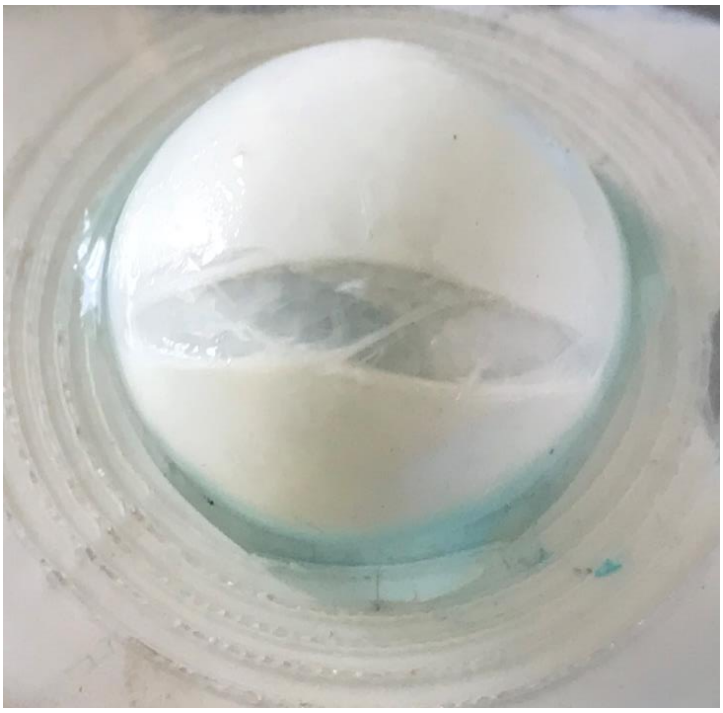

Figure 83: Ruptured bovine aorta using the automated BIT.

3.6 – IMPLEMENTATION OF THE AUTOMATIC BIT WITH A SILICONE SPECIMEN

A single sample of silicone was used with the automatic BIT to demonstrate the 3D surface reconstruction and pressurization of the sample to 44 psi. Figure 84 displays the paired images at a given pressure and their respective 3D surface that was reconstructed. Automatic segmentation was not possible due to the reflections from the lights on the silicone. The outlines of the

surface geometries were traced and reconstructed manually using the method discussed in section 2.9.

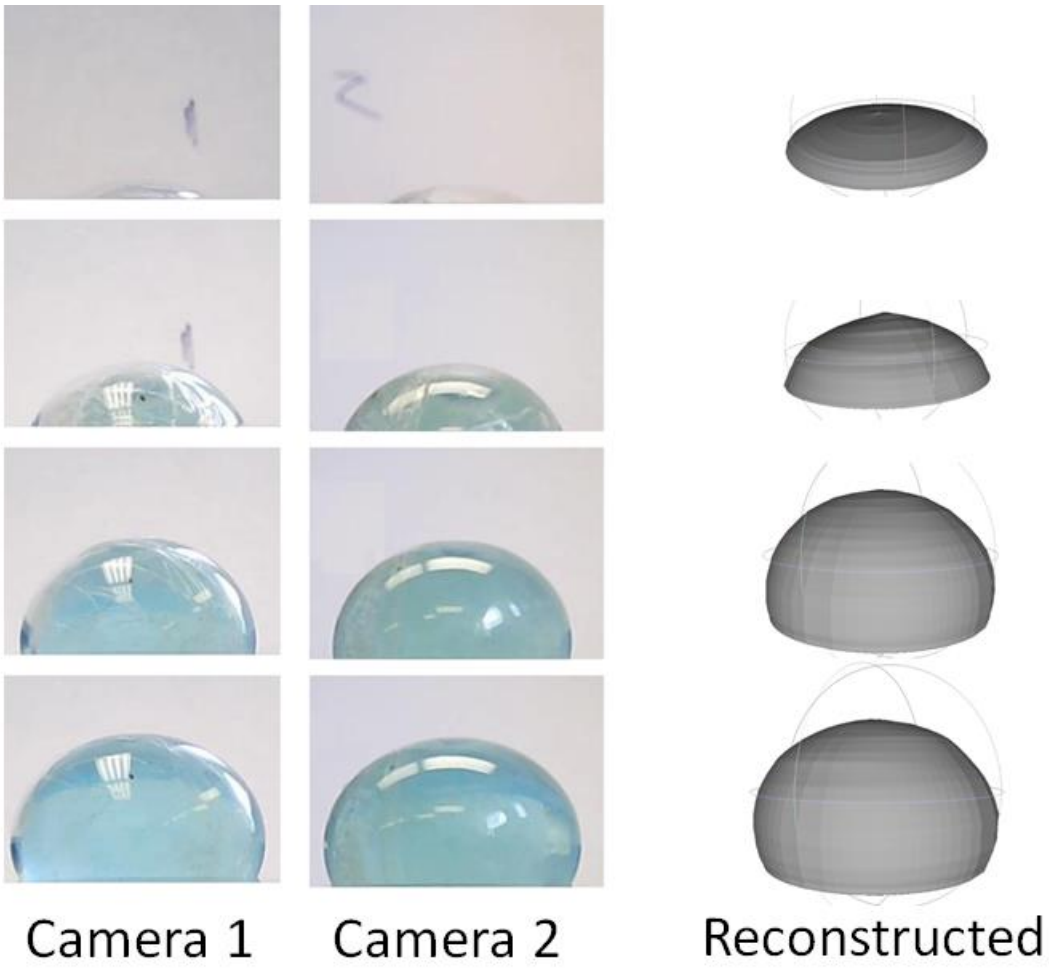

Figure 84: Pressurization of silicone specimens, 4 time-steps pressurized and their reconstructed geometry.

After the surface geometries were reconstructed, the volume was calculated in Meshlab. The pressure and volume relationship was recorded and Figure 85 includes the automatic BIT silicone experiment along with the manual BIT silicone experiments. The automatic BIT silicone did not rupture during experimentation unlike in the manual BIT experiments. The pressure volume relationship fits within the previously recorded manual BIT experiments.

However, as the pressure increased the silicone behaved stiffer. The stiff behavior could be a result of the specimen being thicker (2.25 mm) than the manual BIT silicone specimens (1.02 ± 0.34 mm).

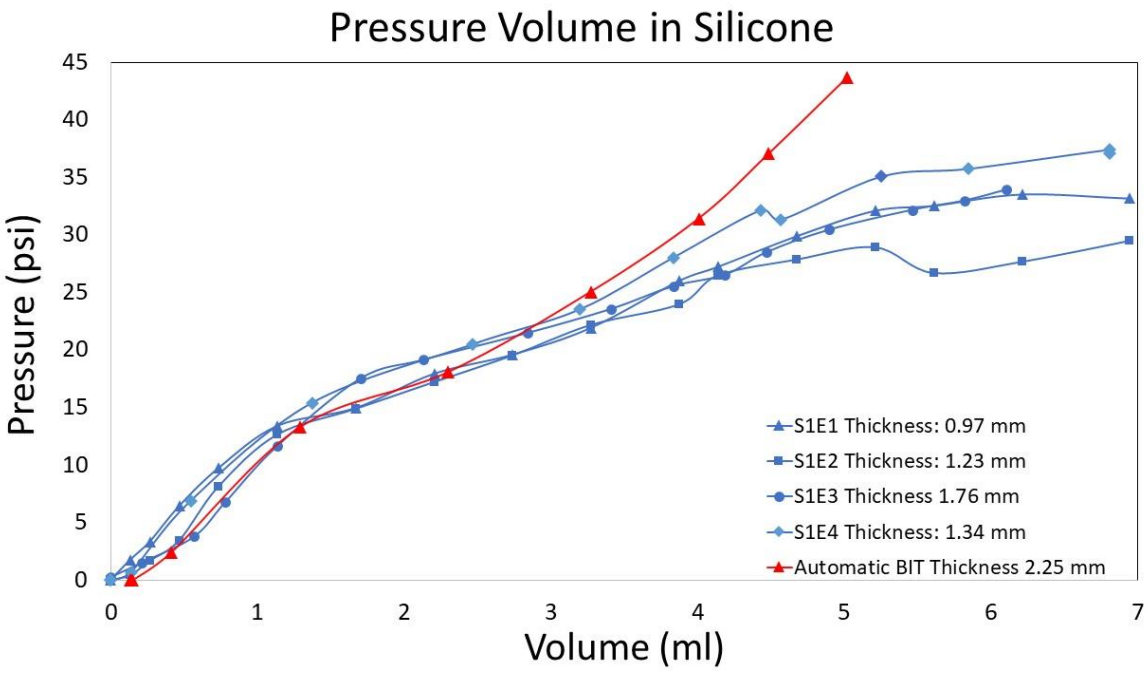

Figure 85: Silicone pressure-volume relationship with Manual (blue) and Automated BIT (red).

Validation was not performed to assess the results found in the automated BIT. Future implementation using the cameras will use a darker background along with avoiding direct light on the specimen to allow for robust automatic segmentation of the specimen during pressurization.

3.7 – MANUAL AND AUTOMATED BIT DISCUSSION AND CONCLUSION

Biological soft tissues (bovine aorta) was ruptured using both the manual and automated BIT. A single sample (n = 1) bovine aorta was ruptured using the automated BIT, but the reconstruction was not performed due to the second

camera not initializing. Further experiments were performed to ensure that the camera initialization problem was remedied. Another silicone sample (n = 1) was used to perform the entire surface reconstruction per time step. Although the implementation was successful, additional validation of the results is needed to ensure that the reconstruction pressure-volume methodology is suitable. It is not yet clear on whether localized stresses can be calculated from the reconstructed geometries and if the bi-plane curve evolution algorithm is suitable to capture material heterogeneity. The manual BIT was implemented in a larger number of samples that included silicone sheets, bacterial cellulose sheets and bovine aortic tissue. Stress analysis was performed for silicone sheets and bovine aortic tissue at a single time point right before rupture, whereas stress analysis could not be performed in bacterial cellulose due to the low strain not creating a deformation large enough to be analyzed. It was found that there was no difference between the uniaxial failure properties of a presumed homogenous isotropic material (silicone) and multiaxial failure properties. In bovine aortic tissue, multiaxial rupture predominantly occurred in the circumferential orientation. When compared to longitudinally and circumferentially oriented uniaxial extension tests in the same region, it was found that circumferentially ruptured multiaxial failure properties were correlative to of longitudinally oriented failure properties. However, it was undeterminable whether obliquely oriented multiaxial failure would relate to both longitudinally and circumferentially oriented uniaxial extension tests. Further studies that pair oriented multiaxial failure properties with oriented uniaxial multiaxial failure properties may improve the

reliability of the claims made in this study, also oblique multiaxial failure properties with their orthogonal counterparts may aid in understanding if oblique rupture is a localized phenomenon or due to fiber orientation in that region. Advantages of the manual BIT over the automated BIT include the ease of use, simplicity of data acquisition and the ability to measure a large number of samples whereas the automated BIT requires samples to procured from material sheets and it is yet to be determined if the automated BIT reconstruction method can capture material heterogeneity. Ruptured specimens exhibited across the thickness tears with the length of the tears being longer on the inner layer (lumen) than the outer layer (adventitia). It is unclear why this may have been the case, but this observation may be indicative what occurs when AAA develop. Mini tears may continue to propagate on the luminal side increasing clot (intraluminal thrombus) while the outer layer does not exhibit breaching of the wall. Future implementation of either BIT would benefit from a catheter camera on the luminal side during rupture experiments to record how the rupture progresses during pressurization.

CHAPTER 4 -AIM 3: ASSESS VARIOUS FAILURE CRITERIA USING COMPUTATIONAL MODEL OF RUPTURED AAA

INTRODUCTION

In a necropsy study of AAA, four ruptured and nine unruptured aneurysms were harvested whole from human cadavers. Wall thicknesses were measured with a digital caliper, histology was performed, and mechanical properties from uniaxial extensions testing of multiple strips resulted in a collection of elastic parameters and failure tension from the anterior, posterior and lateral regions of each aneurysm. The sparse data of wall thicknesses and elastic parameters were interpolated/extrapolated to all nodes (thickness) and elements (elastic parameters) using geodesic distance-weighted approaches. The resulting finite element model was a heterogeneous, variable wall thickness shell model subjected to a consistent systolic pressure. Appendix III gives reference to a manuscript in revision and includes the relevant information to this study in greater detail. The data that was collected allows for the first time, a thorough investigation into a potential causative role of peak wall stress and AAA rupture. The site of rupture is known and each ruptured AAA model includes failure properties (sparse) along with variable wall thicknesses. The wall stress to failure stress ratio and wall tension to failure tension ratio can be calculated through measured failure properties, rather than stochastically derived failure properties. Analysis revealed that while the median peak wall tension in the ruptured AAA was higher than that in the unruptured group, the sites of peak wall tension or the tension to failure tension ratio did not match the sites of ruptures.

This finding suggests that a better understanding and quantification of failure characteristics of AAA wall is important. Until the study in Aim 2 was completed, it was speculated that multiaxial failure properties differ from uniaxial failure properties but it was uncertain to what degree and what relationship if any existed. It was found for a fibrous anisotropic bovine aorta (biological soft tissue) that the circumferentially oriented multiaxial failure properties were correlated to longitudinally oriented uniaxial extension tests. This finding was important as the

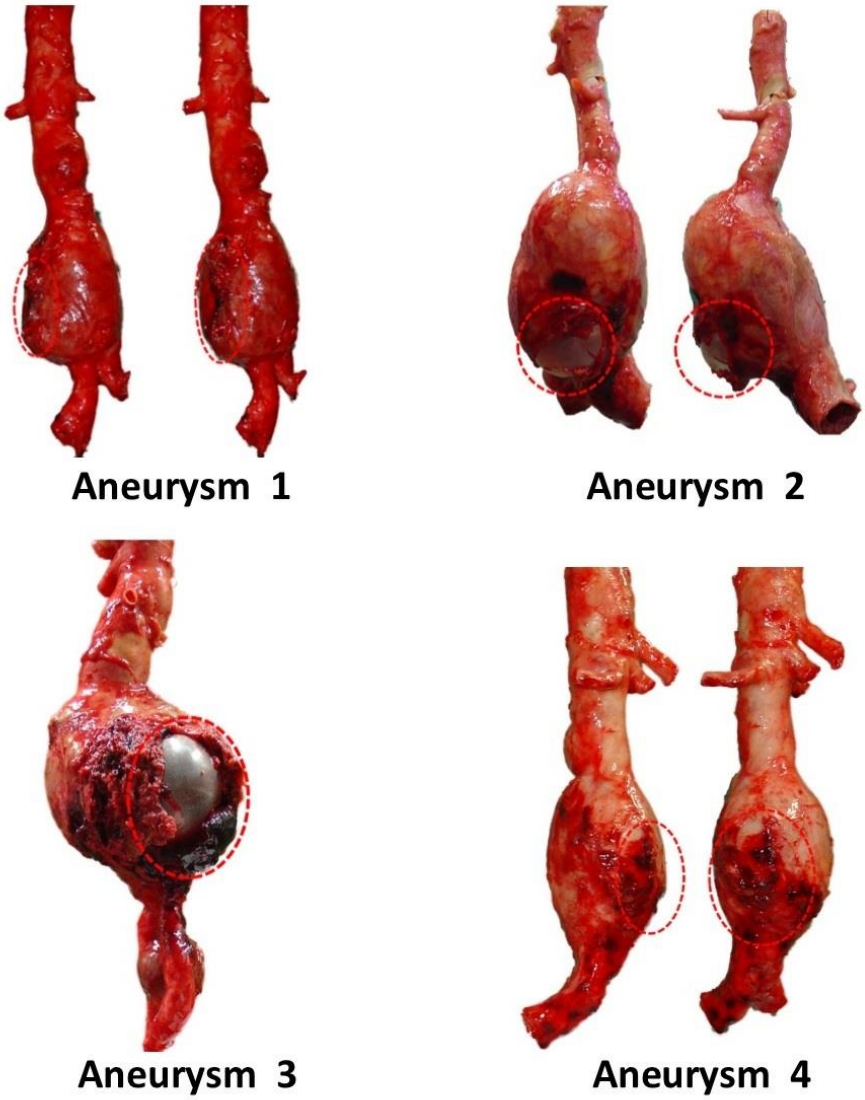

Figure 86: Four ruptured aneurysms and their rupture sites.

computational studies that integrated failure properties were taken in the longitudinal direction[6] and they are within reason of multiaxial failure properties, however it cannot be stated whether these uniaxial extension tests would have ruptured in an oriented manner using the BIT. Figure 86 are the original photographs taken at zero pressure with the rupture location highlighted.

Photographs that were taken were of the zero-pressure geometry of the AAA and the undeformed computational model is representative of this. In AAA computational studies, majority of the surface geometry is reconstructed using 3D imaging modalities (Computed Tomography or MRI) at normal systolic and/or diastolic pressures meaning the geometries have already been deformed to a certain degree. The primary advantage of having zero pressure geometry is the ability to have somewhat accurate strain and displacement data. In the past Lu et al performed inverse elastostatic stress analysis in predeformed AAA from in vivo images to find zero pressure geometry [76], but this step was not necessary as the digital photographs were taken at zero pressure. Aim III proposed to retrospectively analyze ruptured AAA with known rupture site(s) by finding alternative failure metrics that match with the geometric location of rupture. Additional analysis of only ruptured aneurysms (1 – 4) were performed and are reported in Appendix IV.

There are many indices reported in the field of AAA mechanics that hope to understand rupture at the material level through experimentation or at the environmental level through computational finite element analysis. Material indices are interrogated with uniaxial failure testing and the following indices

extracted includes: failure stress, failure tension, thickness and failure strain. Pressurizing *in silico* to ideal systolic pressure of aneurysm geometries retrieve indices that include: Principal stress (max, middle and min), Von Mises stress, Tresca stress and more recently tension (stress resultant). Generally, nodal displacement and strain metrics (strain energy and principal strains) are not reported due to the unreliability of the non-zero pressure geometry. The computational model used for ruptured AAA featured a zero-pressure geometry, variable wall thickness and material heterogeneity. Although, the material measurements were sparse, strain metrics are reported as a potential indicator of rupture location. Maximum principal stress, Von Mises stress, tension, strain energy and displacement magnitude will be reported as potential indices that may match with the rupture site in ruptured AAA.

4.1 - PRINCIPAL STRESS ORIENTATION IN RUPTURED AAA

Maximum principal stresses are typically reported for computational studies of AAA without reference to orientation. Qualitative analysis of maximum principal stress orientation was performed with four ruptured aneurysms as the direction of stress cannot be assumed. It was clearly shown for four ruptured AAA that the maximum principal stress was oriented in the circumferential direction (Figure 87 and Appendix II). However, as the aneurysm became more spherical in shape, the orientation information became unclear. Figures 87 displays the rupture site of aneurysm 3 and the maximum and middle principal stresses. It can be observed qualitatively that the region of rupture has a higher disruption of stress orientation in the spherical region in the middle of the AAA

rupture site. In the most spherical region of the aneurysm the max principal stress 'swirls' around a localized pole while the mid principal stresses seem to be longitudinally and circumferentially oriented at this localized pole. Although it cannot be presumed that rupture propagated from this localized pole, the jagged rupture line may be indicative of the manner in which the principal stress are oriented.

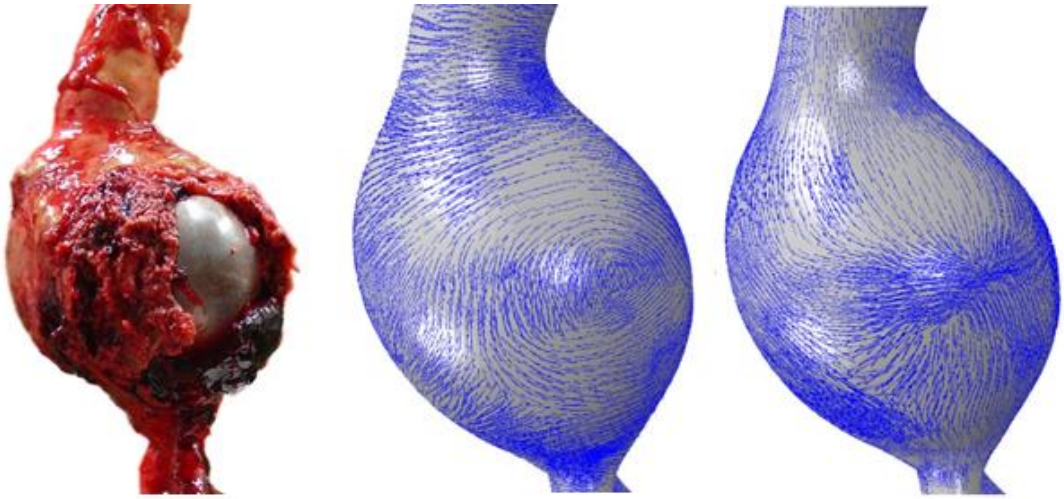

Figure 87: Rupture site location with maximum principal stress and middle principal stress of aneurysm 2.

Appendix II displays the three ruptured aneurysms and disruptions to the expected orientation of stress (max principal in the circumferential direction and mid principal in the longitudinal direction) are seen near the site of rupture.

4.2 – RUPTURE SITE AND COMPUTATIONAL INDICES

Rupture location is valuable in understanding AAA rupture and it is difficult to obtain unless excised from a cadaveric patient. After the geometric reconstruction was performed and the computational analysis performed, rupture site location was interrogated further. Figure 88 displays aneurysm 1 and ten

manually picked points off the textured surface model. Points were chosen from the proximal end of the rupture line to the most distal. This process was performed for the rest of the ruptured aneurysms and the following metrics were reported: Maximum principal stress (N/cm^2), Von Mises stress (N/cm^2), tension (N/cm). tension to failure tension ratio, displacement magnitude and strain energy. Table 13 reports the mean and standard deviation of the aforementioned indices for all locations in the ruptured AAA. Table 14 reports the rupture line means as a percentile of the entire aneurysm. Maximum principal stress and Von Mises stress had similar means and percentiles in the rupture line of each aneurysm. Displacement and strain energy also shared a similar relationship (percentiles only) in each rupture line. Large displacements may not always correlate to strain energy due to the unpredictability of aneurysm movement during simulation, in general the displacements and strain energy were ranked higher except for the mean strain energy in aneurysm 4. Table 15 reports the percentile of the maximum value of a given metric. It is reported that a consistent metric across all ruptured AAA does not exist.

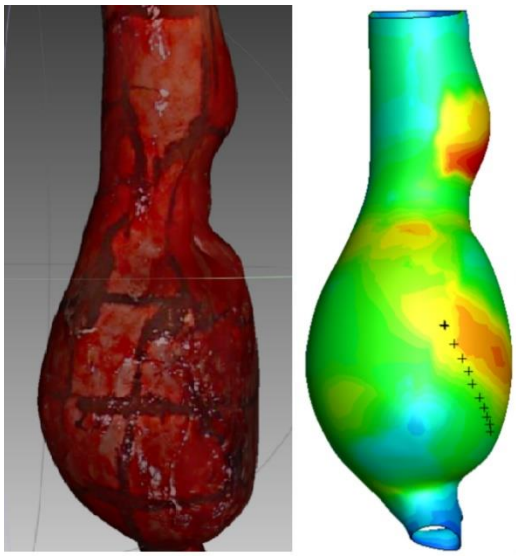

Figure 88: Rupture site and rupture line of aneurysm 1.

Table 13: Mean and standard deviation of various indices.

ANEURYSM	A1	A2	A3	A4
STRESS (N/CM^2)	16.5 ± 4	23.5 ± 6.13	21.1 ± 6.52	15.8 ± 4.6
MISES (N/CM^2)	14.6 ± 3.4	20.8± 5.35	19 ± 5.71	13.9 ± 4.1
TENSION (N/CM)	1.7 ± 0.28	3.35 ± 0.71	2.65 ± 0.71	2.82 ± 0.58
TENSION TO FAILURE TENSION RATIO	0.13 ± 0.02	0.27 ± 0.08	0.35 ± 0.14	0.37 ± 0.1
DISPLACMENT (MM)	0.14 ± 0.04	0.30 ± 0.11	0.28 ± 0.1	0.21 ± 0.07
STRAIN ENERGY PER UNIT VOLUME	0.82 ± 0.3	1.26 ± 0.49	1.00 ± 0.49	0.77 ± 0.28
STRAIN ENERGY PER UNIT SURFACE AREA	0.09 ± 0.025	0.21 ± 0.077	0.13 ± 0.052	0.15 ± 0.044

Table 14: Mean rupture line indices percentile.

ANEURYSM	A1	A2	A3	A4
STRESS	88	66	72	60
MISES	89	70	75	60
TENSION	74	59	60	56
RPI	79	98	64	72
DISPLACMENT	95	91	88	87
STRAIN ENERGY PER UNIT VOLUME	85	83	73	56
STRAIN ENERGY PER UNIT SURFACE AREA	80	84	63	62

Table 15: Percentile of the maximum metric in rupture line.

ANEURYSM	A1	A2	A3	A4
MAX PRINCIPAL STRESS	99	88	86	65
VON MISES	99	87	89	67
TENSION	97	84	71	61
NODAL DISPLACEMENT	99	94	93	90
STRAIN ENERGY PER UNIT VOLUME	95	91	92	70
STRAIN ENERGY PER UNIT SURFACE AREA	96	91	74	77
MAX PRINCIPAL STRAIN	80	87	72	68

Figure 89 display the rupture line plots of each aneurysm. The maximum principal stress and Von Mises stress are very similar (within 10% stress) as their quantities are directly related. Equation 12 describes how Von Mises stress is calculated from the principal components of stress and is a combination of these stresses.

Equation 12: Von Mises Stress calculation from principal stresses.

$$Von\ Mises\ Stress = \sqrt{\frac{(\sigma_1 - \sigma_2) + (\sigma_2 - \sigma_3) + (\sigma_3 - \sigma_1)}{2}}$$

$$where\ \sigma_1, \sigma_2, and\ \sigma_3\ are\ the\ max, mid\ and\ \min\ principal\ stresses$$

Strain energy is calculated by the historical deformation (strain) and the stress at that strain governed by the assigned hyperelastic coefficients of the material model during simulation. The calculation of strain energy occurs by

taking the integral (area under the curve) of the stress-strain curve per element. As the model has variable heterogeneity, each element undergoes a unique strain and in turn have different strain energies. However, the strain energy is based on stress-strain and not tension-strain meaning the thickness is accounted for and inversely related to stress. Therefore, strain energy per unit volume is grounded in stress and strain energy per unit surface area is based on tension (strain energy per unit volume multiplied by thickness).

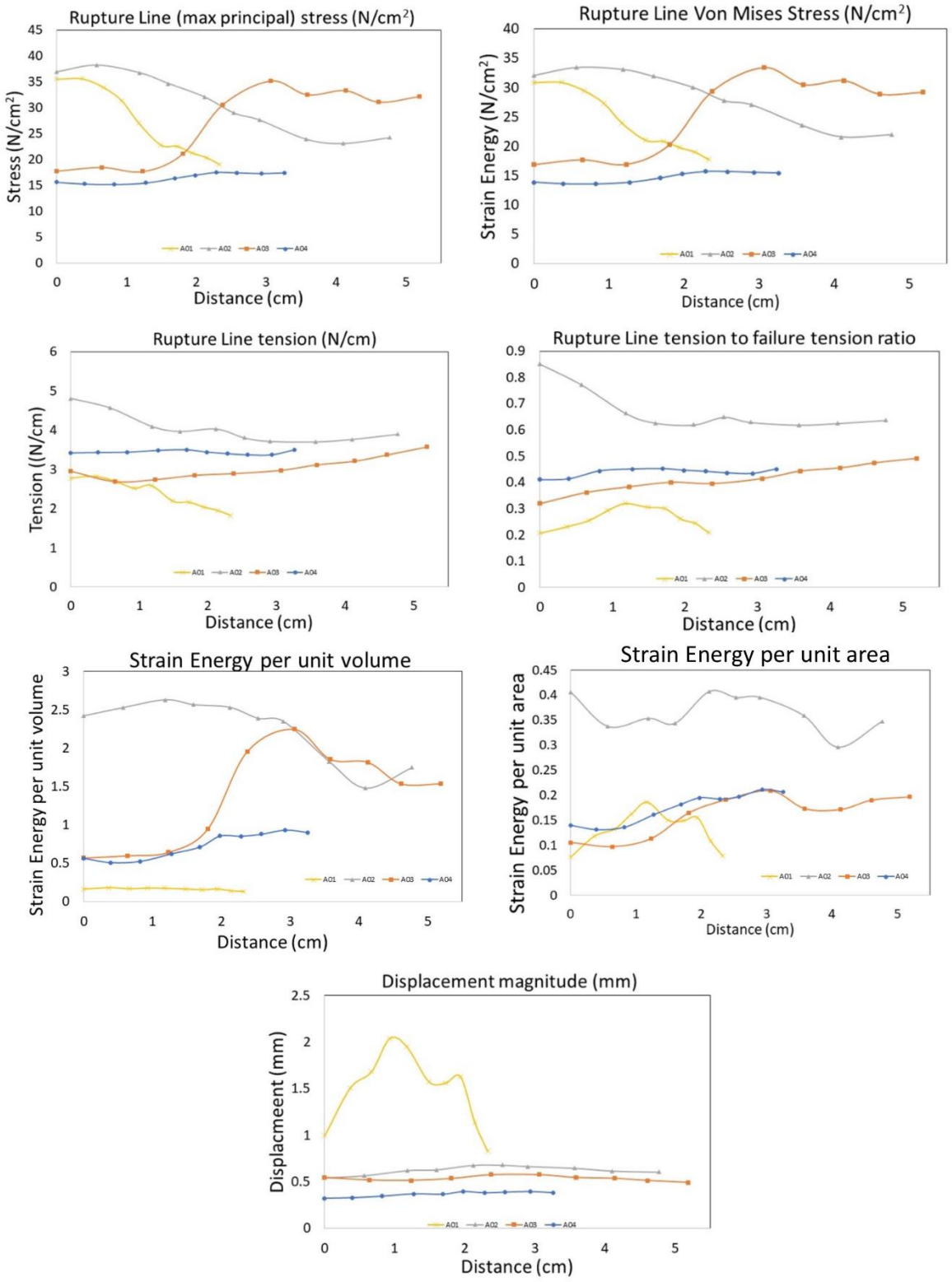

Figure 89: Indices of each rupture line in four ruptured AAA.

4.3 – STRAIN AND DISPLACEMENT INDICES

Displacement magnitude differs than strain due to the simple fact that movement of the aneurysm during simulation occurs. It is unclear whether displacement is due to strain during pressurization or the physical movement of the AAA during simulation. Larger displacement may also be indicative of the summation of smaller displacements in adjacent areas during pressurization.

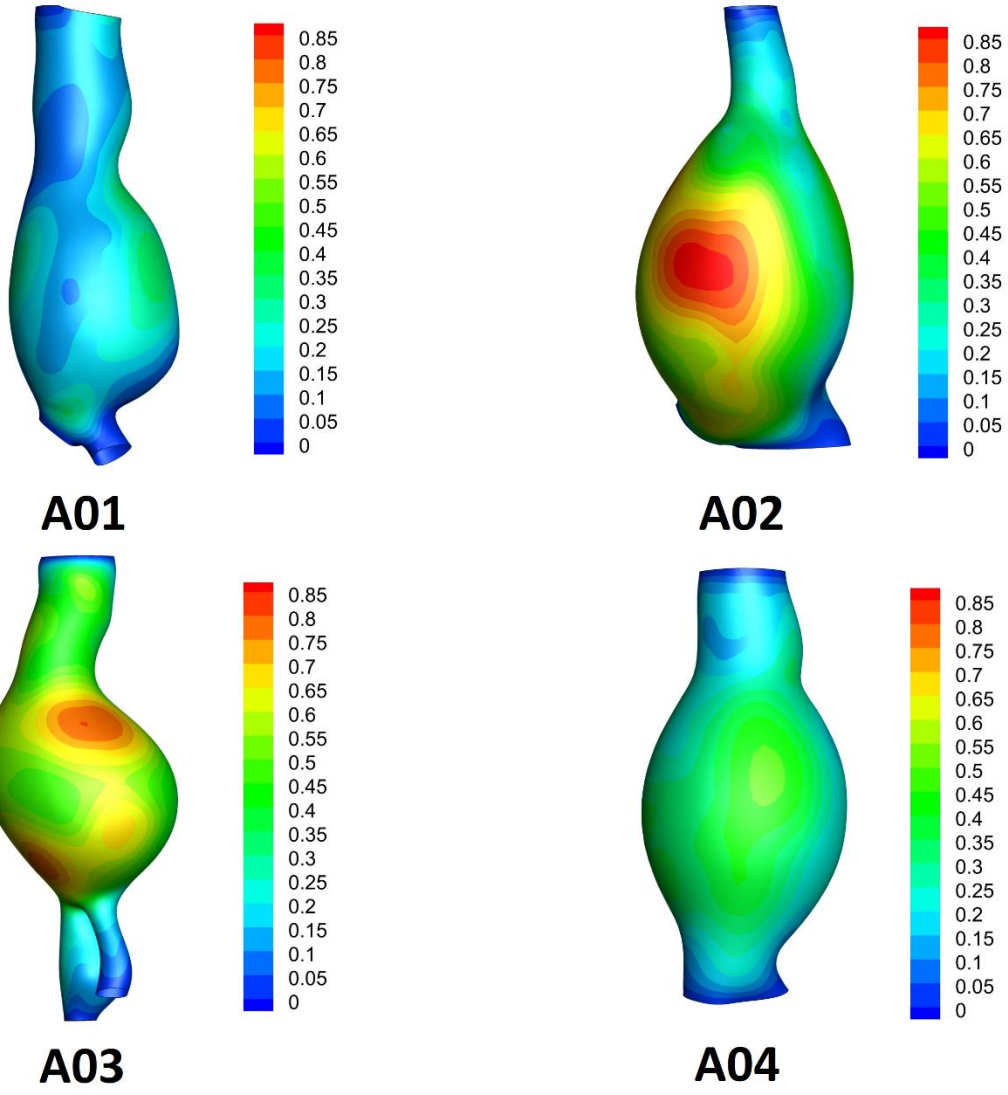

Figure 90: Nodal displacement (magnitude) in each ruptured AAA.

Figure 90, displays the nodal displacements in rupture AAA that are relatively

close to where rupture occurred in AAA. Although the history of displacements were not recorded between each simulation step, the nodal displacements serve as a quantification of AAA movement during simulation.

Figure 91 reports the maximum principal strain for each ruptured AAA. The peak strain values do not correlate with the nodal displacement magnitudes suggesting that large nodal displacements are not indicative of large material strains. It also appears for aneurysm 3, that a band of low strain appears at the

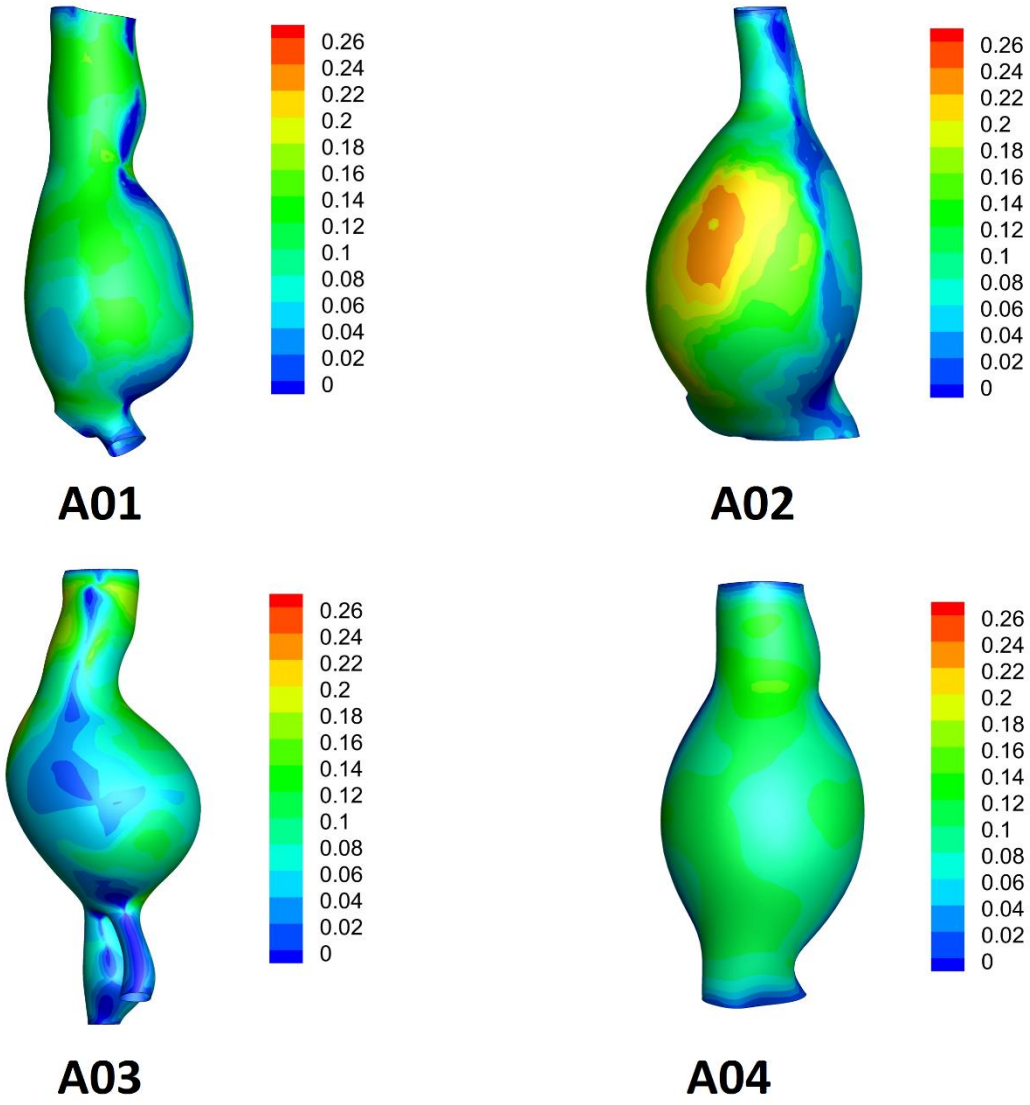

Figure 91: Maximum principal strain in ruptured AAA.

site of rupture. Depending on localized individual material behavior, low strains can translate into higher peak stress or tension values if the material is stiffer and the contrary could be said if the material is less stiff.

Strain energy clarifies to an extent the questions that arise with nodal displacement and maximum principal strain. It is reiterated that the model was materially heterogeneous and each element had the ability to strain based on their interpolated α and β coefficients. Strain energy capture localized loading

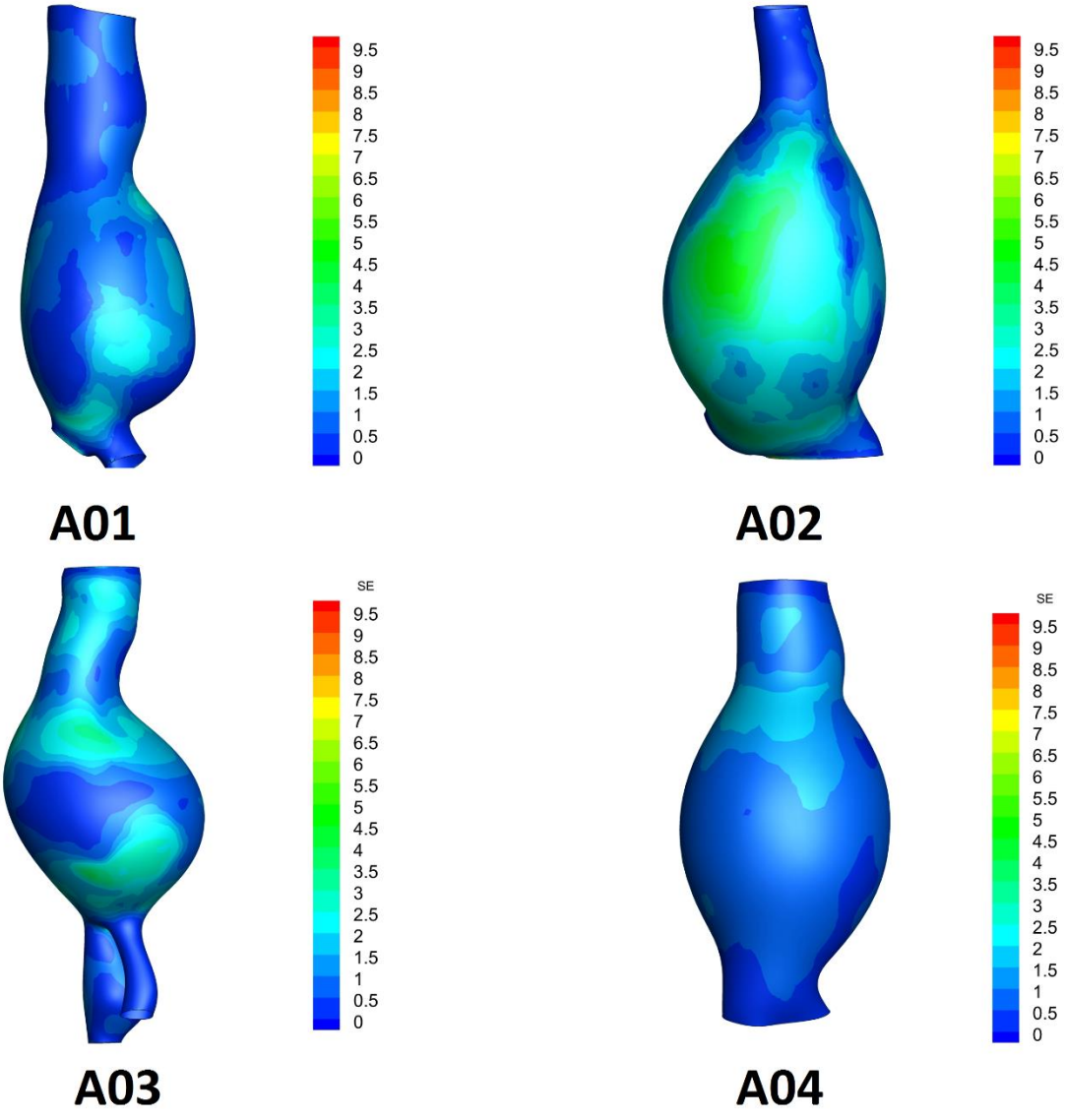

Figure 92: Strain energy per unit volume in four ruptured AAA.

history, but it has not been determined in literature whether a correlation exist between strain energy and AAA rupture. Upon further qualitative observation of the strain energy and rupture site, it can be clearly seen that there are high gradients of strain energy near the rupture site and adjacent areas (Figure 92). It is unclear whether dislocations or stress concentrations form because of these strain energy gradients. These strain energy gradients may also be dependent on their thicknesses as this information is preserved in the calculation of the strain energy per unit volume (Figure 93).

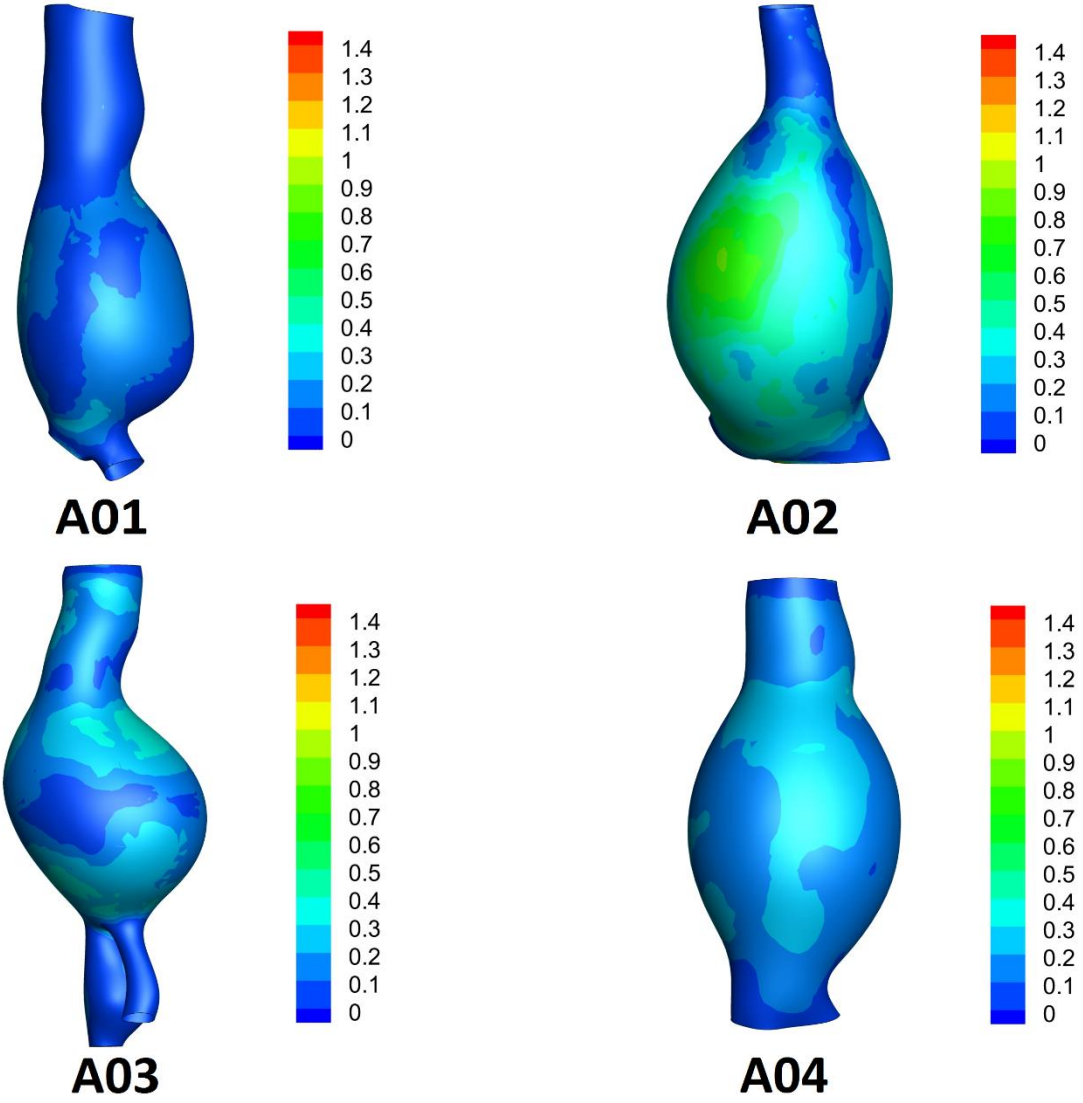

Figure 93: Strain energy per unit surface area of four ruptured AAA.

Strain energy per unit surface area is reported in Figure 93 of rupture AAA. Similar inferences can be made with the strain energy per unit surface area, however removing the thickness slightly smooths out strain energy discontinuities that were presented for strain energy per unit volume (evident in aneurysm 3). Strain energy metrics may play a role in understanding how the material deforms locally for AAA. Additional studies are needed to understand whether strain as whole is driven by the shape of the geometry or through localized material heterogeneity.

4.4 – FAILURE INDICES DISCUSSION AND CONCLUSION

There was no clear metric that represented a causative relationship to the AAA rupture site/line. Although the majority of the indices were higher than the third quartile (intra aneurysm), there was no clear distinction between these indices and the rupture line as the sample size is too small to make any sweeping claims. Qualitative analysis of the principal stress orientation revealed that shape driven features (sphericity) of ruptured AAA created localized poles of randomly oriented principal stresses. It is unclear of where the tear initiated, but the randomly oriented principal stresses may help give insight to the overall path of rupture. Von Mises stress was not rigorously investigated as their stress values were similar to the maximum principal stress and provided redundant conclusions in relation to AAA rupture site. Further investigation is needed to clearly understand whether shape is the primary factor in localized strain deformations or if material heterogeneity determines localized strain. It is also unclear on if the random stress orientations in spherical geometries give rise to

rupture as the longitudinal and circumferential orientations are preferential in tubular vasculatures. Crack propagation studies *in silico* may aid in understanding the path and directionality of rupture whether it is in a single direction proximal to distal, distal to proximal or bi-directional.

With the recent development of the BIT apparatus, it would be beneficial to bridge the gap in the limitation to the earlier computational study that incorporated wall thicknesses and material heterogeneity. Due the scarcity of the material properties tests, the interpolation algorithm may not be representative of localized material properties within an aneurysm. The manual BIT could provide a higher density of measurements to assess stress to failure strength ratio, tension to failure strength ratio and generally understanding the material characteristics of where rupture takes place in post-mortem AAA studies.

CHAPTER 5 – SUMMARY

A novel BIT apparatus (manual and automated) was developed to test fibrous biological soft tissues and non-fibrous molded silicone. It was found that multiaxial failure properties in silicone were no different statistically to that of uniaxial failure properties and that multiaxial rupture in a preferred orientation (circumferential) was linearly correlated to uniaxial extension tests in longitudinally oriented strips. With these findings, it was deduced that the failure properties extracted from an earlier study (Raghavan et al)[6] for ruptured AAA are a reliable metric for material failure properties. However, for oblique multiaxial ruptures it confounded the reliability between this type of rupture and oriented uniaxial extension tests. Without *a priori* directionality of rupture, a correlation between oriented strips may not be reliable.

Additional failure properties and strain information from computational studies were used to assess if these indices were predictive of rupture site location. Although the study was inconclusive in finding causation, the rupture line of each aneurysm had indices ranging between the third quartile and peak values for tension to failure tension ratio, nodal displacement magnitude, strain energy per unit volume and strain energy per unit surface area. Additional studies that introduce localized material strain behavior, principal stress orientation and overall relationship between shape and deformation may greatly improve the understanding of AAA rupture.

REFERENCES

1. Vorp, D. A. Biomechanics of abdominal aortic aneurysm. *J. Biomech.* **40,** 1887–1902 (2007).
2. Darling, R. C., Messina, C. R., Brewster, D. C. & Ottinger, L. W. Autopsy study of unoperated abdominal aortic aneurysms. The case for early resection. *Circulation* **56,** II161-4 (1977).
3. He, C. M. & Roach, M. R. The composition and mechanical properties of abdominal aortic aneurysms. *J. Vasc. Surg.* **20,** 6–13 (1994).
4. Teng, Z. *et al.* Layer- and Direction-Specific Material Properties, Extreme Extensibility and Ultimate Material Strength of Human Abdominal Aorta and Aneurysm: A Uniaxial Extension Study. *Ann. Biomed. Eng.* **43,** 2745–2759 (2015).
5. Humphrey, J. D. & Na, S. Elastodynamics and arterial wall stress. *Ann. Biomed. Eng.* **30,** 509–523 (2002).
6. Raghavan, M. L., Hanaoka, M. M., Kratzberg, J. A., Higuchi, M. de L. & da Silva, E. S. Biomechanical failure properties and microstructural content of ruptured and unruptured abdominal aortic aneurysms. *J. Biomech.* **44,** 2501–2507 (2011).
7. Thubrikar, M. J., Labrosse, M., Robicsek, F., Al-Soudi, J. & Fowler, B. Mechanical properties of abdominal aortic aneurysm wall. *J. Med. Eng. Technol.* **25,** 133–142 (2001).
8. Raghavan, M. L. *et al.* Regional distribution of wall thickness and failure properties of human abdominal aortic aneurysm. *J. Biomech.* **39,** 3010–6 (2006).
9. Raghavan, M. L. & Vorp, D. A. Toward a biomechanical tool to evaluate rupture potential of abdominal aortic aneurysm: Identification of a finite strain constitutive model and evaluation of its applicability. *J. Biomech.* **33,** 475–482 (2000).
10. Vande Geest, J. P., Sacks, M. S. & Vorp, D. A. The effects of aneurysm on the biaxial mechanical behavior of human abdominal aorta. *J. Biomech.* **39,** 1324–1334 (2006).
11. Vorp, D. A., Raghavan, M. L. & Webster, M. W. Mechanical wall stress in abdominal aortic aneurysm: Influence of diameter and asymmetry. *J. Vasc. Surg.* **27,** 632–639 (1998).
12. Holzapfel, G. A. Determination of material models for arterial walls from uniaxial extension tests and histological structure. *J. Theor. Biol.* **238,** 290–302 (2006).
13. Raghavan, M. L., Lin, K. & Ramachandran, M. Planar radial extension for constitutive modeling of anisotropic biological soft tissues. *Int. J. Struct. Chang. Solid* **3,** 23–31 (2011).
14. Milankovic, I. *et al.* Development of the system for abdominal aortic aneurysm mechanical properties research using 'Bubble Inflated' method. *Serbian J. Electr. Eng.* **10,** 415–423 (2013).
15. Cooney, G. M., Moerman, K. M., Takaza, M., Winter, D. C. & Simms, C. K. Uniaxial and biaxial mechanical properties of porcine linea alba. *J. Mech.*

Behav. Biomed. Mater. **41,** 68–82 (2015).
16. Yamada, H., Sakata, N., Wada, H., Tashiro, T. & Tayama, E. Age-related distensibility and histology of the ascending aorta in elderly patients with acute aortic dissection. *J. Biomech.* **48,** 3267–3273 (2015).
17. Zioupos, P. & Barbenel, J. C. Mechanics of native bovine pericardium: I - The multiangular behaviour of strength and stress of the tissue. *Biomaterials* **15,** 366–373 (1994).
18. Dobrin, P. B. Mechanical properties of arterises. *Physiol. Rev.* **58,** 397–460 (1978).
19. Humphrey, J. D. Mechanics of the arterial wall: review and directions. *Crit. Rev. Biomed. Eng.* **23,** 1–162 (1995).
20. Weisbecker, H., Viertler, C., Pierce, D. M. & Holzapfel, G. A. The role of elastin and collagen in the softening behavior of the human thoracic aortic media. *J. Biomech.* **46,** 1859–1865 (2013).
21. Raghavan, M. L., Webster, M. W. & Vorp, D. A. Ex vivo biomechanical behavior of abdominal aortic aneurysm: assessment using a new mathematical model. *Ann Biomed Eng* **24,** 573–582 (1996).
22. Reeps, C. *et al.* Measuring and modeling patient-specific distributions of material properties in abdominal aortic aneurysm wall. *Biomech. Model. Mechanobiol.* **12,** 717–733 (2013).
23. Vande Geest, J. P., Sacks, M. S. & Vorp, D. A. A planar biaxial constitutive relation for the luminal layer of intra-luminal thrombus in abdominal aortic aneurysms. *J. Biomech.* **39,** 2347–2354 (2006).
24. Tong, J., Cohnert, T., Regitnig, P. & Holzapfel, G. A. Effects of age on the elastic properties of the intraluminal thrombus and the thrombus-covered wall in abdominal aortic aneurysms: Biaxial extension behaviour and material modelling. *Eur. J. Vasc. Endovasc. Surg.* **42,** 207–219 (2011).
25. Liao, J., Yang, L., Grashow, J. & Sacks, M. S. Molecular orientation of collagen in intact planar connective tissues under biaxial stretch. *Acta Biomater.* **1,** 45–54 (2005).
26. Debes, J. C. & Fung, Y. C. Effect of temperature on the biaxial mechanics of excised lung parenchyma of the dog. *J. Appl. Physiol.* **73,** 1171–80 (1992).
27. Sacks, M. S. Incorporation of experimentally-derived fiber orientation into a structural constitutive model for planar collagenous tissues. *J. Biomech. Eng.* **125,** 280–7 (2003).
28. Li, Y., Nemes, J. A. & Derdouri, A. A. Membrane inflation of polymeric materials: Experiments and finite element simulations. *Polym. Eng. Sci.* **41,** 1399–1412 (2001).
29. Slifka, A. J., Drexler, E. S., Wright, J. E. & Shandas, R. Bubble-test method for synthetic and bovine vascular material. *J. Biomech.* **39,** 1939–1942 (2006).
30. Hsu, F. P. K. Material Identification Using Membrane Inflation Tests: Applications to Saccular Aneurysms. (University of Maryland, 1993). doi:10.16953/deusbed.74839
31. Charalambides, M. N., Wanigasooriya, L., Williams, G. J., Goh, S. M. &

Chakrabarti, S. Large deformation extensional rheology of bread dough. *Rheol. Acta* **46,** 239–248 (2006).
32. Brunon, A., Bruy??re-Garnier, K. & Coret, M. Characterization of the nonlinear behaviour and the failure of human liver capsule through inflation tests. *J. Mech. Behav. Biomed. Mater.* **4,** 1572–1581 (2011).
33. Davis, F. M., Luo, Y., Avril, S., Duprey, A. & Lu, J. Pointwise characterization of the elastic properties of planar soft tissues: application to ascending thoracic aneurysms. *Biomech. Model. Mechanobiol.* **14,** 967–978 (2015).
34. Bischoff, J. E., Drexler, E. S., Slifka, A. J. & McCowan, C. N. Quantifying nonlinear anisotropic elastic material properties of biological tissue by use of membrane inflation. *Comput. Methods Biomech. Biomed. Engin.* **12,** 353–369 (2009).
35. Mohan, D. H. & Melvin, J. W. Failure Properties of Passive Human Aortic Tissue - Uniaxial Tension Tests. *J. Biomech.* **15,** 887–902 (1982).
36. Drexler, E. S. *et al.* An experimental method for measuring mechanical properties of rat pulmonary arteries verified with latex. *J. Res. Natl. Inst. Stand. Technol.* **108,** 183 (2003).
37. Duprey, A., Trabelsi, O., Vola, M., Favre, J. P. & Avril, S. Biaxial rupture properties of ascending thoracic aortic aneurysms. *Acta Biomater.* **42,** 273–285 (2016).
38. Charalambides, M. N., Wanigasooriya, L., Williams, G. J. & Chakrabarti, S. Biaxial deformation of dough using the bubble inflation technique. I. Experimental. *Rheol. Acta* **41,** 532–540 (2002).
39. Raghavan, M. L., Fillinger, M. F., Marra, S. P., Naegelein, B. P. & Kennedy, F. E. Automated Methodology for Determination of Stress Distribution in Human Abdominal Aortic Aneurysm. *J. Biomech. Eng.* **127,** 868 (2005).
40. Fillinger, M. F., Marra, S. P., Raghavan, M. L. & Kennedy, F. E. Prediction of rupture risk in abdominal aortic aneurysm during observation: Wall stress versus diameter. *J. Vasc. Surg.* **37,** 724–732 (2003).
41. Truijers, M. *et al.* Wall Stress Analysis in Small Asymptomatic, Symptomatic and Ruptured Abdominal Aortic Aneurysms. *Eur. J. Vasc. Endovasc. Surg.* **33,** 401–407 (2007).
42. Fillinger, M. F., Raghavan, M. L., Marra, S. P., Cronenwett, J. L. & Kennedy, F. E. In vivo analysis of mechanical wall stress and abdominal aortic aneurysm rupture risk. *J. Vasc. Surg.* **36,** 589–597 (2002).
43. Polzer, S. & Gasser, T. C. Biomechanical rupture risk assessment of abdominal aortic aneurysms based on a novel probabilistic rupture risk index. *J. R. Soc. Interface* **12,** 20150852 (2015).
44. Khosla, S. *et al.* Meta-analysis of peak wall stress in ruptured, symptomatic and intact abdominal aortic aneurysms. *Br. J. Surg.* **101,** 1350–1357 (2014).
45. Maier, A. *et al.* A comparison of diameter, wall stress, and rupture potential index for abdominal aortic aneurysm rupture risk prediction. *Ann. Biomed. Eng.* **38,** 3124–3134 (2010).

46. Doyle, B. J. *et al.* An experimental and numerical comparison of the rupture locations of an abdominal aortic aneurysm. *J. Endovasc. Ther.* **16,** 322–335 (2009).
47. McGloughlin, T. M. & Doyle, B. J. New approaches to abdominal aortic aneurysm rupture risk assessment: Engineering insights with clinical gain. *Arterioscler. Thromb. Vasc. Biol.* **30,** 1687–1694 (2010).
48. Vande Geest, J. P. Towards an Improved Rupture Potential Index for Abdominal Aaneurysms: Anisotropic Constitutive Modeling and NonInvasive Wall Strength Estimation. 317 (2005).
49. Vande Geest, J. P., Di Martino, E. S., Bohra, A., Makaroun, M. S. & Vorp, D. A. A biomechanics-based rupture potential index for abdominal aortic aneurysm risk assessment: Demonstrative application. *Ann. N. Y. Acad. Sci.* **1085,** 11–21 (2006).
50. Martufi, G., Satriano, A., Moore, R. D., Vorp, D. A. & Di Martino, E. S. Local Quantification of Wall Thickness and Intraluminal Thrombus Offer Insight into the Mechanical Properties of the Aneurysmal Aorta. *Ann. Biomed. Eng.* **43,** 1759–1771 (2015).
51. Wang, D. H. J., Makaroun, M. S., Webster, M. W. & Vorp, D. A. Effect of intraluminal thrombus on wall stress in patient-specific models of abdominal aortic aneurysm. *Journal of Vascular Surgery* **36,** 598–604 (2002).
52. Georgakarakos, E. *et al.* The Role of Geometric Parameters in the Prediction of Abdominal Aortic Aneurysm Wall Stress. *Eur. J. Vasc. Endovasc. Surg.* **39,** 42–48 (2010).
53. Polzer, S., Gasser, C., Markert, B., Bursa, J. & Skacel, P. Impact of poroelasticity of intraluminal thrombus on wall stress of abdominal aortic aneurysms. *Biomed. Eng. Online* **11,** 62 (2012).
54. Martufi, G., Di Martino, E. S., Amon, C. H., Muluk, S. C. & Finol, E. A. Three-Dimensional Geometrical Characterization of Abdominal Aortic Aneurysms: Image-Based Wall Thickness Distribution. *J. Biomech. Eng.* **131,** 61015 (2009).
55. Roweis, S. Levenberg-Marquardt Optimization. *Notes, Univ. Toronto* (1996).
56. Lampton, M. Damping-undamping strategies for the Levenberg-Marquardt nonlinear least-squares method. *Comput. Phys.* **11,** 110–115 (1997).
57. Hong, Q. H., Baumberg, A. M. & Lyons, A. R. Image Processing Apparatus. (2004).
58. Disease Control, C. Aortic Aneurysm Fact Sheet. 1–4
59. Brain Anuerysm Basics That Could Save Your Life. *Brain Aneurysm Found.* (2014).
60. Venkatasubramaniam, A. K. *et al.* A comparative study of aortic wall stress using finite element analysis for ruptured and non-ruptured abdominal aortic aneurysms. *Eur. J. Vasc. Endovasc. Surg.* **28,** 168–176 (2004).
61. Tierney, Á. P., Callanan, A. & McGloughlin, T. M. Use of Regional Mechanical Properties of Abdominal Aortic Aneurysms to Advance Finite Element Modeling of Rupture Risk. *J. Endovasc. Ther.* **19,** 100–114

(2012).
62. Chung, T. K.-J. Heterogeneous Finite Element Stress Analysis of Abdominal Aortic Aneurysms: Comparison Between Ruptured and Unruptured Lesions. *University of Iowa Master's Thesis* (University of Iowa, 2013). doi:10.1017/CBO9781107415324.004
63. Tong, J., Schriefl, A. J., Cohnert, T. & Holzapfel, G. A. Gender differences in biomechanical properties, thrombus age, mass fraction and clinical factors of abdominal aortic aneurysms. *Eur. J. Vasc. Endovasc. Surg.* **45,** 364–372 (2013).
64. Voycheck, C. A., Luu, K., McMahon, P. J. & Debski, R. E. Collagen fiber alignment and maximum principal strain in the glenohumeral capsule predict location of failure during uniaxial extension. *Biomech. Model. Mechanobiol.* **13,** 379–385 (2014).
65. Raghupathy, R., Witzenburg, C., Lake, S. P., Sander, E. a. & Barocas, V. H. Identification of Regional Mechanical Anisotropy in Soft Tissue Analogs. *J. Biomech. Eng.* **133,** 91011 (2011).
66. Koff, W. & Gustafson, P. 3D Printing and the Future of Manufacturing. *CSC Lead. Edge Forum* 1–11 (2012). doi:10.1211/PJ.2015.20068625
67. Yao, X. & Lin, Y. Emerging manufacturing paradigm shifts for the incoming industrial revolution. *Int. J. Adv. Manuf. Technol.* **85,** 1665–1676 (2016).
68. Chilson, L. The Difference Between ABS and PLA for 3D Printing. *ProtoParadigm Blog* 7–9 (2013).
69. Van der Blom, N. Valve connector. (2003).
70. Crosby, P. Get to know lasers and their roles in plastics. *Plastics Technology* 4 (2002).
71. Beauregard, B. Arduino PID Library. (2009).
72. Ibrahim, A. M. Balancing of a Ball on Beam using Arduino as a PID controller. (2014). Available at: http://mechatronicstutorials.blogspot.com/2014/07/balancing-of-ball-on-beam-using-arduino.html. (Accessed: 1st December 2017)
73. Raghavan, M. L. *et al.* Aneurysm Shape Reconstruction from Biplane Angiograms in the ISUIA Collection. *Transl. Stroke Res.* **5,** 252–259 (2014).
74. Sederberg, T. W. & Greenwood, E. Shape Blending of 2-D Piecewise Curves. *Math. Methods CAGDIII* 1–10 (1995).
75. Bischoff, J. E. Constitutive modeling and testing of biological soft tissue. 175 (2001).
76. Lu, J., Zhou, X. & Raghavan, M. L. Inverse elastostatic stress analysis in pre-deformed biological structures: Demonstration using abdominal aortic aneurysms. *J. Biomech.* **40,** 693–696 (2007).
77. Heng, M. S. *et al.* Peak wall stress measurement in elective and acute abdominal aortic aneurysms. *J. Vasc. Surg.* **47,** 17–22 (2008).
78. Doyle, B. J., Callanan, A., Grace, P. A. & Kavanagh, E. On the influence of patient-specific material properties in computational simulations: A case study of a large ruptured abdominal aortic aneurysmOn the influence of patient-specific material properties in computational simulations: A case

study of a large. *Int. j. numer. method. biomed. eng.* **26,** 807–827 (2013).
79. Raut, S. S., Chandra, S., Shum, J. & Finol, E. A. The Role of Geometric and Biomechanical Factors in Abdominal Aortic Aneurysm Rupture Risk Assessment. *Ann Biomed Eng* **41,** 1459–1477 (2013).
80. Gasser, T. C. Biomechanical Rupture Risk Assessment: A Consistent and Objective Decision-Making Tool for Abdominal Aortic Aneurysm Patients. *Aorta (Stamford, Conn.)* **4,** 42–60 (2016).
81. Doyle, B. J., Callanan, A., Walsh, M. T., Grace, P. A. & Mcgloughlin, T. M. A Finite Element Analysis Rupture Index (FEARI) as an Additional Tool for Abdominal Aortic Aneurysm Rupture Prediction. *Vasc. Dis. Prev.* **6,** 114–121 (2009).
82. Raghavan, M. L. Wall thickness is a red herring in the study of aneurysm tissue mechanics. in *Proceedings of 5th International Conference on Computational and Mathematical Biomedical Engineering* (2017).

APPENDIX I - RUPTURE SITES OF BOVINE BIT EXPERIMENTS

Experiment 1: 2.56 mm with circumferential rupture (lumen, adventitia)

Experiment 2: 2.81 mm with circumferential rupture (lumen, adventitia)

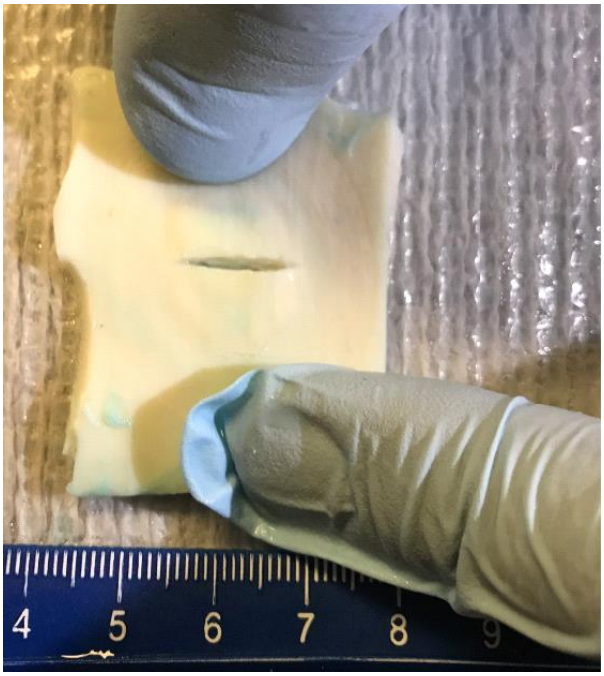

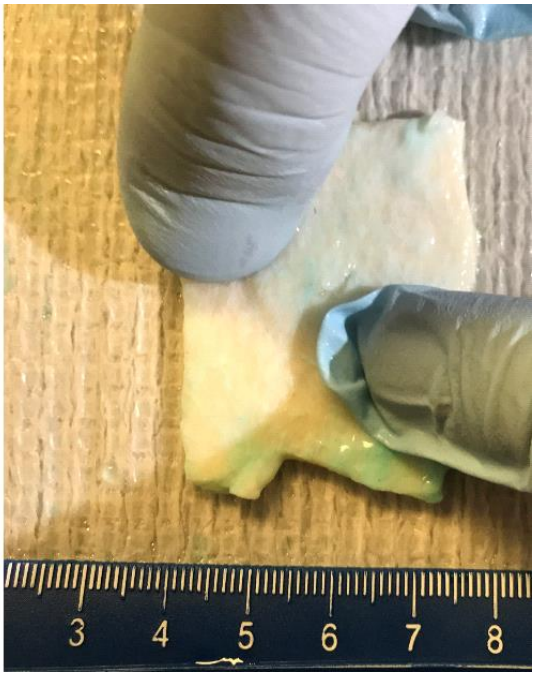

Experiment 3: 1.69 mm with circumferential rupture (lumen, adventitia)

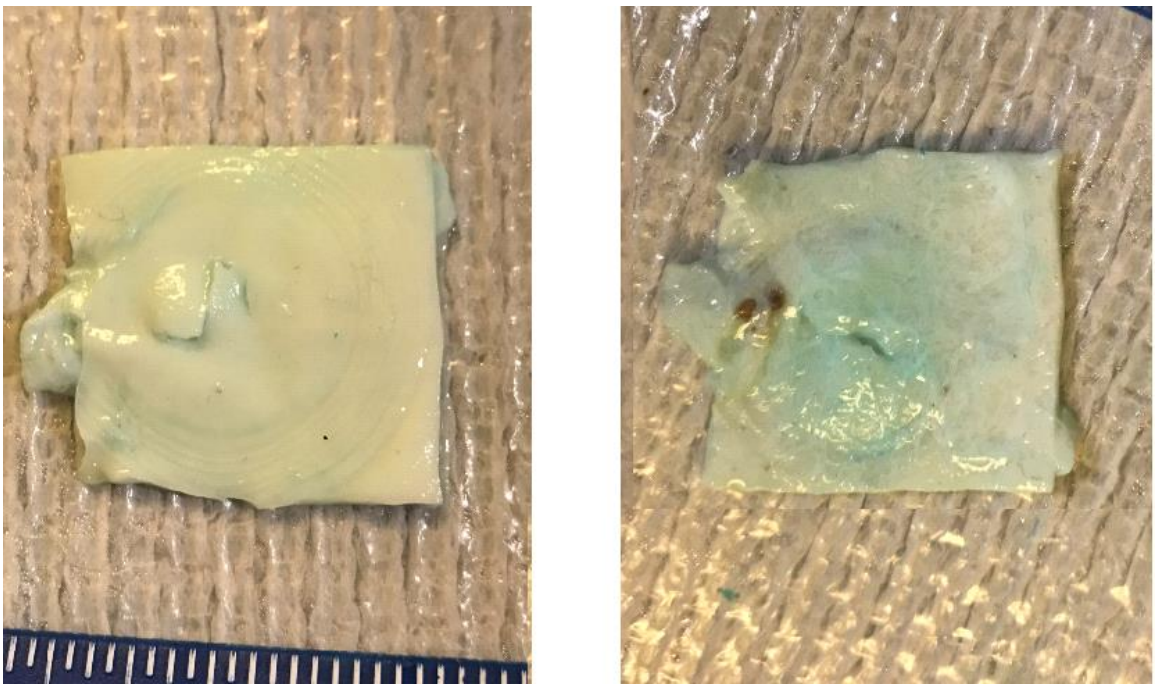

Experiment 4: 2.26 mm with circumferential rupture (lumen, adventitia)

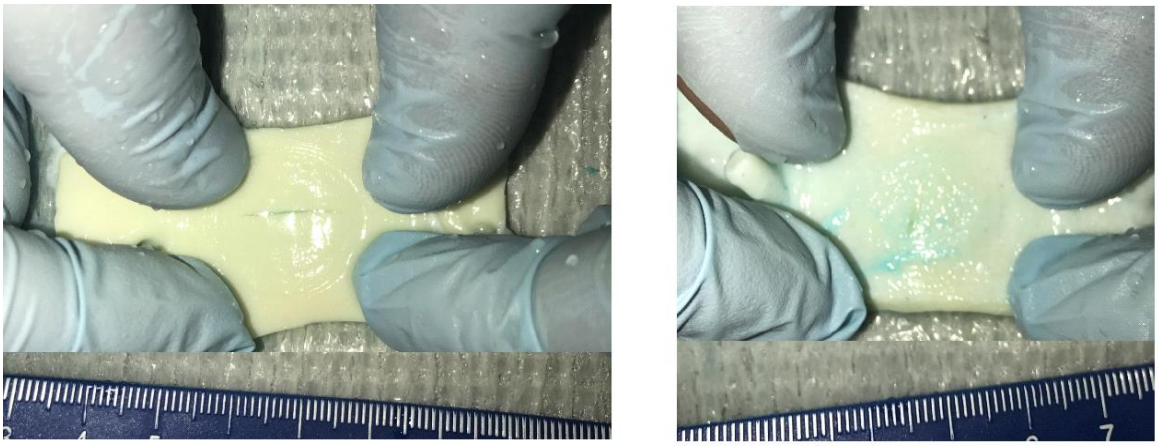

Experiment 5: 3.49 mm with circumferential rupture (lumen, adventitia)

Experiment 6: 3.94 mm with circumferential rupture (lumen, adventitia)

Experiment 7: 4.71 mm with circumferential rupture (lumen, adventitia)

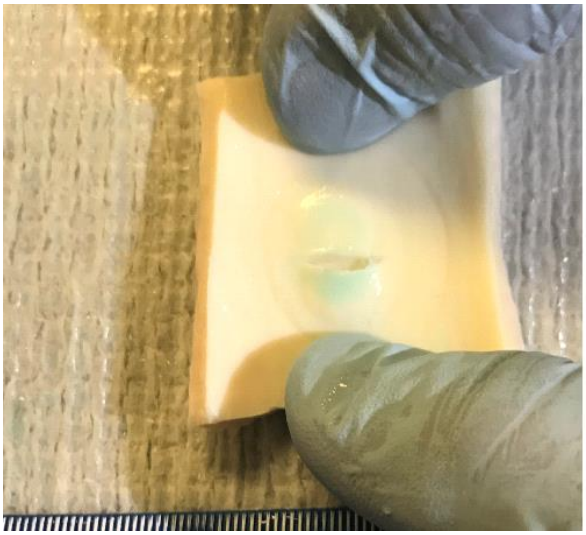

Experiment 8: 4.53 mm with circumferential rupture (lumen, adventitia)

Experiment 9: 5.17 mm with circumferential rupture (lumen, adventitia)

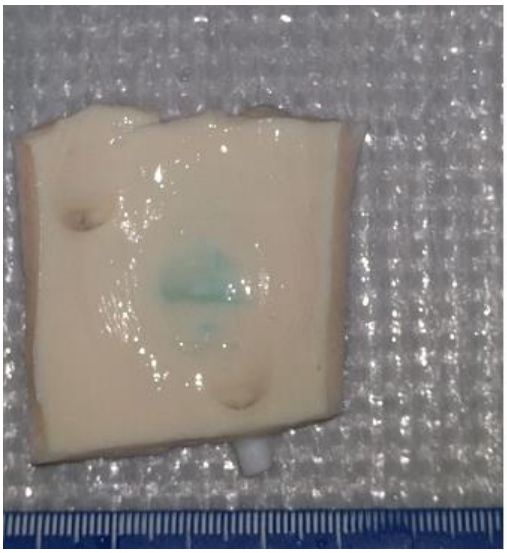
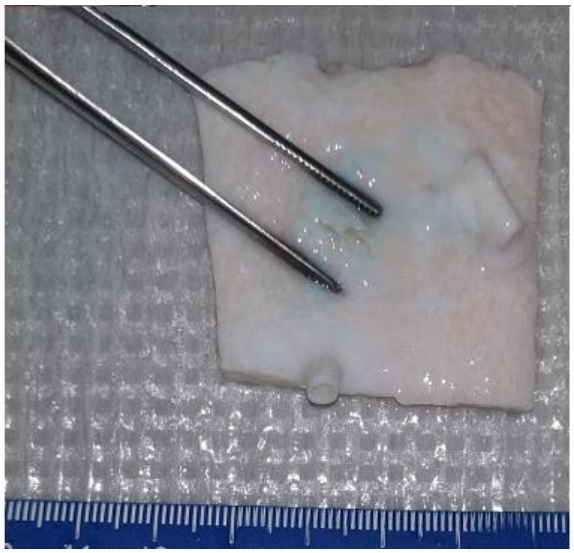

Experiment 10: 5.10 mm with circumferential rupture (lumen, adventitia)


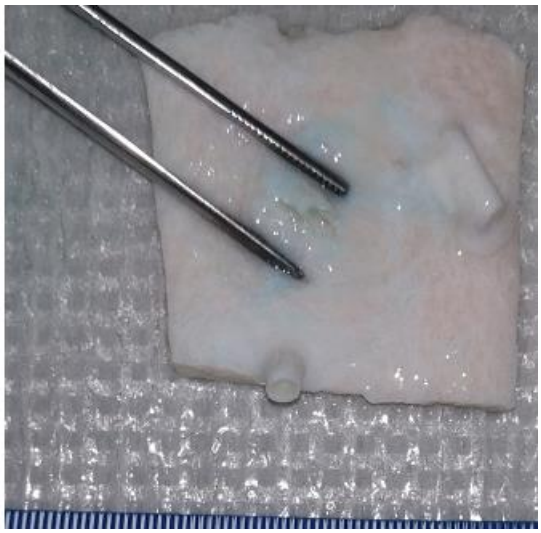

Experiment 11: 6.00 mm with circumferential rupture (lumen, adventitia)

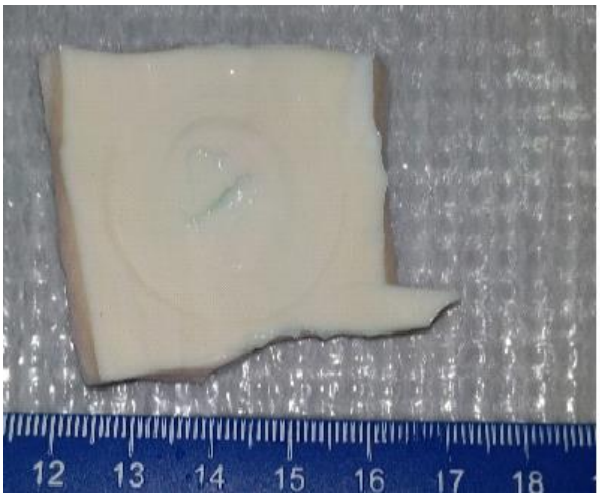

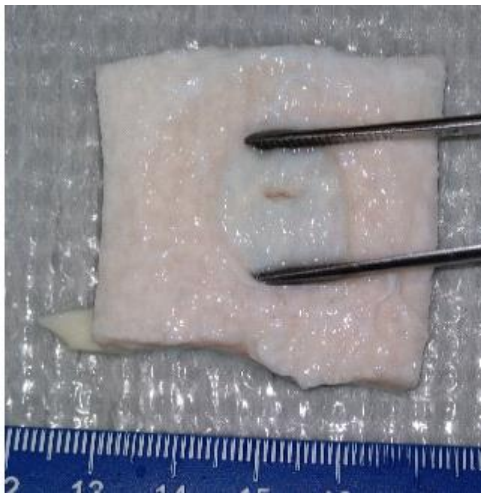

Experiment 12: 5.89 mm with circumferential rupture (lumen, adventitia)

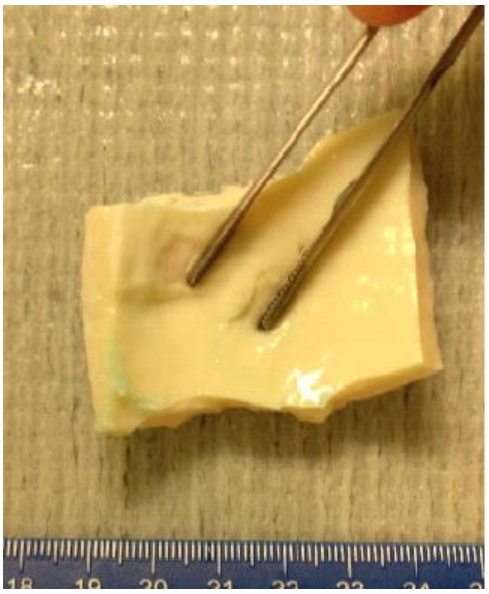

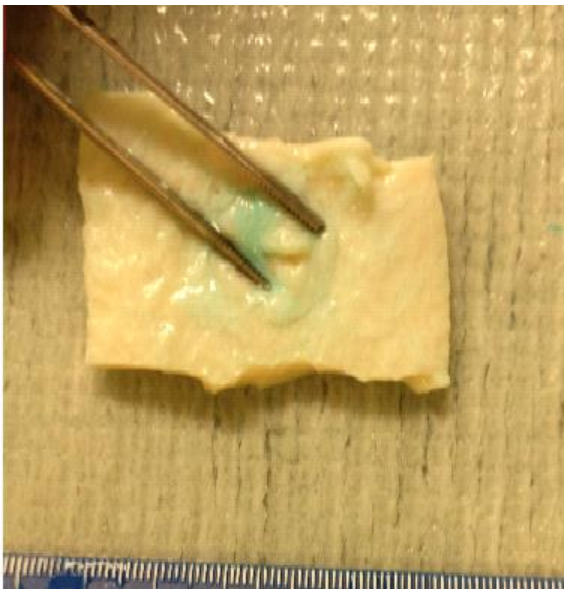

APPENDIX II – ORIENTATION OF MAX AND MID PRINCIPAL STRESSES

Aneurysm 1: Rupture site, maximum and middle principal stresses.

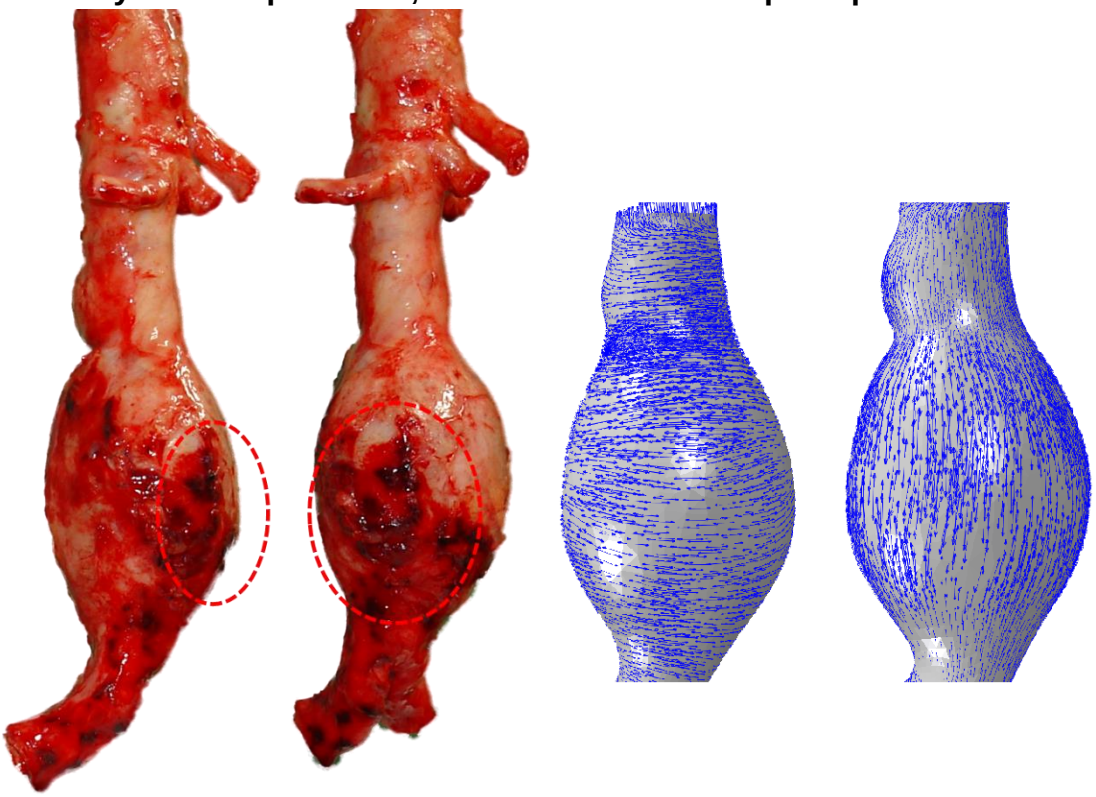

Aneurysm 2: Rupture site, maximum and middle principal stresses.

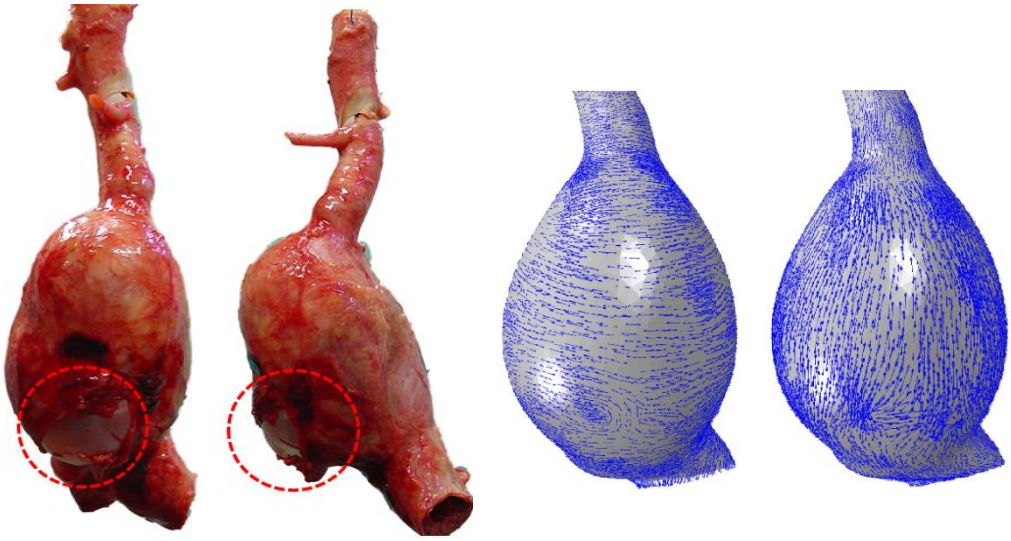

Aneurysm 4: Rupture site, maximum and middle principal stresses.

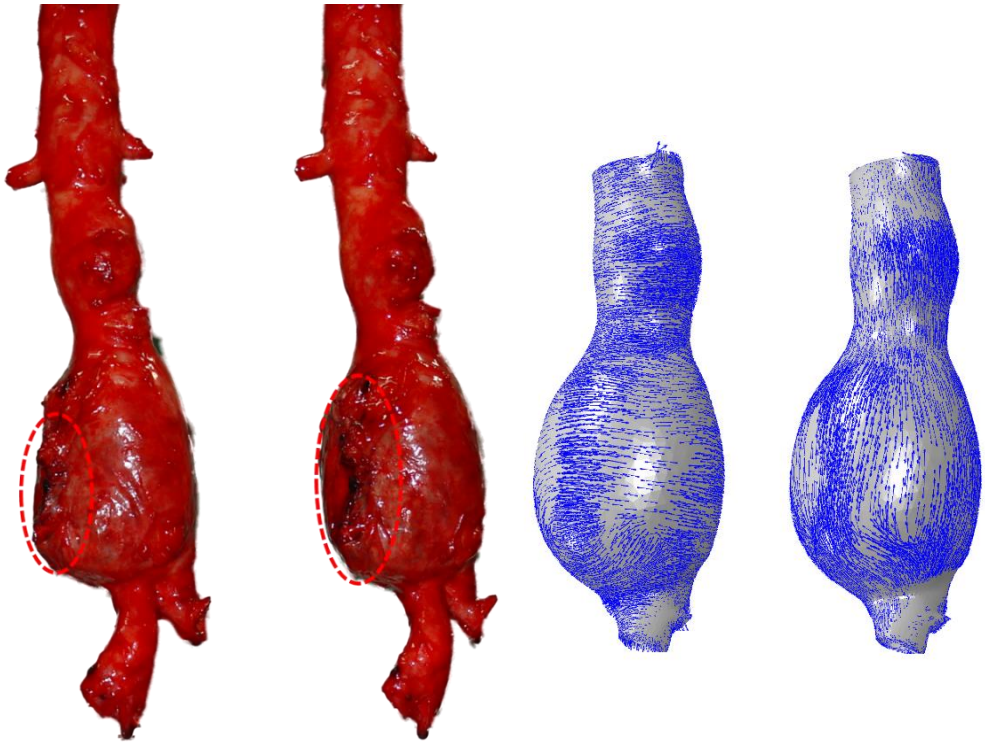

APPENDIX III - PAPER IN REVISION TO THE JOURNAL OF BIOMECHANICS:

Does elevated wall tension cause aortic aneurysm rupture? Investigation using a heterogeneous model

[1]Chung, Timothy K., [2]da Silva, Erasmo S., [1]Raghavan, Suresh M.L.
[1]Department of Biomedical Engineering, University of Iowa, Iowa City, IA USA
[2]Department of Vascular Surgery, University of São Paulo, São Paulo, Brazil.

ABSTRACT

Objective. To investigate whether peak wall tension in abdominal aortic aneurysm occurs at the site of rupture to test for a causative relationship.

Methods. Four ruptured and nine unruptured AAA were harvested whole from cadavers, followed by regional measurements of wall thickness, elastic parameters and failure tension. Finite element models were developed with subject-specific load-free AAA morphology and heterogeneous properties interpolated using a geodesic distance weighted approach from the measurements. The wall tension under uniform pressure and tension to failure tension ratio as an index of susceptibility to rupture were computed. As a secondary aim, the peak wall tension using this heterogeneous model approach was compared to the traditional homogeneous model approach in order to evaluate the reliability of the latter.

Results. The average peak wall tension in the ruptured group was 43% higher than in the unruptured group without statistical significance even though it was 54% larger in diameter. The site of peak wall tension was in the vicinity of the site of rupture in two ruptured AAA. The peak tension did not breach failure tension at the rupture site in any of the AAA. The traditional population-wide

homogeneous model approach overestimated peak wall tension by just 3% compared to the subject-specific heterogeneous model approach.

Conclusion. We failed to find adequate evidence of a causative relationship between peak wall tension and AAA rupture. The findings are not conclusive owing to study limitations such as ignoring intraluminal thrombus, sparse distribution of specimens procured and small study population.

INTRODUCTION

Abdominal aortic aneurysms (AAA) that go onto rupture under observation or present in the clinic ruptured have been shown to have higher peak wall stress resultant compared with those that stay unruptured under observation or present unruptured [1,40–42,45,49,60,77–80]. It is important to recognize that they only point to correlation and not causation in the relationship between peak wall stress and AAA rupture. It is plausible for elevated peak wall stress to correlate to rupture risk for reasons of study design bias (e.g., the ruptured group could be larger than the unruptured group) and still not cause it. We submit that, if elevated stress is the sole cause of rupture, then not only would ruptured AAA have elevated peak wall stress, but the locations of peak wall stress and rupture would have to match as well. Doyle et al., (2009) found that the location of rupture site matched numerical predictions in experimental silicone models, but does this hold up in human AAA? Through a study of AAA harvested whole during necropsy [6], we have for the first time, collected the experimental and imaging data necessary for rigorously testing for a causative relationship. This is the first study where the site and extent of rupture was precisely identified *ex vivo*.

Further, the computational methodology avoided many assumptions common to AAA stress analyses by starting with a load-free configuration, patient-specific spatially varying wall thickness, elastic parameters and permitted comparison to patient-specific measured failure properties. A secondary aim of the study is to compare AAA wall stresses estimated in this study with one using the traditional approach with a homogenous population-averaged elastic parameters and pre-deformed *in vivo* geometry in order to assess the reliability of noninvasive patient-specific wall stress analysis.

METHODS

Specimen procurement and measurements

Four ruptured and nine unruptured infrarenal aortic aneurysms that were harvested whole from human cadavers submitted to necropsy for the elucidation of the cause of death at the Service for Confirmation of Deaths at the University of São Paulo School of Medicine. The study was approved by the institutional review board (Ethical Committee of Clinics Hospital, São Paulo University Medical School #849/99). The whole AAA specimens were hung from hooks, mildly inflated with a compliant balloon to < 5 mmHg to remove any surface collapse while using negligible pressure and digitally photographed from 360^0 – 36 photographs with a plain green background (Figure 1; left panel) taken all around the cranio-caudal axis of the aneurysm in 10^o increments to capture the 3D surface shape. Wall thickness was measured at an average of 35 sites all around each AAA. An average of six rectangular strips were cut from each AAA and subjected to uniaxial extension until failure.

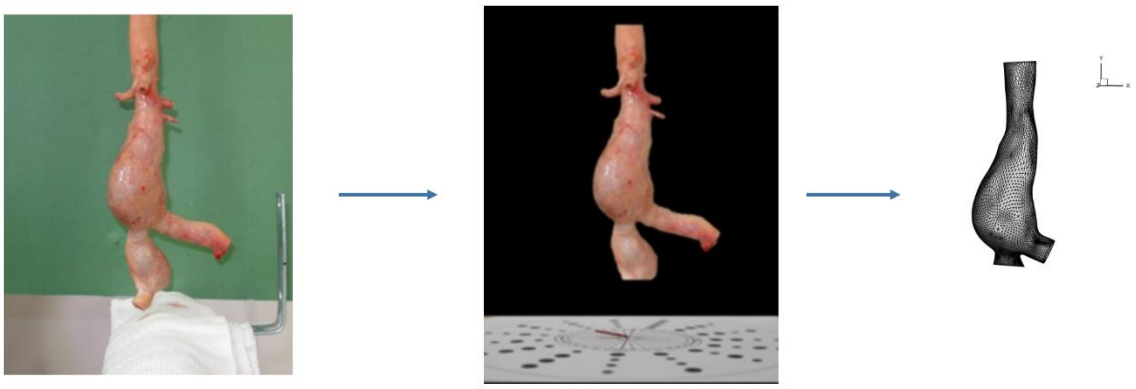

Fig 1: Zero pressure image and shape from silhouette reconstruction

The sites of wall thickness measurements and rectangular strips were marked on photographs. Additional details on specimen procurement, preparation, wall thickness measurements, mechanical testing and histological analyses have been reported earlier [6]. Specifically, failure tension and failure stress were determined. For elastic properties, α and β, the parameters of the finite elastic isotropic incompressible two-parameter model reported by Raghavan and Vorp, 2000 were estimated using the Levenberg – Marquardt damped least-squared method from the stress-strain curve for each strip with the constraint that α has to be greater than 3 N/sq.cm.

Geometric model construction

For a given AAA, the 36 images were segmented using an in house batch processing script in MATLAB. This was straightforward owing to the green background in the photographs. A calibration mat was digitally inserted based on known camera angles and parameters during photography. Voxel carving, a shape from silhouette technique, was performed in 3DSOM (CDSL Limited,

London, England; Hong et al., 2004) to reconstruct a polygonal representation of 3D aneurysm wall surface geometry as shown in Figure 1. The 3D reconstruction method was verified by reconstructing a hypothetical cylinder from digital 360 degree images of the cylinder. The 3D surface mesh and texture map was exported into Meshlab (Visual Computing Laboratory, Pisa, Italy) and a surface preserving Laplacian smoothing was performed (Figure 1). Texture maps from the photographs were projected back on to the mesh surface to recreate a 3D model of the AAA that visually matches with the photographs. Locations of wall thickness measurements and center-points of mechanical test strips were directly mapped onto specific nodes on the finite element model (Figure 2).

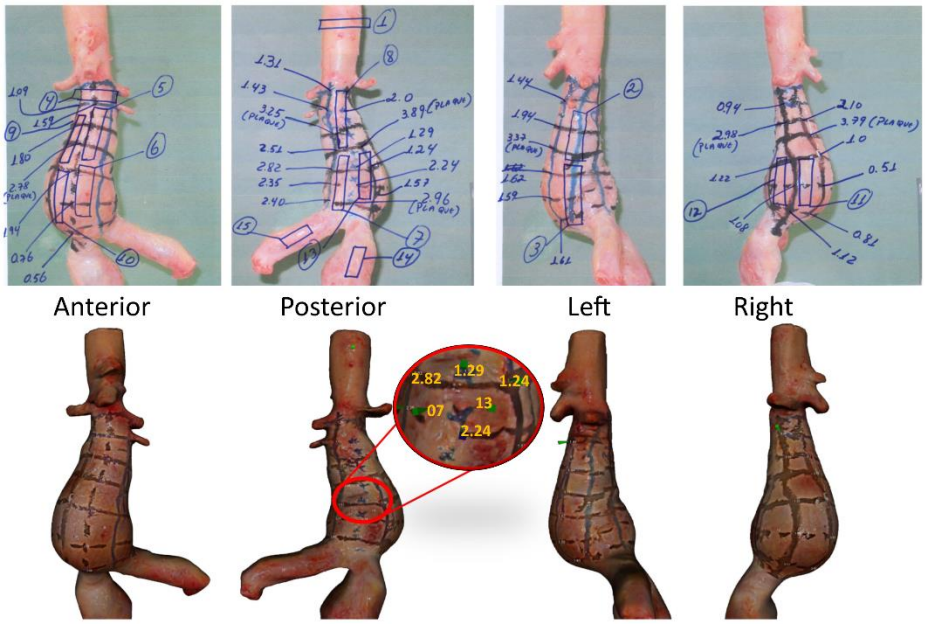

Fig 2: AP left and right locations of wall thicknesses and material properties.

Interpolation of properties

While the regional measurements were obtained at multiple sites, it still constitutes a sparse collection of measurement sites compared to the large number of vertices in the computational model – especially for the mechanical properties. A geodesic distance nearest neighbor nonlinear weighted scattered data interpolation algorithm was developed to interpolate any given scalar value (thickness and elastic properties) from the set of known locations (measurement sites) to the set of unknown locations (all other nodes) on the mesh surface. The premise for interpolation is that the scalar value at an arbitrary node be dependent on the scalar value of the measured sites in its neighborhood weighted inversely by its geodesic distance (shortest path on the surface) from those sites. First, the geodesic distances from each of the measurement sites to all of the nodes in the surface mesh were computed. Now let us consider a node i, for which the interpolated thickness t_i needs to be determined. Its nearest m neighbors with measured thicknesses $t_{i,1}$, $t_{i,2}$, …and $t_{i,m}$, are at geodesic distances $d_{i,1}$, $d_{i,2}$, …and $d_{i,m}$ from node i (nearest to farthest). From this, the normalized geodesic distances may be written as,

$$g_{i,j} = \frac{d_{i,j}}{\sum_{k=1}^{m} d_{i,k}} \qquad (1)$$

The interpolated thickness of i^{th} node is defined as

$$t_i = \sum_{j=1}^{m} w_{i,j}\, t_{i,j} \qquad (2)$$

where, $t_{i,j}$: $1 \leq j \leq m$ are the thicknesses of the *m* nearest neighboring nodes with measured values (*j*=1 represents the nearest neighbor to node *i*; *j*=2, the next nearest; and so on), and

$$w_{i,j} = \begin{cases} (1 - g_{i,j}) & j = 1 \\ (1 - g_{i,j}) \prod_{k=1}^{j-1} g_{i,k} & 1 < j < m \\ \prod_{k=1}^{j-1} g_{i,k} & j = m \end{cases} \quad (3)$$

It can be shown that the sum of weights in Eq. 3, $\sum_{j=1}^{m} w_{i,j} = 1$

Eq. 3 ensures that the nearest neighbor is weighted the most followed by the next nearest neighbor and so on with a nonlinear drop in weights. In this study, *m* = 4 (that is, the interpolation was performed using four nearest neighbors). Therefore, Eq. 3 would reduce to,

$$\begin{aligned} w_{i,1} &= 1 - g_{i,1} \\ w_{i,2} &= (1 - g_{i,2}) g_{i,1} \\ w_{i,3} &= (1 - g_{i,3})(g_{i,2})(g_{i,1}) \\ w_{i,4} &= (g_{i,3})(g_{i,2})(g_{i,1}) \end{aligned} \quad (4)$$

As an illustration, if the four nearest neighbors of node *i* have measured thicknesses of 1.50, 1.70, 1.90 and 2.00 mm and are respectively at geodesic distances from node *i* of 1,2,3 and 4 cm, then, by definition, $t_{i,1}$ = 1.50 mm; $t_{i,2}$ = 1.70 mm; $t_{i,3}$ = 1.90 mm; $t_{i,4}$ = 2.00 mm and $d_{i,1}$ = 1 cm; $d_{i,2}$ = 2 cm; $d_{i,3}$ = 3 cm; and $d_{i,4}$ = 4 cm. From Eq. 1, $g_{i,1}$ = 0.1; $g_{i,2}$ = 0.2; $g_{i,3}$ = 0.3; $g_{i,4}$ = 0.4. From Eq. 4, $w_{i,1}$ = 0.9; $w_{i,2}$ = 0.08; $w_{i,3}$ = 0.014; and $w_{i,4}$ = 0.006, such that $w_{i,1} + w_{i,2} + w_{i,3} + w_{i,4}$ = 1. From Eq. 2, we can estimate the thickness of node *i*, t_i = 1.52 mm. In the absence of an existing proven method for interpolation, we developed the functional form of this interpolation model to ensure that 1) there is a

discontinuity-free distribution of interpolated values with a predominant weighting for the nearest neighbor with measured value; 2) a baseline model with hypothetically homogeneous measured values will result in a homogeneous interpolated model (since the sum of weights = 1); and 3) when the interpolation is applied to a node with a measured value (i.e., when a node's nearest neighbor is itself; $d_{i,1}$=0), the interpolated value will converge to the measured value itself (i.e., $t_i = t_{i,1}$ if $d_{i,1}$=0). Given the sparse distribution of test specimen strips per AAA, it was important that the nearest neighbor predominantly determines the interpolated value. Figure 3 illustrates the result of interpolating thickness values from measured sites to all vertices in the AAA surface model. The methodology described above for wall thickness interpolation was used for all the properties – wall thicknesses, failure stress, failure tension and the elastic coefficients, [9].

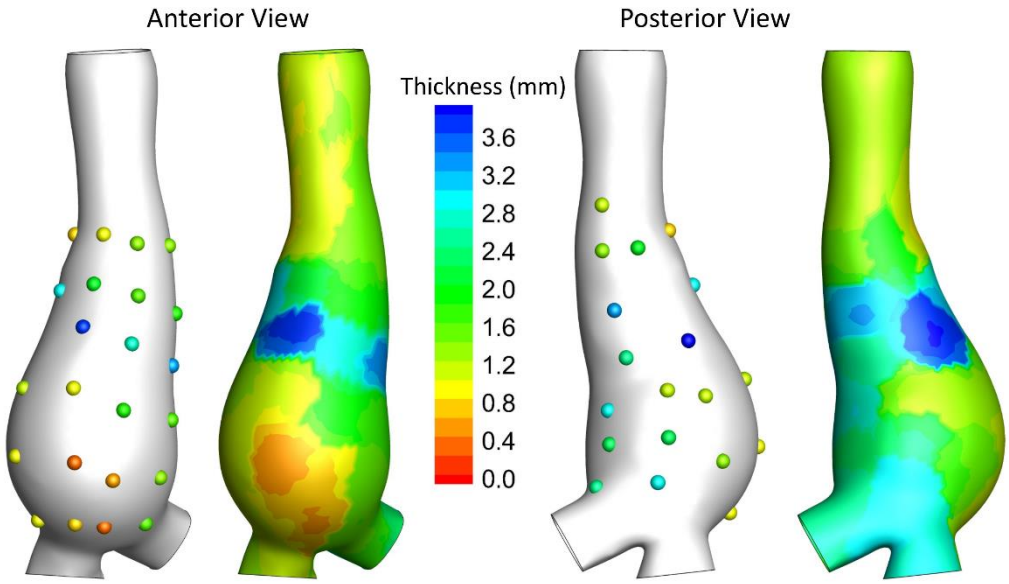

Fig 3: Example of thickness interpolation

Finite element analysis and interpretation

The finite element model of the AAA at zero pressure with shell elements (S3R Abaqus) and regionally varying wall thickness and elastic parameters based on the interpolations was created in Abaqus (3DS, Waltham, MA). The morphology of intraluminal thrombus that was present in some of the aneurysms was not included because they cannot be visualized in photographs. The proximal and distal ends of the aneurysm model were constrained on all degrees of freedom and uniform pressure of 120 mmHg (1.57 N/cm^2) was applied internally assuming the zero pressure initial models were stress-free. Nonlinear finite element analysis with an automatic time stepping scheme was performed and the resulting stress distribution and deformation was documented. In assessing the stress distribution, we focused on the maximum principal stress. From the

resulting elemental stress distribution, the elemental stress resultant or wall tension was estimated as,

$$Tension = \sigma\, t\, \frac{A_o}{A_f} \qquad \text{Eq. 5}$$

where, σ is maximum principal stress at the element, t is the undeformed thickness of the element (average of nodal thicknesses), A_o is the undeformed element area and A_f is the deformed element area. The element area ratio incorporates the fraction by which the thickness is altered during inflation due to incompressibility. Vande Geest et al. (2006), Doyle et al. (2009), Gasser et al. (2016) proposed the wall stress to strength ratio as an indicator of rupture risk. In this study, the failure properties (failure stress, failure tension) were measured on a subject-specific basis and interpolated to all of the nodes. So, the nodal distribution of pressure-induced wall tension to failure tension ratio (TFT) was also computed. In interpreting our results, we computed and studied both wall stress and wall stress resultant (wall tension), but focused on the latter only because rupture is a complete thickness tear that can only occur when the stress resultant breaches its maximum allowable threshold (failure tension), to take a simplistic failure model [82]. Large population studies reporting on AAA stress analysis [40–42,45,49,60,77] have assumed the same spatially uniform wall thickness for all aneurysms in their study population, but for some exceptions [54]. Thus, these studies were essentially reporting peak wall tension (stress resultant) scaled by a constant value (the presumed wall thickness). Therefore, our focus on wall tension as opposed to wall stress therefore is more consistent with literature.

Reliability of traditional forward approach to AAA stress analysis

As a secondary arm of this study, we also evaluated the reliability of assumptions made while using the traditional approach to finite element analysis of patients' AAA based on non-invasive imaging because of lack of little additional information on a patient-specific basis. They include some or all of these assumptions: 1) assuming that the geometry reconstructed from non-invasive imaging data is stress-free when it is in fact not even load-free, having been pre-deformed due to mean aortic pressure; 2) assuming homogeneity in wall thickness and elastic parameters; and 3) assuming all subjects in the population have the same homogeneous wall thickness and elastic parameters, ignoring patient-specificity. These are all understandable assumptions, no doubt. Irrespective, owing to the unique *ex vivo* experimental data collected in this current study, we have avoided all those assumptions. Thus, the results provide us a rare opportunity to assess the validity of the traditional approach. We used the current analysis results as the standard ("load-free heterogeneous model") to compare against the traditional approach ("pre-deformed homogeneous model"). The pre-deformed homogeneous model involved starting with the deformed models from the load-free heterogeneous model analysis as the input stress-free configuration (equivalent to the models that are obtained from non-invasive imaging). Wall thickness and elastic parameters were spatially uniform within each AAA and the same for all AAA models (1.9 mm thick; $\alpha = 17.4$; $\beta = 188.1$ N/sq.cm). Internal pressure of 120 mmHg was applied internally on the aneurysm wall and the finite element analysis performed similar to that done with the load-free heterogeneous model. The peak wall tension was estimated for each AAA

and compared to assess the reliability of the traditional approach for AAA stress analysis using which many large population longitudinal studies have been reported.

RESULTS

Stress analysis for all thirteen aneurysms reached convergence (Figure 4). The midsection diameter of the ruptured group was higher than that of the unruptured group (mean±SD: 6.3±1.3 versus 4.1±1.0 cm) with statistical significance (Mann Whitney U Test, two-tailed P = 0.0056). The average peak wall tension defined as 99th percentile value within the spatial distribution in ruptured group was higher than that in the unruptured group, but without statistical significance (mean±SD: 4.98±1.37 versus 3.49±0.91 N/cm; P = 0.074; Figure 5). The peak wall stress was also higher in the ruptured group without statistical significance (47.5 ± 12.0 versus 41.6 ± 17.6 N/cm; P = 0.17; Figure 5). The peak TFT was higher in the ruptured group also without statistical significance (0.75 ± 0.35 versus 0.44 ± 0.20; p = 0.099 ;Figure 5). Figure 6 shows the four ruptured AAA along a view where the rupture site is visible and the distributions of wall tension, wall stress, and TFT. The variation of wall tension and TFT along the rupture line is shown in Figure 7. A comparison of peak wall tension computed using the zero-pressure heterogeneous model used in this study and that using the traditional pre-deformed homogeneous model is shown in Figure 8. Traditional approach overestimates the peak wall tension by 3 percent, but do so

consistently in all cases such that its stratification of aneurysms in a study

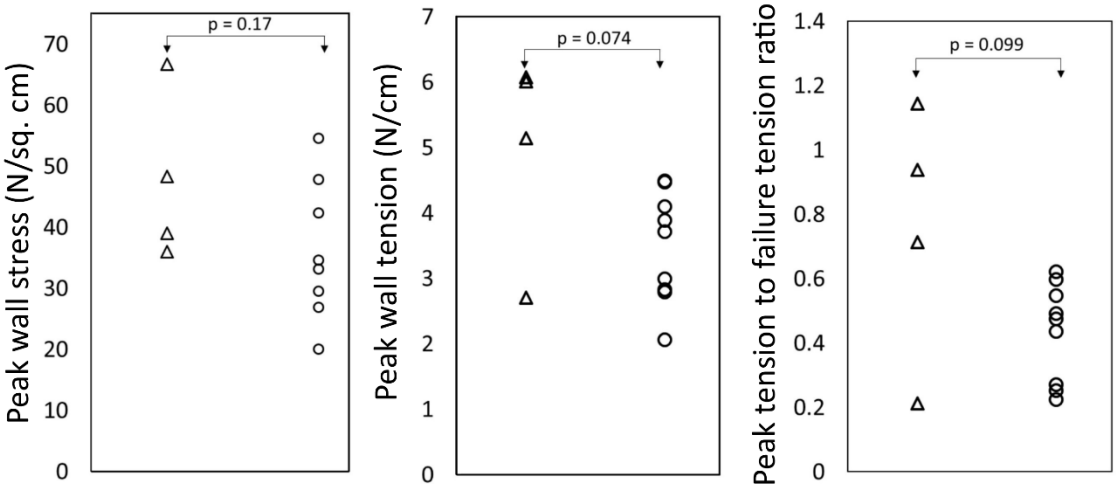

Fig 5: Comparison of indices in ruptured vs. unruptured AAA.

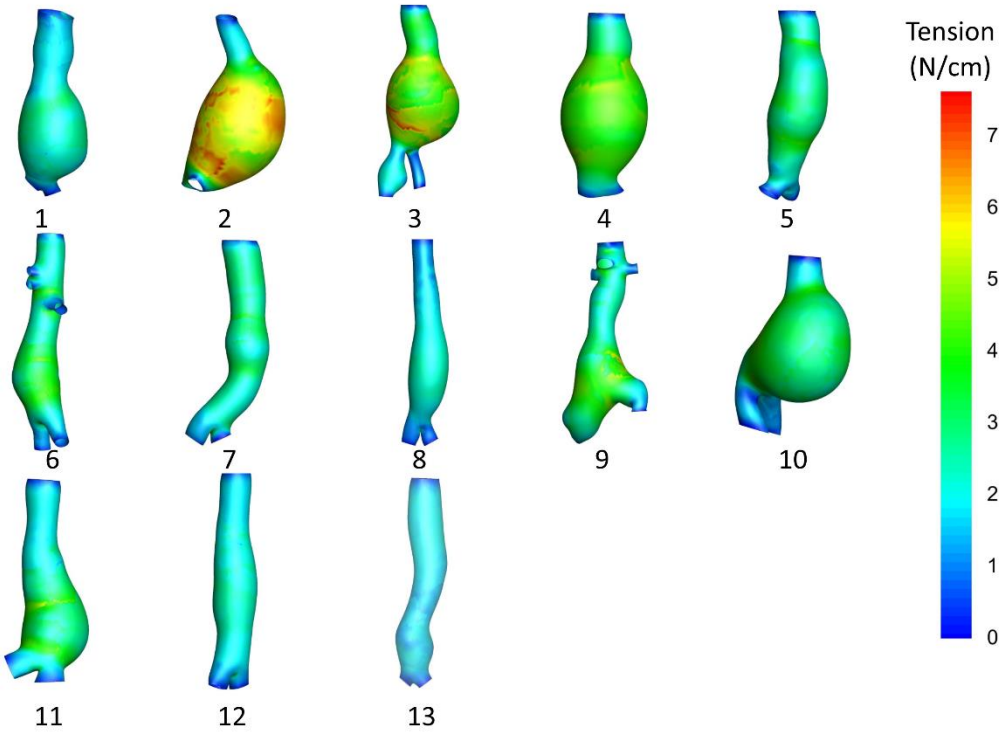

Fig 4: Computational results of all nine AAA.

population is almost identical to the zero-pressure heterogeneous model.

DISCUSSION

This study is different in unique and important ways from previously reported computational modeling approaches because the AAA used in this study were harvested whole from human cadavers. The morphology of each AAA was known at zero pressure, regional variations in wall thickness, elastic properties and failure properties were measured within each AAA and the precise location and spread of the rupture site was recorded with high fidelity (in the ruptured AAA). This rich information helped evaluate whether there exists a causative relationship between elevated wall stress resultant and rupture. In interpreting our results, we focus on stress resultant or tension first. The results did not show the ruptured aneurysms to have statistically higher peak wall tension although it was on average 43% higher trending toward significance (Figure 5). That 43% difference can be attributed to the ruptured group being 54% larger in diameter with statistical significance. Even if one takes the trend toward significance as relevant, that just speaks to correlation. However, if the site of peak wall tension matches that of rupture, it would be consistent with a causative relationship. The precise site of peak wall tension did not match the rupture site in any of the four AAA, but it is reasonable to wonder if it matches ‘closely enough’. Now, what constitutes a ‘close enough’ match is subjective. To objectify the process, we studied the wall tension and TFT along the rupture line in the four ruptured AAA

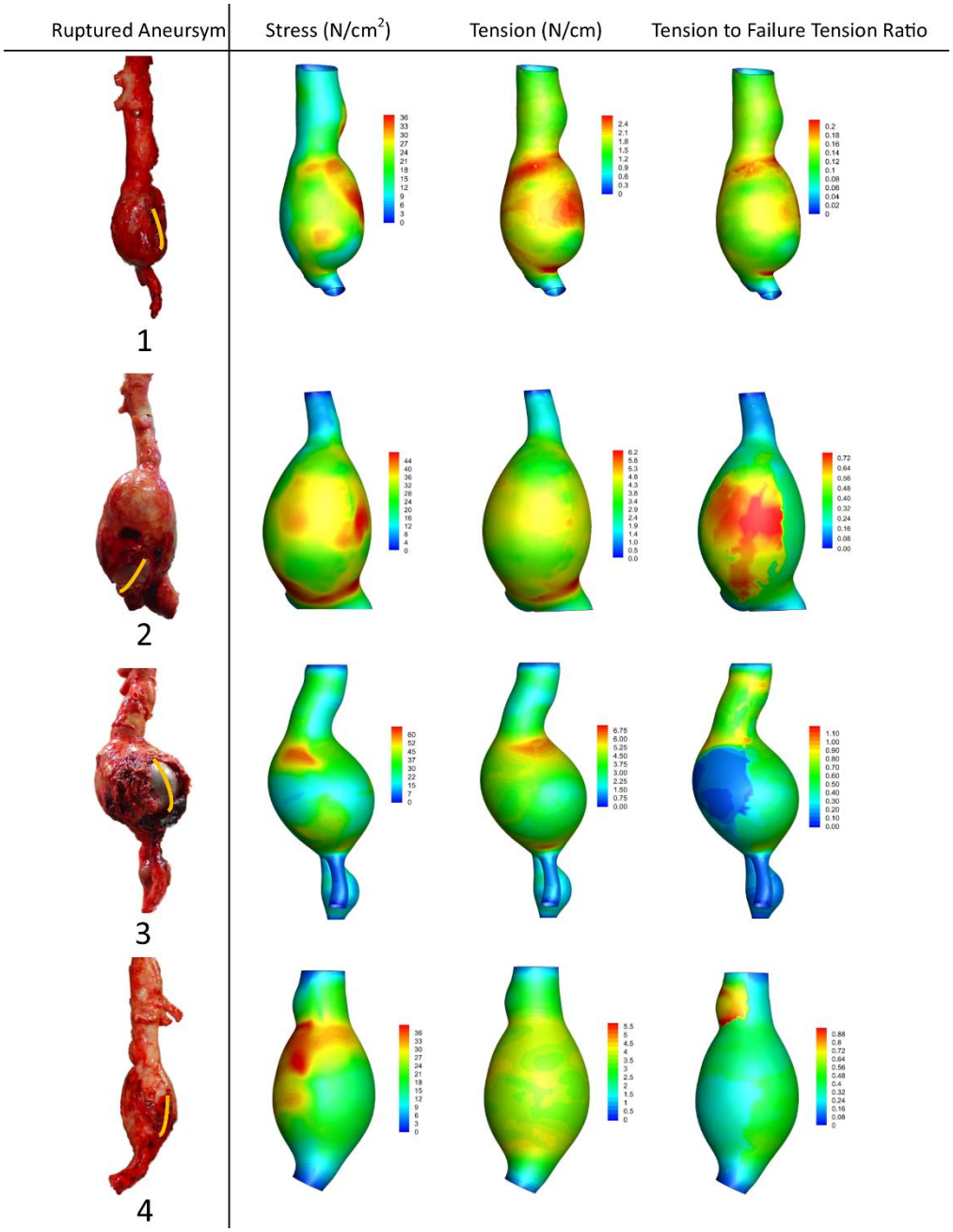

Fig 6: Rupture site location and indices.

(Figure 7). How close is the rupture line tension to peak wall tension? The average rupture line tension as a fraction of the AAA-specific peak wall tension was 88%, 84%, 59% and 79% in AAA #1, 2, 3 and 4 respectively. In none of the four AAA, the TFT breached 1.0 along the rupture line as consistently seen in Figures 6 and 7. For reasons stated earlier, we submit that inferences drawn

from wall stress needlessly distracts from the idea of rupture. But to keep with convention in the field, we studied it. The peak wall stress in the ruptured AAA was only slightly higher (14%) without statistical significance. And the location-specific observations offer even less support for a match between the sites of peak wall stress and rupture. Overall, these findings do not offer strong support for a causative relationship between AAA wall tension (or for that matter, just wall stress) and rupture. At best, they do not rule out the possibility that peak wall tension caused rupture in two of the four AAA, but that certainly does not constitute adequate support to the causation hypothesis. Some key limitations of our study are worthwhile to consider in this context. The lack of inclusion of intraluminal thrombus owing to the nature of experiments conducted means that we are likely overestimating the computed wall tension and likely by a factor that is spatially varying. It is important to recognize thrombus was ignored as well in many of the earlier large population studies such as that by Fillinger et al. (2002, 2003) which continue to be widely cited. The findings reported here certainly provide more context in evaluating these earlier studies. The sites of failure properties measurement were sparsely located. Thus, the interpolated values and consequently, tension to failure tension ratio should be viewed with some caution. We didn't know the systolic pressure at the time of rupture in those patients. This affects the wall tension values but not its spatial distribution. The study population is too small for drawing any conclusion. But, in this first attempt at checking for a causative role for peak wall tension, we failed to find evidence to support it. Possibly in all four ruptured AAA, but certainly likely in two, it is

plausible that rupture was caused, not by localized elevated wall tension, but by localized weakness (manifesting as low failure tension). This localized weakness may well have not been captured by the sparse collection of specimen strips cut for testing. Again, this highlights the need for a denser collection of specimen strips to assess the true distribution of failure properties.

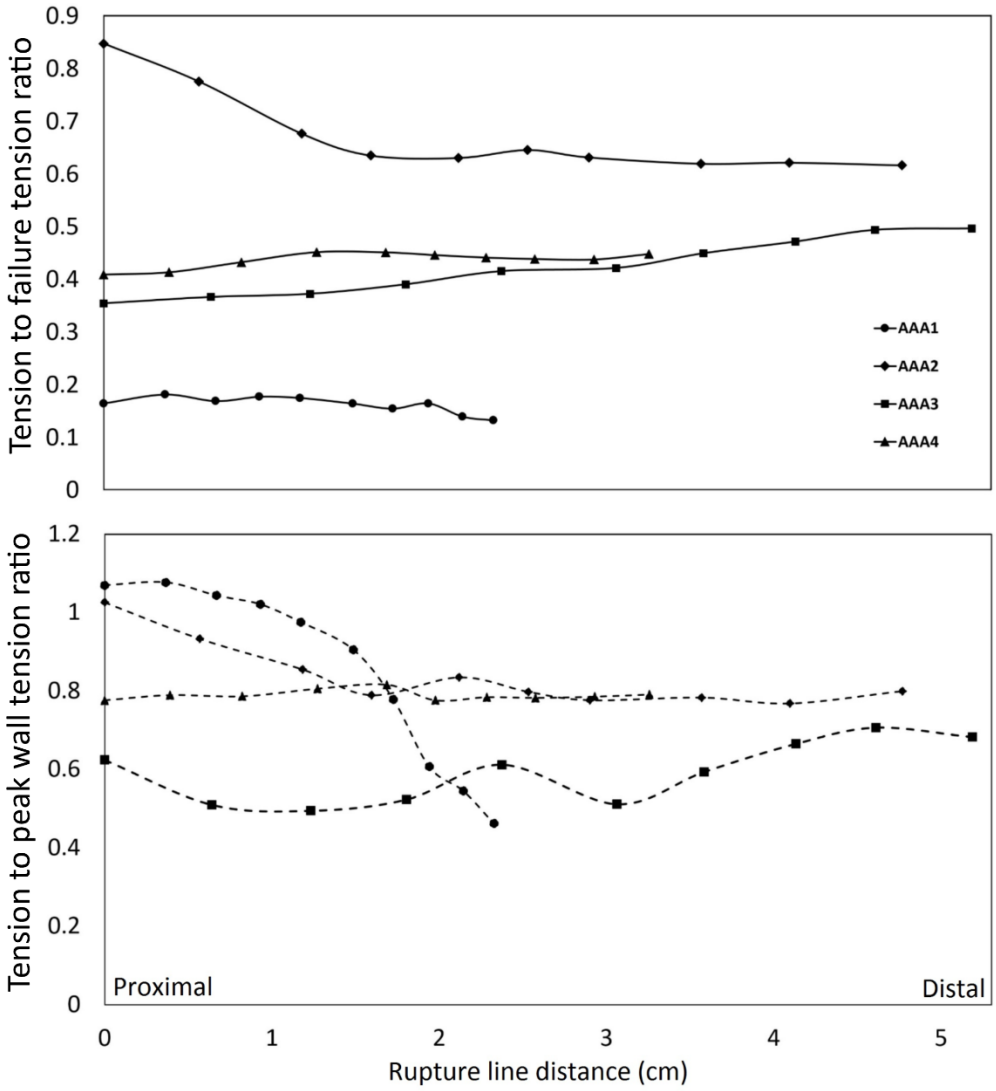

Fig 7: Characterization of rupture line.

We have reported earlier that an inverse elastostatic approach would be the appropriate method for stress analysis of such pre-deformed structures [76]. Still it is worthwhile to investigate the scope for error in the traditional forward approach. The remarkable agreement in peak wall tension between the load-free heterogeneous model and the pre-deformed homogeneous model (Figure 8) offers strong support to the claim that the latter is reasonably reliable for peak wall tension estimation. This is not surprising. AAA stress analysis is essentially a geometry-driven problem with little sensitivity to elastic parameters. And, since we focus on wall tension rather than wall stress, any lingering sensitivity to wall

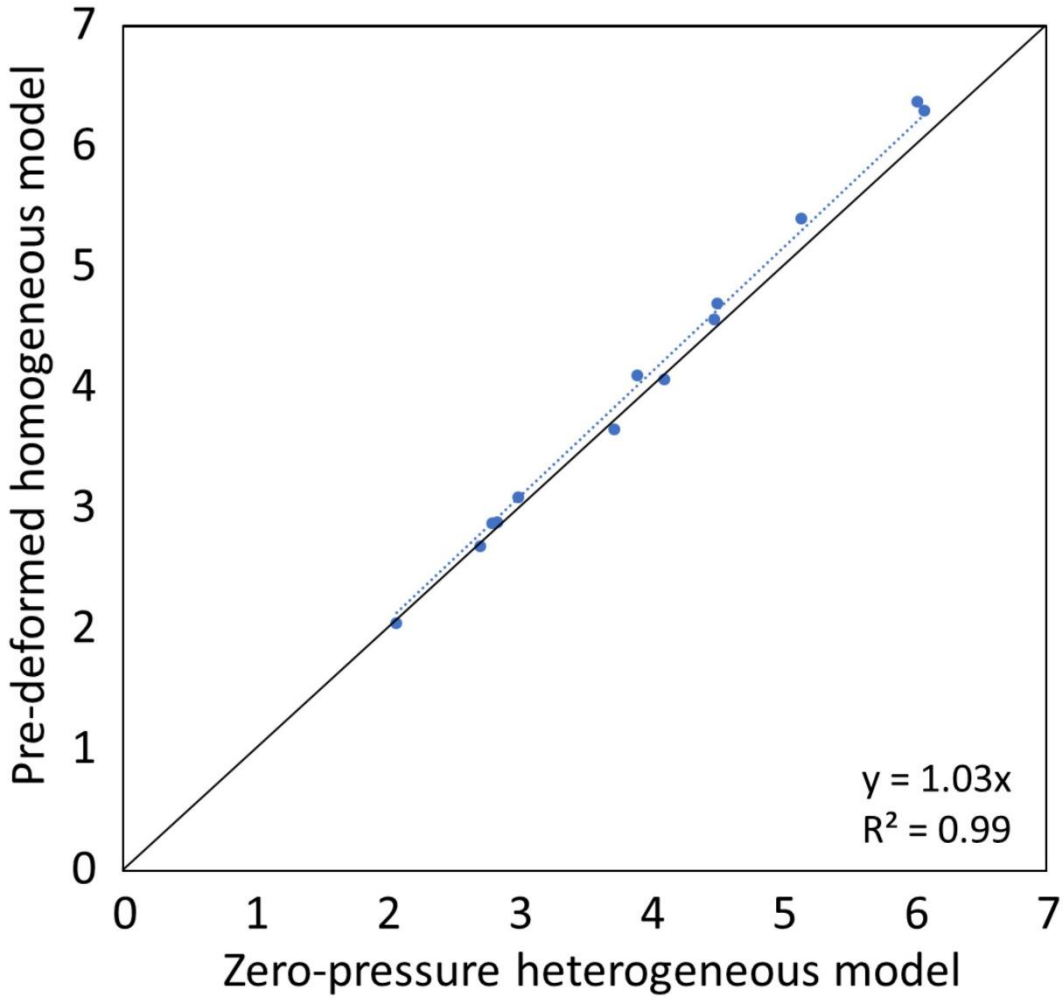

Fig 8: Heterogeneous vs. Homogeneous Model.

thickness is also obviated. That the pre-deformed homogeneous model overestimates peak wall tension (by 3%) makes sense because the input model for this traditional approach is slightly more inflated than that used for the load-free heterogeneous model.

CONCLUSION

In this study of four ruptured AAA and nine unruptured AAA, there was not adequate evidence to support a causative relationship between wall tension or stress and rupture. Localized weakness (reduced failure tension) should be investigated as an alternative causative factor in rupture. More rigorous experiments are needed before conclusive inferences may be drawn however. Traditional stress analysis from noninvasive imaging of patient-specific AAA provides reliable estimates of peak wall tension despite many of the common assumptions made regarding the pre-deformed geometry and elastic parameters.

ACKNOWLEDGEMENTS

This study was partially supported by a grant from the American Heart Association Heartland Affiliate #0365408Z.

CONFLICT OF INTEREST STATEMENT

The authors have no financial or personal relationships with other people or organizations that could inappropriately influence (bias) our work.